COMPANIONS TO APOGEE STARS: A STELLAR POPULATIONS VIEW OF THE MILKY WAY'S STELLAR AND SUBSTELLAR COMPANION HOSTS

Nicholas William Troup
Littlestown, Pennsylvania

B.S. Physics, University of Delaware, 2012

M.S. Astronomy, University of Virginia, 2014

A Dissertation Presented to the Graduate
Faculty of the University of Virginia
in Candidacy for the Degree of
Doctor of Philosophy

Department of Astronomy

University of Virginia
August 2017

Committee Members:

Steven R. Majewski
Phil Arras
Zhi-Yun Li
Michael F. Skrutskie
Eric Herbst

Abstract

Over the past few decades, the power of statistical population studies of multiplicity has been unleashed, allowing us to derive general properties such as period, eccentricity, and mass ratio distributions for binary stars. With the explosion of candidate and confirmed planetary systems recently made available, due in large part to NASA's *Kepler* mission, these types of studies are now becoming possible for exoplanet systems as well. The Sloan Digital Sky Survey's (SDSS-III/IV) Apache Point Observatory Galactic Evolution Experiment (APOGEE) is an ongoing stellar chemodynamical survey of the Milky Way and its closest galactic neighbors, but given its typical radial velocity (RV) precision of ~ 100 m s^{-1}, APOGEE can also detect companions with masses as low as a few Jupiter masses around solar-mass stars. This gives APOGEE a unique place among the aforementioned population studies as the first Galaxy-wide survey for stellar and substellar companions, capable of sampling a diverse set of stars and environments.

In three years of operation (2011-2014), the APOGEE-1 survey observed >14,000 stars with enough epochs over a sufficient temporal baseline for the fitting of Keplerian orbits to RV variations induced by companions. We present the custom orbit-fitting pipeline used to create this catalog, which includes novel quality metrics that account for the phase and velocity coverage of a fitted Keplerian orbit. Here we present initial results from a catalog of 382 of the most compelling stellar and substellar companion candidates detected by APOGEE-1, which orbit a variety of host stars in diverse Galactic environments. The most surprising result from this catalog is a large number of close-in BD companion candidates. We propose a few potential explanations of this finding, some which invoke this catalog's many small separation companion candidates found orbiting evolved stars, which suggests that the canonical

BD desert may only be a special case for Sun-like stars.

Several improvements to the APOGEE pipelines were implemented for the start of APOGEE-2 in SDSS-IV, including treatment for stellar rotational velocities in dwarfs and new methods for RV determination for low S/N spectra which we present here. These upgrades improve APOGEE's ability to derive orbits for stars in exciting new Galactic environments and for stellar populations never before probed with long-term RV monitoring. We exploit these improvements and the extended baseline of APOGEE-2 to build a new catalog of $\sim$700 companion candidates that includes the first two years of APOGEE-2 observations. This new catalog supports the primary result from our previous sample of a large number of BD companion candidates from 0.1AU $\lesssim a \lesssim$ 3AU. We combine the orbital parameters in this catalog with the uniformly-derived stellar parameters and chemical abundances available with the first APOGEE-2 data release to investigate the plausible formation mechanisms of the brown dwarf companions in our catalog.

Finally, we present some of our ongoing follow-up efforts to further vet our candidate systems, and our dedicated APOGEE-2 goal science program to intentionally gain a large number of additional epochs of APOGEE-1 targets. We also introduce the APOGEE Time-Domain Legacy Survey (ATLaS), a major After Sloan 4 (AS4) program that will expand upon the work presented here and extend it well into the next decade.

Acknowledgments

First, to my advisor, Steve: Thanks for giving the freedom and flexibility to explore what interested me even if it wasn't your "cup of tea" initially (although it seems like I have at least partially converted you). You really helped me find my niche in APOGEE, all the while teaching me how to navigate the often tricky politics of a large collaboration. I appreciate all the time you spent thoughtfully commenting on drafts and crafting letters of recommendation for me. You have helped me establish the foundation of a successful career, and for that, you will never be forgotten. I look forward to our continued professional relationship, and I will be proud to count myself among the illustrious group of SRMGRP alumni. To the rest of my committee: Thank you for all of the time you took out of your busy schedules to meet with me and offer valuable advice on this work. To all of my APOGEE collaborators: Thank you for taking a chance on a young scientist who hadn't quite found his home yet, and for giving me the opportunity to leave my mark on the survey. Of course, I am obliged to acknowledge financial support from the Sloan Foundation, the Virginia Space Grant Consortium, and the National Science Foundation (AST-1616636).

To Whitney, Barbara, Jackie, and David: You are the glue that holds this department together. Thank you for making sure we always got paid, for fixing things when we broke them, and for dealing with all of the other requests that got thrown your way on a daily basis. To Ed and Kelsey: Thank you for acting as mentors to me in matters of education and public outreach. I count what I learned and the experience I gained in those areas as valuable as my research experience here. To all of the members of DSBK: I was proud to be a part of this group while at UVa, and I am so happy to an enthusiastic new group of leaders to take the reigns. To Dom, Scott, Meng, Heifeng, Chenliang, and Oza: I could not have asked for better office-mates.

I'm sorry I am ruining the lock-down we've had for the past five years, but I'm sure you will find a worthy replacement. Your kids (Human or otherwise) were always a welcome presence and a great source of stress relief. Thank you for always being there to listen to our frustrations, share each others' successes, and just overall reminding me why UVa was a great place to be. I will miss you my friends. To Sandy: So much of the above applies to you as well. Thanks for all of the rides home, the shared meals, and the times you kept Chrissy company while I was out of town, but most of all, thank you for reminding me that it was OK to relax occasionally.

Finally, I would like to express my eternal gratitude to my family, both by blood and by marriage. To my parents and grandparents-in-law: Thank you for letting me whisk away your (grand)daughter for a few years (I know you are excited to have her back). Thanks for all support you have provided during this transitional time, and I look forward to spending more time with you in the coming years. To my parents and grandparents: Without your unwavering support and unconditional love, I would not be here today. While Steve helped lay the foundation for my success, you are the bedrock on which it was built. I could fill volumes for all that you have done for me, and it is my hope that in return, I have at the very least made you proud. Last, but by no stretch of the imagination least, to my wife, Chrissy: I don't think I can adequately express how much having you by my side these past five years has meant to me. Thank you for putting up with and comforting me through all of the late nights, rantings, and stress. I also appreciated you trumpeting my successes to others when I was to timid to share them myself. Thanks for all of the "tough love" you showed me, and for cheering me on to the finish line. Most of all, thank you for always helping me keep perspective, and reminding me of the truly important things in life. I love you, and I look forward to our next adventure together.

"The heavens declare the glory of God;
the skies proclaim the work of His hands.
Day after day they pour forth speech;
night after night they reveal knowledge."
Psalm 19:1-2

Table of Contents

List of Figures

List of Tables

Chapter 1

Background and Motivation

Over the past few decades, it has been established that solitary Milky Way stars are the exception rather than the rule. Previous studies of stellar multiplicity have shown that more than half of stellar systems contain two or more bound stars, and that stars in these systems span a wide range of separations and mass ratios (e.g., Raghavan et al. 2010; Duchêne & Kraus 2013). With the advent of the enormous database of confirmed and candidate systems generated by the large-scale planet-hunting mission *Kepler* (Borucki et al. 2010), planetary companions are also thought to be quite commonplace. However, it turned out that many of these systems, especially among the first discovered, were quite unlike our own solar system, with many including an unexpected class of short-period Jupiter-mass planet (Mayor & Queloz 1995). These "hot Jupiters," have been explained by inward orbital migration during their formation (Masset & Papaloizou 2003), a concept that would not have likely to be given as much consideration in the formation of planetary systems if it was not for the discovery of hot Jupiters. Applications of these concepts to the Solar System inspired new theories regarding its formation such as the Nice (Tsiganis et al. 2005) and Grand Tack (Walsh et al. 2011) models. Therefore, the study of exoplanetary

systems has allowed us to gain a better understanding of how our own Solar System came to be and are how it fits in context of planetary systems in our Galaxy.

1.1 Exoplanets and Binaries: From Studies of Individual Objects to Statistical Populations

Studies such as Raghavan et al. (2010) demonstrate the power of statistical populations studies of multiplicity, allowing us to derive general properties such as period, eccentricity, and mass ratio distributions for binary stars. With the explosion of candidate and confirmed planetary systems recently made available, due in large part to Kepler (see Figure 1.1), these types of studies are now becoming possible for exoplanet systems as well.

1.1.1 Brown Dwarfs and The Brown Dwarf Desert

Brown Dwarfs (BDs) were first hypothesized by Kumar (1962) from the the realization that as stars of sufficiently low mass condense out of the interstellar medium, they will become dense enough to be supported by electron degeneracy pressure before they become hot enough to fuse hydrogen in their core. However, these objects, which are canonically defined as having a mass between the Deuterium-burning limit ($\sim 13 M_{Jup}$) and the Hydrogen-burning limit ($\sim 80 M_{Jup}$), were not observed until nearly three decades later. The first BDs were discovered as companions to a white dwarf (Becklin & Zuckerman 1988) and a red dwarf (Nakajima et al. 1995), and the first free-floating BD was discovered by Rebolo et al. (1995) in the Pleiades cluster.

Over the following decade it became apparent, that while both exoplanets and stellar-mass companions have been found in extremely short-period orbits, there was

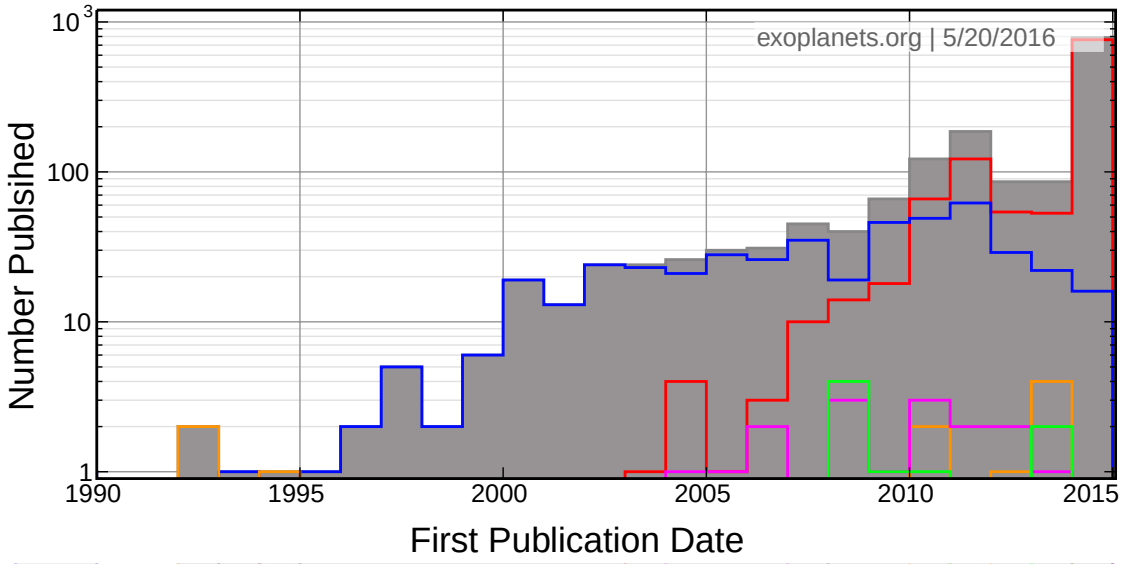

Fig. 1.1.— A history of the discovery of substellar companions through the end of 2015 as compiled by the exoplanet.org database. The most successful detection methods by far are radial velocity monitoring (blue) and transits (red), with the later overtaking in recent years thanks to the efficiency of *Kepler*. Less common methods of detection such as microlensing (magenta), transit/pulsar timing (orange), and direct imaging (green) are also shown. The grey filled histogram is the sum of the discoveries from all detection methods.

a clear paucity of BD companions orbiting Sun-like stars emerging (Marcy & Butler 2000). This phenomenon, which is now known as the "BD Desert," required considering companion hosts as a *population* to be uncovered. More recent work has shown that this Desert might be limited in extent, only existing for relatively small separation ($a < 5 - 10$ AU) companions (Gizis et al. 2001; Grether & Lineweaver 2006), but Grether & Lineweaver (2006) still estimated that $< 1\%$ of Sun-like stars host BDs (see Figure 1.2). However, even this has been filling in as several close-in BD companions have been discovered in recent years (e.g., Patel et al. 2007; Sahlmann et al. 2010; Johnson et al. 2011; Janson et al. 2012; Díaz et al. 2013; Jones et al. 2014b). Table A.1 in Wilson et al. (2016) summarizes all previously known brown dwarf companions to solar-type stars, now numbering in the several dozen.

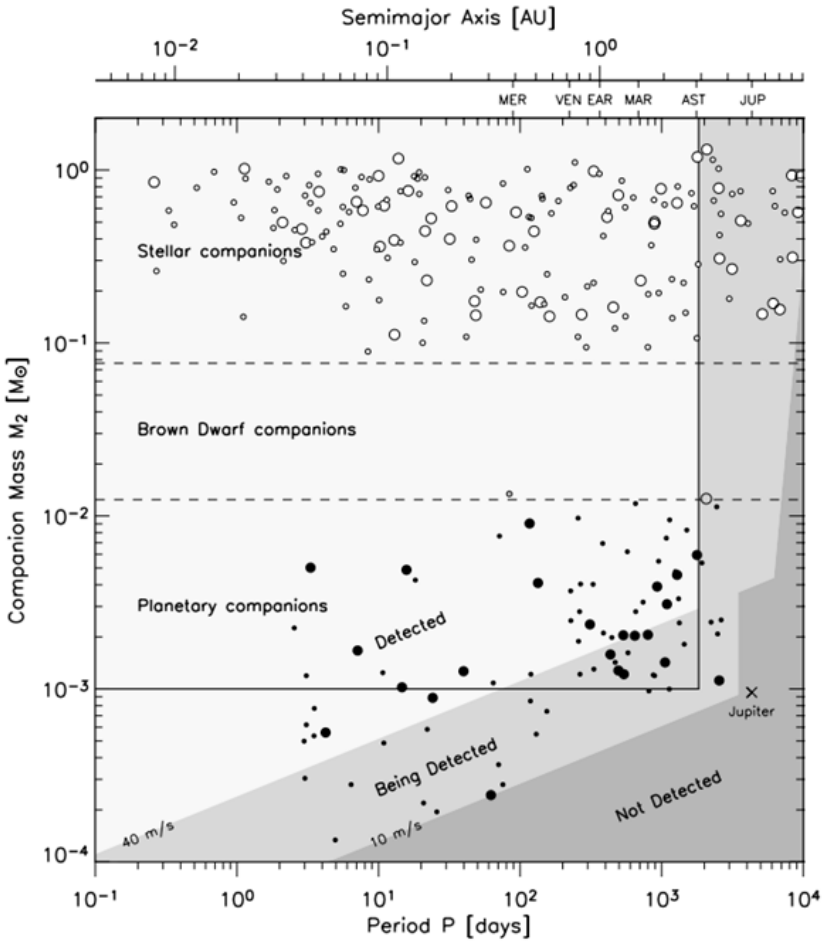

Fig. 1.2.— Figure 5 from Grether & Lineweaver (2006) demonstrating the brown dwarf desert.

1.1.2 Correlating Host Star Properties with Their Companions (or Lack Thereof)

Statistical populations of companion hosts and non-hosts allows for studies correlating companion occurrence with the properties of the host stars. From these studies, it is becoming clear that the properties of the host star plays an important role in the types of companions that are able to form with it. For example, planet occurrence rate been shown to depend on the mass of the host star, with higher-mass hosts being

less likely to host a planet than lower-mass hosts (e.g., Hekker et al. 2008a).

Several studies have indicated that planet-hosting dwarf stars have unique chemical abundance signatures when compared to their non-host counterparts. The most fundamental of these is the planet-metallicity correlation (PMC), which states that Jupiter-mass planets are more common around stars with higher metallicity (Fischer & Valenti 2005). However, it has recently been found that this trend decreases and ultimately disappears for stars hosting only Earth-mass planets (Hasegawa et al. 2014). Furthermore, the trend seems to be much weaker in the sample of RG stars discussed by Jofré et al. (2015). The PMC is believed to be a consequence of the core accretion (CA; Pollack et al. 1996) model of planet formation, which requires a potential Jovian planet to acquire ~ 5–$10 M_{\oplus}$ worth of solid material before the central star expels the hydrogen and helium gas from the protoplanetary disk (Matsuo et al. 2007). It has also been found that planets orbiting metal-poor stars have longer periods than those in metal-rich systems (Adibekyan et al. 2013). Meanwhile, stellar binaries are formed via a separate mechanism, and it is disputed whether or not metallicity plays a role in binary fraction (Abt 2008). Binarity has generally been found to be higher in lower metallicity populations (e.g., Carney et al. 2003). However, a higher fraction of stellar binaries has been found among metal-rich F-type dwarfs in the field compared to their metal-poor counterparts (Hettinger et al. 2015). It is not clear whether BD companion formation follows star or planet formation trends more closely. If lower-mass BD companions are formed as runaway giant planets via CA, then we would expect the PMC to be stronger for BD companions, extending the trends found by Adibekyan et al. (2013) and Hasegawa et al. (2014), as well as the trend described in Adibekyan et al. (2013). It is possible the formation pathway for these companions more closely mimics that of binary systems which is thought to be dominated by

gravitational fragmentation (Reipurth et al. 2014), or a gravitational instability (Boss 1997) scenario. Indeed, Mata Sánchez et al. (2014) found that BD-hosting stars were slightly more metal-rich than non-hosting stars, but not to the extent of the PMC suggesting that the BD formation may more closely mimic that of stars.

Work has also been done to explore the role of chemistry beyond just overall metallicity. Bodaghee et al. (2003) found abundances of 9 chemical elements for 77 gas giant planet hosts and saw differences in V, Mn, Ti and Co, between hosts and non-hosts. Dodson-Robinson et al. (2006) took stellar parameter and abundance data of 1040 nearby FGK dwarfs, including 99 planet hosts from the Spectroscopic Properties of Cool Stars catalog (SPOCS; Valenti & Fischer 2005),and found that abundances of Si and Ni in planet hosts were systematically enhanced over other stars of the same [Fe/H]. These authors constructed Monte Carlo simulations that predicted the fraction of star-disk systems that form planets via CA as a function of [Fe/H] and [Si/Fe], showing an increasing fraction with both abundances. Furthermore, Delgado Mena et al. (2010) suggested that C/O and Mg/Si ratios of a planet-host are useful diagnostics for determining potential terrestrial planet make-up. Variation in the [C/O] abundance may have a profound affect on planet formation and atmospheric chemistry (Kuchner & Seager 2005). Adibekyan et al. (2012) acquired abundances of 12 elements for 1111 FGK stars. They found that for Co, Na, Ni, V, and Mn there was a general increase in the frequency of stars with giant planets with increasing [X/Fe], and that most of their Neptunian hosts had [Al/Fe], [Sc/Fe] and [Mg/Fe] > 0. Low-mass planet hosts in their sample also exhibited slightly higher [Ni/Fe] abundance ratios. These studies suggest that specific chemical species play important roles in planet formation, and that abundances can act as flags for potential planet hosts. However, there is only limited agreement among the aforementioned trends.

1.2 The Growing Scope of Studies

For a number of reasons, most previous exoplanet searches have focused on main sequence stars: (1) Dwarf stars make possible the detection of close-in companions eliciting larger, more easily detectable RV and astrometric variations. (2) Dwarf stars have smaller brightness and radius contrasts with companions that better enable transit and direct imaging methods for companion detection. (3) There is a cultural bias within the exoplanet community toward finding planets around "Sun-like systems". Consequently, much less is known about planetary systems around evolved stars, and samples of such systems are relatively small.

Similarly, because of the aforementioned concentration on solar-like dwarf stars, and the greater difficulty in measuring transit signals and RVs for these types of stars at great distances, most of what we know about the multiplicity of stars and the nature and distribution functions of their stellar and substellar companions derives from observations of stars in the solar neighborhood (e.g., Duquennoy & Mayor 1991). Dominated by disk stars of solar metallicity, field stars in the solar neighborhood provide a limited perspective within the broader range of Galactic environments and their stellar populations. To go beyond such limitations most studies typically use kinematical and chemical means to identify less common representatives of other stellar populations that exist at low local densities, but this results in biased samples of these other populations, relegated to the small fraction of stars capable of interloping through the solar neighborhood from other Galactic locales. As a result, compared to solar metallicity stars near the solar circle, much less is known about, e.g., stellar and substellar companions in low metallicity field stars, or for field stars in the halo, outer disk and central regions of the Galaxy.

1.2.1 A Growing Cornucopia of Stellar Types

The first confirmed exoplanets were actually discovered orbiting a millisecond pulsar in 1992, and were thought to have been "second-generation" planets formed from its host's supernovae remnants (Wolszczan & Frail 1992). It was not until 3 years later that the first exoplanet around a Sun-like star was discovered (Mayor & Queloz 1995), and the vast majority of the subsequent effort over the next twenty years focused on Sun-like stars (i.e. FGK dwarfs) with the hope of finding an Earth analog (see Figure 1.3). M dwarfs have been receiving more attention lately (e.g., Johnson et al. 2007; Johnson & Li 2012), and recently some work has been done with evolved stars (e.g., Reffert et al. 2006; Lovis & Mayor 2007; Johnson et al. 2007; Wittenmyer et al. 2011; Zieliński et al. 2012). However, as of 2015, only approximately 50 planet-hosting giant stars have been confirmed in the literature (Jones et al. 2014a), compared to the $>$ 1000 known dwarf-star planet hosts (see Figure 1.3), but even this small sample of giant star hosts has produced some interesting results.

As a star like the Sun expands into a red giant, its atmosphere will engulf the innermost planets (e.g., Villaver & Livio 2009; Villaver et al. 2014). However, tidal dissipation models cannot account for the lack of the more easily detected close-in planets around evolved stars (see Fig. 9 in Privitera et al. 2016), raising questions about whether stronger tidal dissipation leading to the engulfment of farther out planets is at play. Possible observational signatures of planetary engulfment have been identified in the chemical abundances and peculiarly high rotational velocities seen in some giant stars (e.g., Massarotti et al. 2008; Adamów et al. 2012; Carlberg et al. 2012). Engulfment of a sufficiently large planet may lead to ejection of the RGB star's envelope, and formation of an isolated helium core white dwarf (Nelemans & Tauris 1998; Nordhaus et al. 2010). This scenario is supported by observations

that have found hot Jupiters orbiting sdB stars, which suggests that some Jovian planets may survive within the extended envelope of their host star during its RGB phase (e.g., Silvotti et al. 2014). However, for small mass companions or large final separations, this interpretation is problematic because there is not enough orbital energy to eject the envelope. Alternatively, the substellar companion could have merged with the helium core of the RGB primary, ejecting the envelope, and forming an *isolated* helium core white dwarf in the process (Nelemans & Tauris 1998).

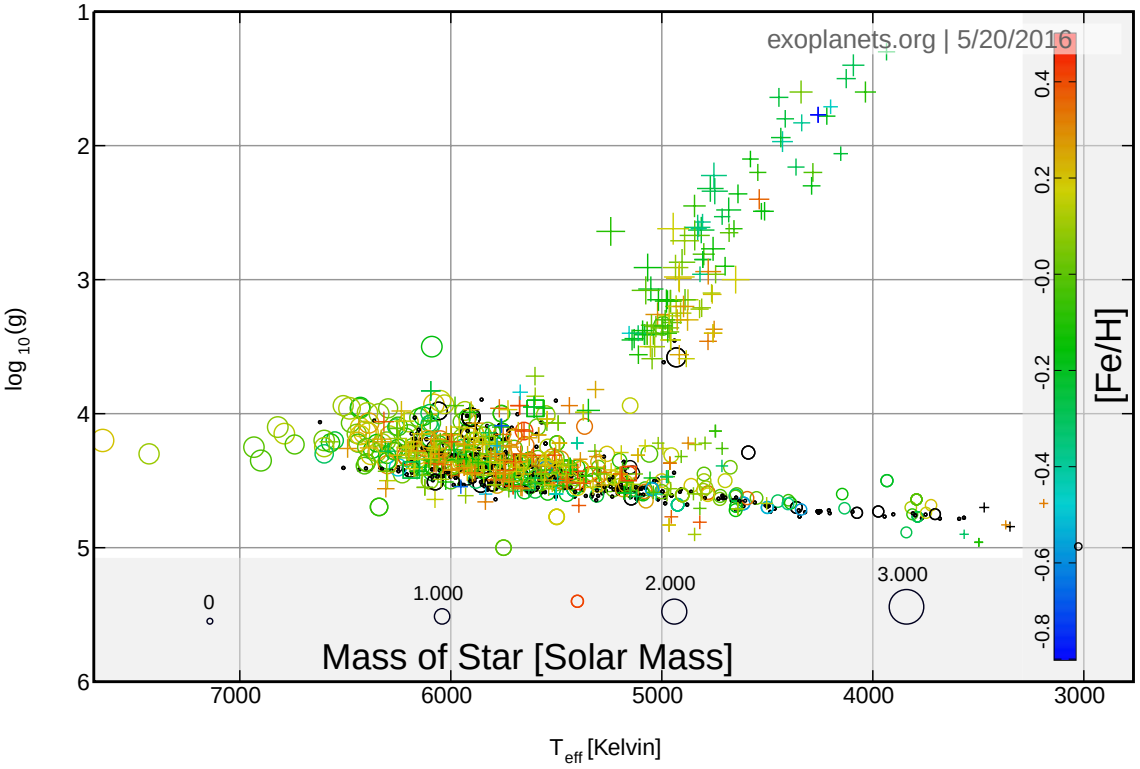

Fig. 1.3.— A spectroscopic HR diagram of the known planet in the exoplanet.org database as of the end of 2015. Symbol size and color represent the mass and metallicity of the host star, with black dots indicating host stars with no mass or metallicity measurements. Plot symbol indicates the method used to detect the companion with open circles indicating transit, plus signs indicating RV, squares indicating timing, triangle indicating directly imaged companions, and filled circles for companions detected via microlensing. It is interesting to note that while transit detections dominate among the dwarf hosts, planets around giant stars have largely only been detected via RV.

1.2.2 Microlensing and Galactic Reach

Studies of the role of environment on companion formation have focused primarily on the role of stellar density via the study of star clusters (e.g., Armitage 2000; Adams et al. 2006). Clusters can be particularly fruitful subjects for study of stellar multiplicity because substantial statistical information about the frequency and mass ratios of stellar companions can be inferred from color-magnitude distributions (e.g., in the strengths of binary main sequences and the presence of blue stragglers), and clusters lend themselves to multi-object spectroscopy for efficient collection of RV time series data on many stars. Moreover, whereas it has been difficult to ascertain the ages of field stars, star clusters allow relatively reliable age-dating. Unfortunately, the open clusters subjected to detailed study of companions (e.g., via the WIYN Open Cluster Survey – Mathieu et al. 2004; Geller et al. 2008; Milliman et al. 2014) do not span a significantly larger volume of the MW than what has been probed for field stars. Furthermore, the vast majority of planets have been identified among Galactic field stars, while only a few planets have been discovered in open clusters such as NGC 2423 and 4349 (Lovis & Mayor 2007), as well as M67 (Brucalassi et al. 2014). However, useful information has come from analyzing binaries in clusters. Studies such as Verbunt & Phinney (1995) and Mathieu et al. (2004) were able to use the age information available to cluster binaries to measure the circularization timescale of binaries in a variety of configurations and evolutionary stages.

Studies exploring companion occurrence beyond the local Milky Way disk environment have been meager, as most surveys for stellar and substellar companions have focused on stars in the solar neighborhood. While it is possible with HST to generate deep CMDs from which all sorts of features attributable to stellar companions have been explored (e.g., Milone et al. 2012), few *globular* clusters have been systemati-

cally monitored for RV variations needed to characterize the companions in detail. The SWEEPS transit survey with HST (Sahu et al. 2006), and Microlensing surveys such as The Optical Gravitational Lensing Experiment (OGLE; Udalski 2003) have discovered potential planetary-mass candidates in the Galactic Bulge (Shvartzvald et al. 2014), but few other planets have been found farther than $\sim$ 1 kpc from the Sun (see Figure 1.4).

The potential effects of dark matter (DM) concentration on companion formation processes are completely unexplored. The most DM-dominated galactic environments are found in dwarf spheroidal (dSph) galaxies, where the (M/L)s far exceed those of the MW disk. Only a modest amount of work has been done to even measure the binary fraction of dwarf spheroidal galaxies. The most comprehensive analysis was performed by Minor (2013), who found an average binary fraction of 0.5 among $\sim$ 500 stars across the four dSph galaxies in their sample. However, the binary fractions they derived were all quite unconstrained, and these authors assert that "the allowed parameter space of binary fraction and period distribution parameters in dSphs will be narrowed significantly by a large multi-epoch survey." Typical dSph galaxies are very metal-poor and would not be expected to harbor many planets due to the aforementioned PMC. However, the Sagittarius (Sgr) dSph galaxy, a satellite galaxy currently merging with the MW, is fairly unique in that it has $M/L = 10$ (Law & Majewski 2010), but metallicity spanning from [M/H] < -1 to [M/H] > 0 (Siegel et al. 2007). Moreover, its current orbit around the MW places it currently in fortuitous proximity (29 kpc; Siegel et al. 2011) compared to other dSphs. This unique combination of high metallicity, large M/L, and relative nearness makes the Sgr dSph the perfect laboratory for exploring the question of companion frequency in dark-matter-rich environments, as well as the effects of minor mergers on the

creation and stability of such systems. The MCs, about twice as far away, but still close compared to many MW satellites, also contain metal-rich stellar populations that are interesting and feasible to probe for stellar companions.

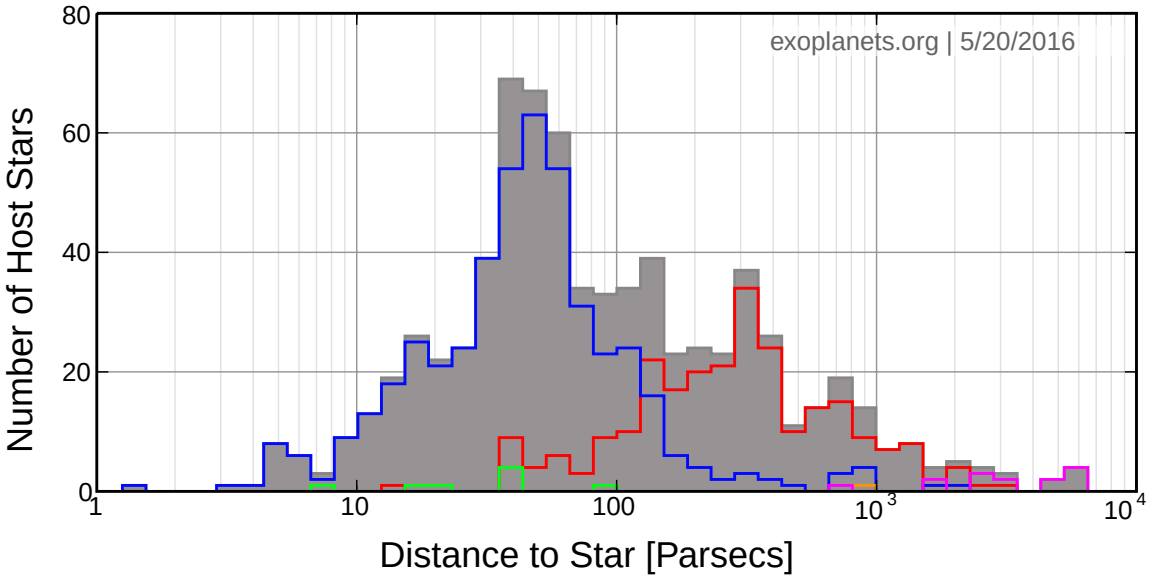

Fig. 1.4.— Histogram showing the distribution of the distances to planet host stars from the Sun in the exoplanets.org database. The colors again indicate detection method, and are the same as Figure 1.1. This figure only includes host stars with a reliable distance measurement, hence the smaller contribution from transit discoveries (red histogram) when compared to Figure 1.1. It is interesting to note that the furthest exoplanet systems were discovered via microlensing, while planets discovered by RV are mostly limited to the solar neighborhood.

1.2.3 Direct Imaging and the Kozai Mechanism

RV and transit detections of companions are, by their nature, biased towards short-period companions. Direct imaging with diffraction-limited imaging, through AO (Skemer et al. 2012, 2014, e.g.,) or Speckle imaging (e.g., Horch et al. 2009; Howell et al. 2011), on the other hand, is more likely to find long-period companions (see triangles in Figure 1.5). Finding long-period companions to stars with known short-period companions have allowed for investigations of the importance of the Kozai

mechanism in the formation of hot Jupiters and close binaries. Traditionally, it has been difficult to explain how two relatively equal-mass binaries can end up at such small separations as they have been observed. The Kozai mechanism allows for a long-period, large separation companion to drive a closer-in companion towards the body it is orbiting (Kozai 1962). Wu & Murray (2003) study a case where a companion at 1000 AU leads to the formation of a hot Jupiter through this mechanism, and Fabrycky & Tremaine (2007) study both the formation of hot Jupiters and two close stars due to Kozai interaction with a distant companion.

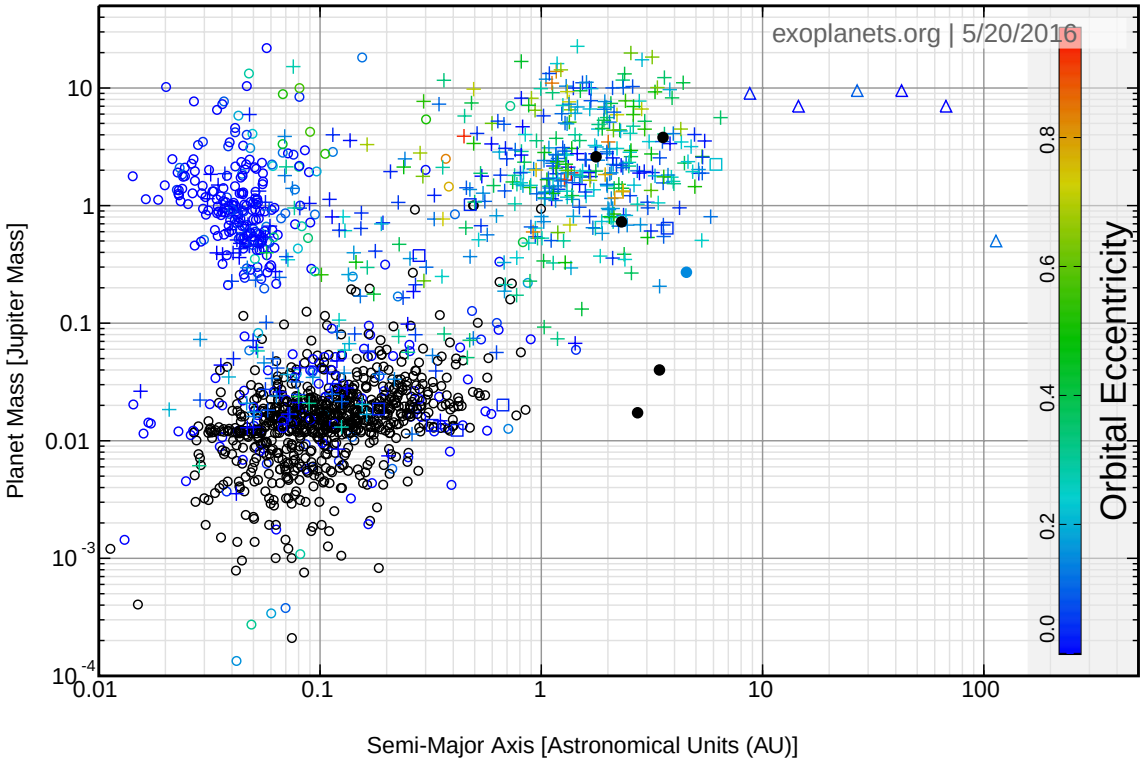

Fig. 1.5.— The orbital distribution of exoplanets and BDs in the exoplanet.org database, with companion mass on the ordinate and semimajor axis on the abscissa. Symbol color is the orbital eccentricity of the companion, and the symbol shape is the method of detection as in Figure 1.3.

1.3 The Role of APOGEE

Many of the aforementioned discoveries came through small and large-scale stellar transit monitoring, the use of single-object spectroscopy, or the combination thereof. A logical step forward in this field if we truly want to build large statistical samples of companions is to use of large-scale, wide-field, multi-object spectroscopy to complement current and future large photometric surveys such as those by *Kepler* (Borucki et al. 2010) and TESS (Ricker et al. 2014a). The Sloan Digital Sky Survey III (SDSS-III; Eisenstein et al. 2011) Multi-object APO Radial Velocity Exoplanet Large-area Survey (MARVELS; Ge et al. 2008) used this approach to observe $\sim 10,000$ stars and discovered several BD and low-mass stellar companions (Lee et al. 2011; Wisniewski et al. 2012; Fleming et al. 2012; Jiang et al. 2013a; Mack et al. 2013; De Lee et al. 2013; Wright et al. 2013; Jiang et al. 2013b). Unfortunately, stability issues with the instrument lead to a much smaller yield than initially anticipated.

1.3.1 APOGEE Overview

The SDSS-III Apache Point Observatory Galactic Evolution Experiment (APOGEE-1 Majewski et al. 2015) is a large-scale, systematic, high-resolution ($R = 22,500$), H-band ($1.51\mu\text{m} < \lambda < 1.69\mu\text{m}$), spectroscopic survey of the chemical and kinematical distribution of Milky Way stars. APOGEE-1 acquired high S/N (> 100) spectra of over 146,000 stars distributed across the Galactic bulge, disk, and halo. To achieve this S/N, many of the stars had to be observed for long net integration times – up to 24 hours. To accomplish this goal, and to gain sensitivity to temporal variations in radial velocity (RV) indicative of stellar companions, the APOGEE survey observed most stars over multiple epochs. In three years of SDSS-III operation, APOGEE-1 observed over 14,000 stars enough times (≥ 8) and over a sufficient temporal base-

line to collect spectra yielding high quality RV measurements suitable to not only reliably detect RV variability, but also to construct reliable Keplerian orbital fits to search for companions of a wide range of masses. With a typical radial velocity precision of ~ 100 m s^{-1}, APOGEE can detect RV oscillations typical of those expected from relatively short-period companions down to a few Jupiter-masses ($10^{-3} M_{\odot}$). And because of APOGEE's design as a systematic probe of Galactic structure, this sample probes stellar populations not traditionally sought in exoplanet and stellar multiplicity studies in regions of the Milky Way well beyond the solar neighborhood.

1.3.2 APOGEE Radial Velocity Observations

All APOGEE-1 observations were taken using fibers connected to either the Sloan 2.5 m telescope (Gunn et al. 2006) or the NMSU 1-m telescope at Apache Point Observatory (APO; Majewski et al. 2015). In normal use on the Sloan 2.5 m telescope, APOGEE employs a massively multiplexed, fiber-fed spectrograph capable of recording 300 spectra at a time. For full details on the APOGEE instrument see Wilson et al. (2015).

Of the 146,000 stars observed in APOGEE-1, 14840 had at least eight visits; these stars were selected for analysis here. APOGEE first light observations were obtained in May of 2011 and APOGEE-1 observations concluded at the end of SDSS-III in July of 2014, providing a maximum temporal baseline of slightly more than three years ($\sim$1000 days). Figure 1.6 shows the distribution of temporal baselines for stars submitted for Keplerian orbit fitting, as well as the distribution of the number of visits to each of these stars. An APOGEE "visit" is defined as the combined spectrum of a source from a single night's observations, typically ~ 1 hour of exposure. For main survey targets, the number of visits scheduled for a star depends on its H magnitude,

with fainter targets needing more visits to acquire the APOGEE target accumulated S/N of 100 per half-resolution element. For stars with at least eight visits, individual visit spectra obtained a median S/N of 12.2. Visits are required to be separated by $\geq$3 days, and must span $\geq$30 days at minimum to gauge the potential binarity of the source. Special targets such as stars used for calibration or ancillary science programs often have additional visits and employ a non-standard cadence. For example, some stars observed during commissioning were re-observed at the end of the survey as a consistency check (see §3.4.2), so these stars may have visits separated by over two years. For a more detailed description of APOGEE targeting and observing strategy see Zasowski et al. (2013) and Majewski et al. (2015).

1.4 Thesis Organization

In this chapter we have seen how the fields of exoplanets, brown dwarfs and binary stars have evolved from studies of single objects to statistical population studies, and have introduced APOGEE's role in this nascent field of substellar companion host populations. We present the operation and verification custom-built automated Keplerian orbit fitting pipeline in chapter 2, as well as the candidate selection criterion, used to derive the many of the results of this thesis. Chapter 3 describes global properties of the "gold sample" of companion candidates derived from the APOGEE DR12 database(Holtzman et al. 2015), as well as some "extreme systems." Both chapters 2 and 3 were drawn from Troup et al. (2016), and use results derived from APOGEE DR12 data. In chapter 4, I describe my contributions to improvements to the APOGEE data reduction pipelines, namely the inclusion of stellar rotational velocities in ASPCAP and improved methods for RV extraction and visit combination for low S/N sources, and their impact on the ability of APOGEE to detect

companions. In Chapter 5 we present new data and techniques used to generate the APOGEE DR14 catalog of companion candidates. We compare this catalog to the DR12 catalog to test the robustness of our detections, and we explore the potential origins of the numerous brown dwarf companions as well as other interesting systems in this catalog. Chapter 6 describes data collected from external observatories, as well a work I performed in preparations for future survey efforts with the APOGEE instrument. In particular, here we describe the proposed After Sloan 4 program, the APOGEE Time-Domain Legacy Survey (ATLaS). The final chapter summarizes the work and findings presented in this thesis, as well as describes APOGEE and ATLaS's place in a new era of population studies of stellar and substellar companion hosts.

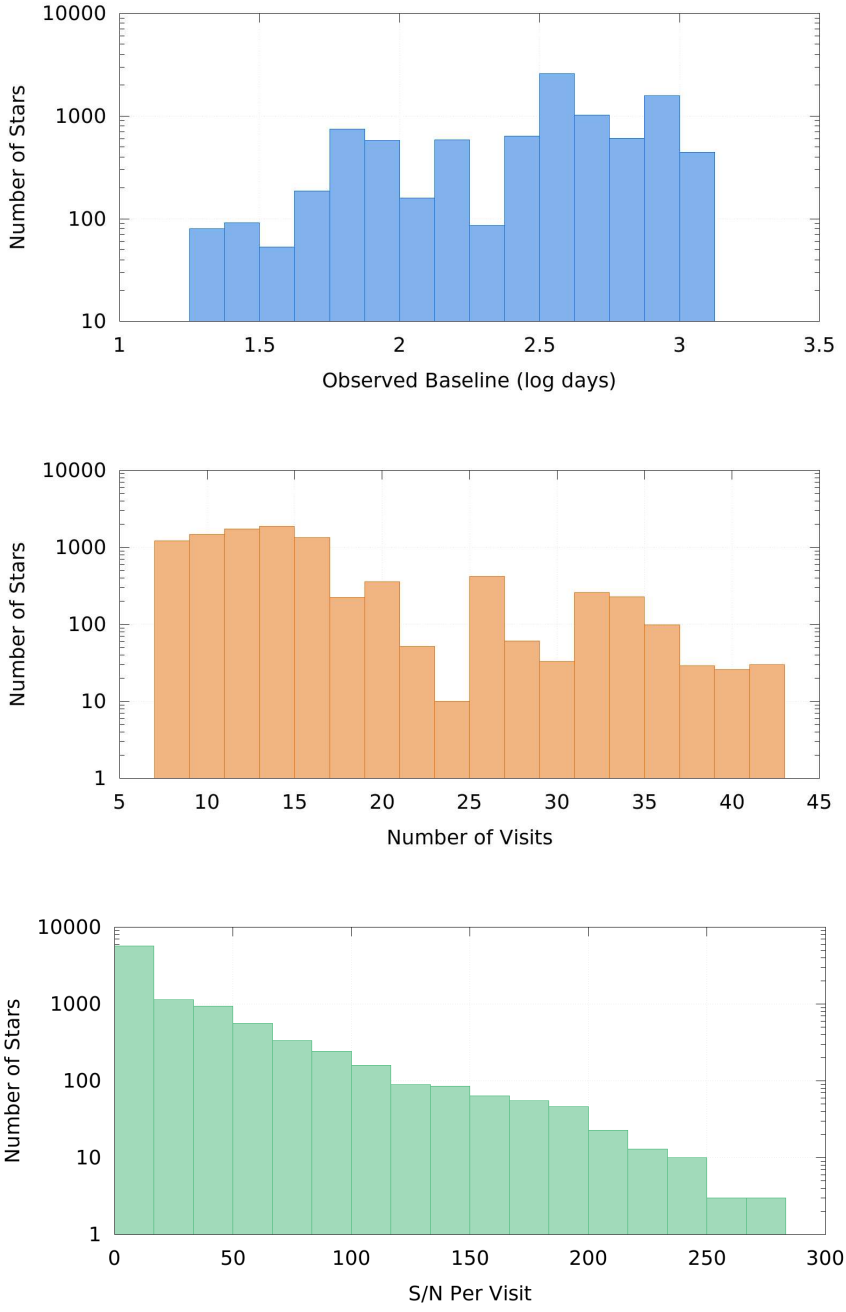

Fig. 1.6.— *Top Panel:* Distribution of the observed baseline for the 14840 APOGEE-1 stars with at least eight visits. The median baseline for this set of stars is slightly over a year at 384 days. *Middle Panel:* Distribution of the number of visits to the same set of stars, with a median of 13 visits. *Bottom Panel:* Distribution of the average S/N per visit for the same set of stars, with a median S/N per visit of 12.2.

Chapter 2

The `apOrbit` Pipeline and the Selection APOGEE Companion Candidates

While studies of individual systems can carefully inspect and tweak each star's RV curve, companion searches with large surveys like APOGEE require a robust automated pipeline and candidate selection procedure that can quickly and reliably deal with tens of thousands of stars without the need for human intervention. In this chapter we present our custom-built Keplerian orbit fitting pipeline used throughout this dissertation. This chapter describes the initial configuration of the pipeline, which was used to derive the results in Chapter 3. Upgrades and changes to the pipeline will be described in later chapters. However, the basic principles and operation of the pipeline outlined in this chapter largely remain unchanged throughout the work presented in this thesis.

Since the performance of the pipeline depends critically on an understanding of the RVs and their uncertainties, we first review those aspects of the data reduction

process most relevant to the derivation of the RVs, and determination of stellar parameters. For more information on processing steps that lead to the creation of the individual visit spectra, as well as more information regarding the main APOGEE data reduction pipeline (`apogeereduce`) see Nidever et al. (2015). After producing the individual visit spectra, `apogeereduce` performs initial radial velocity corrections on the visit spectra (described briefly in §2.1), and combines them into a single spectrum for each star. The APOGEE Stellar Parameters and Chemical Abundances pipeline (ASPCAP García Pérez et al. 2015) then matches this combined spectrum to a library of synthetic spectra (Zamora et al. 2015), constructed by using extensive atomic/molecular linelists(Shetrone et al. 2015), automatically delivering accurate stellar atmospheric parameters ($T_{\rm eff}$ within ∼100 K, $\log g$ and [Fe/H] within ∼ 0.1 dex) and the abundances of up to 15 chemical elements (Fe, C, N, O, Na, Mg, Al, Si, S, K, Ca, Ti, V, Mn, Ni). Both the model synthetic spectrum and stellar parameters derived for the star are used in the production of the final RVs used in orbit fitting as described in §2.1 and to derive the properties for the primary star as described in §2.2.

2.1 Derivation of Radial Velocities

The main APOGEE pipeline retains RVs from two methods: 1) The APOGEE reduction pipeline initially selects, through χ^2 minimization, an RV template from a coarse grid of synthetic spectra (the "RV mini-grid"). This template is cross-correlated against the spectrum to produce absolute RVs. 2) The pipeline cross-correlates the visit spectra with a combined spectrum of all visits and applies a barycentric correction to acquire heliocentric RVs. These RVs are stored as APOGEE data products.

To ensure the highest precision RVs, we preformed the additional step of using

the best-fit synthetic spectrum chosen by ASPCAP as our RV template. The grid of synthetic spectra used by ASPCAP is much finer than the RV mini-grid with additional dimensions to account for [α/M], [C/M], and [N/M]. In addition, the final model spectrum is achieved through cubic Bézier interpolation in the grid of spectra. Therefore, the ASPCAP best-fit template is a significant improvement over the RV mini-grid template and provides a high-quality match to the observed combined spectrum. This approach combines the advantages of using a noiseless synthetic spectrum as a template and using the combined observed spectrum to mitigate the chances of template mismatch. In the cases when mismatch did occurred (e.g., due to a poor or failed ASPCAP solution), we deferred to the RVs derived from the combined observed spectrum template. In either case, the RVs we used for orbit fitting were heliocentric RVs.

2.1.1 Analysis of RV Precision

To fully understand the types of companions to which we are sensitive, we need a clear understanding of dependencies of the RV precision on stellar parameters. Therefore, we created an analytical model of the RV precision based on the primary derived stellar parameters ($T_{\rm eff}$, $\log g$, [Fe/H]) and the S/N for each visit of the star. For the logarithm of the median RV error for each star, $\log \tilde{\sigma}_v$, of every star with at least 8 visits, excluding stars used as telluric standards and stars that have unreliable stellar parameters we fit a function that is linear in each parameter of interest:

$$\begin{aligned} \log \sigma_v = 1.56 + (4.87 \times 10^{-5}) T_{\rm eff} + 0.135 \log g \\ -0.518[Fe/H] - (5.55 \times 10^{-3}) S/N, \end{aligned} \tag{2.1}$$

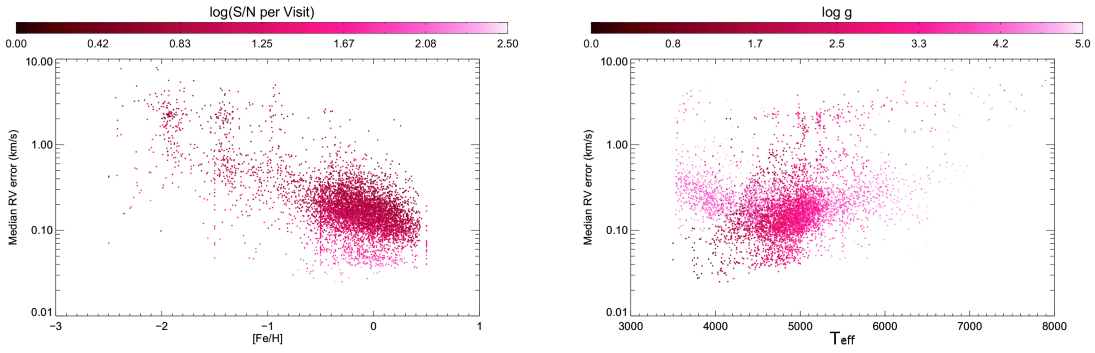

Fig. 2.1.— *Left Panel:* Precision of individual APOGEE visit RVs as a function of the metallicity ([Fe/H]) of the star with the color scale indicating the logarithm of the S/N per visit. *Right Panel:* Precision of individual APOGEE visit RVs as a function of the surface gravity ($\log g$) of the star with the color scale indicating the effective temperature ($T_{\rm eff}$) of the star.

where S/N is the signal-to-noise ratio of the visit spectrum from which the RV measurement was derived, and σ_v is in m s^{-1}. The left panel of Figure 2.1 displays two of the stronger effects on RV error: [Fe/H] and S/N per visit. The effects of $\log g$ and $T_{\rm eff}$ are illustrated in the right panel. These effects are closely related to the strength and number of absorption lines in the spectra. For a typical solar metallicity ([Fe/H]= 0) giant ($T_{\rm eff}$ = 4000K, $\log g$ = 3) and typical solar metallicity dwarf ($T_{\rm eff}$ = 5000K, $\log g$ = 4.5) stars with S/N = 10, we derive a typical RV precision of ∼130 m s^{-1} and ∼230 m s^{-1}, respectively per visit. These are the random RV uncertainties reported by the APOGEE pipeline, and are likely to be underestimates of the true uncertainty (see §3.4.2).

2.1.2 Selection of Usable RVs and RV Variable Stars

RV measurements from observations with $S/N < 5$, as well as RVs or errors that were unphysical, were not included in the final RV curves submitted to the orbit fitter. This reduced the number of stars for which Keplerian orbits could be attempted from 14840

to 9454 stars.

Likely RV variable stars were selected using the following statistic:

$$\text{stddev}\left(\frac{\mathbf{v}-\tilde{v}}{\sigma_{\mathbf{v}}}\right) \geq 2.5, \tag{2.2}$$

where $\mathbf{v}$ and $\sigma_{\mathbf{v}}$ are vectors of the RV measurements and their uncertainties, and $\tilde{v}$ is the median RV measurement for the star. The criterion was motivated by the false positive analysis presented in §2.5.1. There are also several additional pieces of information that we used to pre-reject stars that would have resulted in poor or erroneous Keplerian orbit fits. Therefore we also removed stars with the following criteria:

1. The system's primary must be characterized with reliable stellar parameters ($T_{\rm eff}$, $\log g$, [Fe/H]), so the ASPCAP `STAR_BAD` flag must not be set for the star. Our derivations of the RVs and the physical parameters of the system both rely on reasonable estimates of the stellar parameters of the host star.

2. The star cannot have been used as a telluric standard. These stars are selected for APOGEE observation for their nearly featureless spectra, so it is likely that RVs derived for these stars are unreliable and would lead to false positive signals. [1]

3. The combined spectrum from which the stellar parameters and RVs were derived cannot be contaminated with spurious signals due to poor combination of the visit spectra, so the `SUSPECT_RV_COMBINATION` flag must not be set for the star. This criterion also catches the double-lined spectroscopic binaries (SB2s) that would have resulted in poor stellar parameters, RVs, or orbital parameters from

[1] We backtrack from this particular criterion in later work (see §2.5.2 and Chapter 5)

our current pipelines.

This is not to say the stars excluded using this criteria do not have any sort of RV variation, but these stars are far more likely to have a false positive interpretation, so we elect not to include them.

2.2 Derivation of Primary Stellar Parameters

To determine masses of potential companions, a reasonable estimate of the primary star's mass is required. The measurement of masses for the primary stars in this sample is based on the spectroscopic stellar parameters ($T_{\rm eff}$, $\log g$, [Fe/H]) derived for each star. Between `apogeereduce` and ASPCAP, stellar parameters are derived up to three times for each source. The first approach uses the stellar parameters from the RV template selected for determining initial visit-level RVs. These parameters are available for every star, but are also the least precise of the three methods, so they should only be used as a last resort. The next set of stellar parameters made available are from the raw ASPCAP output. Except in the rare cases where ASPCAP fails to converge (which are removed from our final sample), these are available for all stars. Finally, calibrations are applied to the raw ASPCAP results based on comparisons with manual analysis of cluster stars (Meszaros et al. 2013; Holtzman et al. 2015). These parameters are only available for giant stars in a specific temperature range ($3500 < T_{\rm eff} < 6000$ K), but are the most reliable in absolute terms. To summarize, in order of preference, we adopted: (1) stellar parameters from the calibrated ASPCAP parameters, (2) uncalibrated ASPCAP parameters, (3) parameters used by the much coarser RV mini-grid.

All of the dwarfs in our catalog rely on uncalibrated parameters. Unfortunately this leads to systematically overestimated $\log g$ values for cool dwarfs when compared

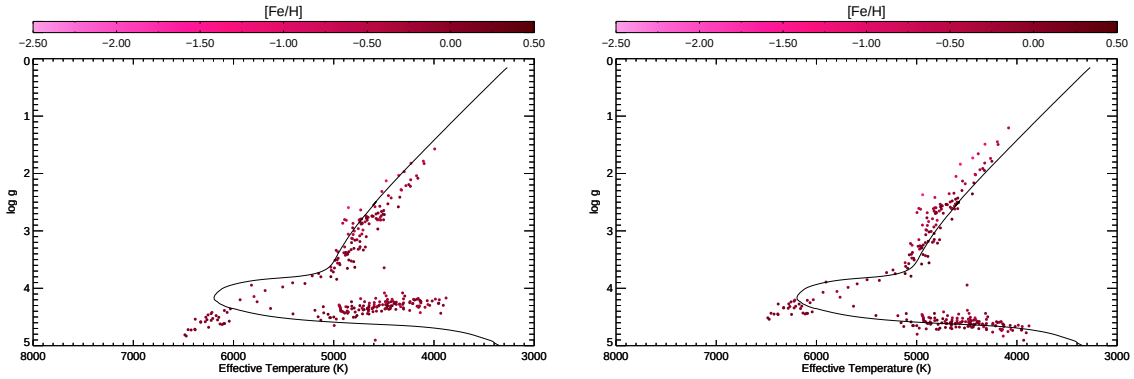

Fig. 2.2.— Spectroscopic HR diagrams of stars in the field of M67 observed by APOGEE with the stars' $T_{\rm eff}$ and $\log g$ as the abscissa and ordinate. The points are color-coded by host star metallicity. A 5 Gyr solar-metallicity isochrone is also included for comparison. *Left Panel:* Uncalibrated parameters (for both giants and dwarfs). Note the $\log g$ is underestimated by ~ 0.5 for stars at $T_{\rm eff} \sim 4000$ K. *Right Panel:* Calibrated parameters, with giants using the ASPCAP calibrated parameters and dwarfs adopting the $\log g$ correction from Equation 2.3.

to Dartmouth isochrones (Figure 2.2). We apply a simple linear correction to calibrate dwarf $\log g$ values:

$$(\log g)_{cal} = \log g - (3 \times 10^{-4})(T_{\rm eff} - 5500\,{\rm K}), \tag{2.3}$$

where $\log g$ and $T_{\rm eff}$ are the uncalibrated suface gravity and effective temperature. The results of this calibration can be seen in Figure 2.2.

2.2.1 Primary Star Classification

Before any further stellar properties are estimated, we divide the stars our sample into 5 classes defined by the following crteria:

1. **Pre-Main Sequence (PMS)** - Stars flagged in APOGEE as young stellar cluster members (IC348 and Orion).

2. **Red Clump (RC)** - Stars in the APOGEE RC Catalog (Bovy et al. 2014, for

the DR12 catalog).

3. **Red Giant (RG)** - Stars not selected as RC or PMS stars with

$$T_{\rm eff} < 5500\,{\rm K}, \tag{2.4}$$

$$\log g < 3.7 + 0.1[{\rm Fe/H}]. \tag{2.5}$$

The second relation was derived by mapping the $\log g$ of the base of the giant branch as a function of [Fe/H] from Dartmouth isochrones (Dotter et al. 2008) for typical ages expected of APOGEE giants.

4. **Subgiant (SG)** - Stars not selected as RC or PMS stars with

$$T_{\rm eff} > 4800\,{\rm K}, \tag{2.6}$$

$$\log g \geq 3.7 + 0.1[{\rm Fe/H}], \tag{2.7}$$

$$\log g \leq 4 - (7 \times 10^{-5})(T_{\rm eff} - 8000\,{\rm K}). \tag{2.8}$$

The second relation only applies for $T_{\rm eff} < 5500\,{\rm K}$. The third relation was determined by the $\log g$ at the highest $T_{\rm eff}$ of Dartmouth isochrones at a variety of ages and [Fe/H], roughly mapping the main-sequence turnoff (MSTO), and fitting a liner function to these points.

5. **Dwarf (MS):** Any star that does not fit into any of the above categories are classified as MS stars.

These classifications are saved for the catalog, and illustrated in Figure 2.3.

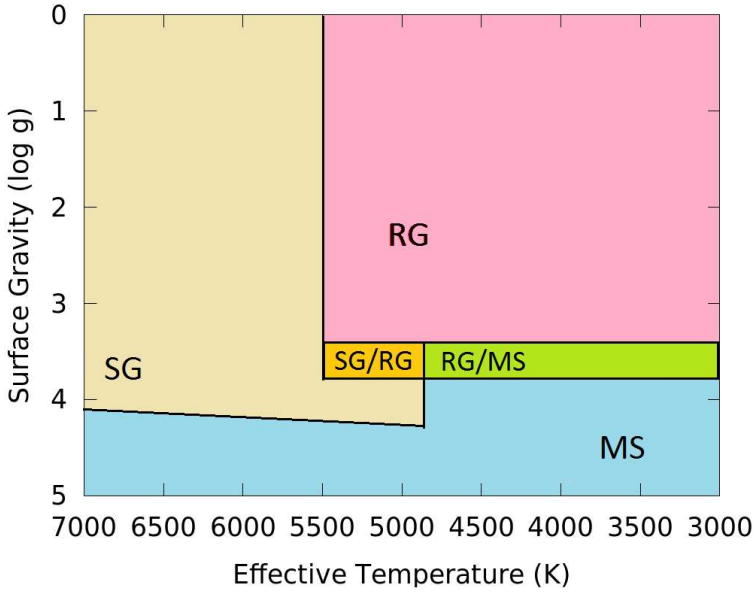

Fig. 2.3.— Classification scheme of Red Giant (RG), Subgiant (SG), and main-sequence dwarf stars (MS) in $\log g$ – $T_{\rm eff}$ space. Red Clump (RC) and pre-main sequence stars (PMS) transcend these boundries as they selected through alternate means. Region labeled with SG/RG or MS/RG are regions where the star can be either classification depending on its metallicity. The upper left corner of this plot does not contain any stars in our sample, so the SG classification there is simply in place to cover the phase space.

2.2.2 Derivation of Bolometric Magnitudes

In addition to stellar parameters, we need an estimate of the bolometric magnitude of our stars to compare to the bolometric luminosities we calculate and use in the following derivations of the masses and radii of the primary stars. We adopt the extinction coefficient, A_K from the APOGEE targeting data (Zasowski et al. 2013). If the APOGEE targeting A_K is not populated or is less than zero, then we adopt the WISE all-sky K-band extinction. If this source is negative, or not populated, as well then we assume $A_K = 0$. In the rare case ($< 1\%$ of APOGEE stars) that neither quantity is available, we assume $A_K = 0$, and flag the star. The extinction-corrected

K_s magnitude is then $K_0 = K_s - A_K$. We derived the bolometric correction to the 2MASS K_s band from Dartmouth isochrones:

$$BC_K = (2.7 + 0.15[\mathrm{Fe/H}]) - (25 + 0.5[\mathrm{Fe/H}])X^{2-0.1[\mathrm{Fe/H}]}e^{-X} \tag{2.9}$$

for PMS, dwarf and SG stars, where $X = \log T_{\mathrm{eff}} - 3.5$, and

$$BC_K = (6.8 - 0.2[\mathrm{Fe/H}])(3.96 - \log T_{\mathrm{eff}}) \tag{2.10}$$

for RG and RC stars. This correction yields the bolometric magnitude of the star: $m_{bol} = K_0 - BC_K$.

2.2.3 Derivation of Dwarf and Subgiant Primary Mass, Radius, and Distance

For stars selected as dwarf and subgiant stars, we adopted the Torres et al. (2010) relations to estimate the mass and radius of the primary star:

$$\log M_\star = a_1 + a_2 X + a_3 X^2 + a_4 X^3 a_5 (\log g)^2 + a_6 (\log g)^3 + a_7 [\mathrm{Fe/H}], \tag{2.11}$$

$$\log R_\star = b_1 + b_2 X + b_3 X^2 + b_4 X^3 + b_5 (\log g)^2 + b_6 (\log g)^3 + b_7 [\mathrm{Fe/H}], \tag{2.12}$$

where $X = \log T_{\mathrm{eff}} - 4.1$ and the coefficients, a_i and b_i are given in Table 4 of Torres et al. (2010). This empirical relationship has a scatter of 6.4% in mass and 3.2% in radius, so for dwarfs and subgiants, we adopt $\sigma_{M_\star} = 0.064 M_\star$ as the uncertainty in the mass, and $\sigma_{R_\star} = 0.032 R_\star$. This information allows one to estimate the luminosity,

$L_\star$, as well as the distance,d, to these stars:

$$L_\star = 4\pi R_\star^2 \sigma_{SB} T_{\rm eff}^4 \tag{2.13}$$

$$M_{bol} = 4.77 - 2.5 \log\left(\frac{L_\star}{L_\odot}\right) \tag{2.14}$$

$$d = 10^{1+0.2(m_{bol}-M_{bol})}, \tag{2.15}$$

where M_{bol} is the star's absolute bolometric magnitude. Uncertainty for these parameters are also derived through normal propagation of uncertainties, which yields a 13.5% typical distance uncertainty for dwarfs and subgiants.

Unfortunately, the Torres et al. (2010) relations fail when applied to giant and pre-main sequence (PMS) stars. For example, using the Torres et al. (2010) relations to derive the mass of Arcturus ($T_{\rm eff}$ = 4286 K, $\log g$ = 1.66, [Fe/H] = -0.52) yields a mass of $3.5 M_\odot$ compared to the accepted mass of $1.08 M_\odot$ (Ramírez et al. 2010). Therefore, we must resort to alternate methods for estimating the mass of the primary.

2.2.4 Derivation of Giant and Pre-Main Sequence Primary Mass, Radius, and Distance

Efforts are currently underway to compile all published (or soon-to-be published) distance measurements to APOGEE stars. For stars selected as RG and RC stars, we employ a preliminary version of this distance catalog as the basis for our mass derivation. The most accurate distances for APOGEE stars are those derived from asterosiesmic parameters from the APOGEE-Kepler catalog (APOKASC Pinsonneault et al. 2014, for the DR12 catalog). These distances were our first choice because they only have $\sim$ 2% random errors (Rodrigues et al. 2014). Unfortunately, no stars in our sample matched APOKASC stars with distance measurements, but we include it

in the pipeline in hopes that future versions of the APOKASC catalog will overlap with future versions of this catalog. Our second choice, if the star is a RC star, is to use distances derived from APOGEE RC catalogs. These distances are cited to have $5-10\%$ random errors in Bovy et al. (2014) If the star has neither of the above distances available, we adopted the spectrophotometic distance estimates derived by Santiago et al. (2015), Hayden et al. (2015), or Schultheis et al. (2014) for DR12, based on which estimate has the lowest error. Of course for later data releases, distance catalogs such as these will be expanded and updated, and will be used in future versions of this catalog. These distances generally have $< 15-20\%$ uncertainties. The PMS stars, as selected are all intentionally targeted young embedded cluster members. If there is no spectrophotometric distance available for these stars, we adopt the distance to their host cluster as the approximate distance to these stars [2]. From the adopted distance, d, we estimate the luminosity of the star, and thus its radius and mass:

$$M_{bol} = m_{bol} - 5\log(d) + 5 \tag{2.16}$$

$$L_\star = 10^{-0.4(M_{bol}-4.77)} L_\odot \tag{2.17}$$

$$R_\star = \sqrt{\frac{L_\star}{4\pi\sigma_{SB}T_{\rm eff}^4}} \tag{2.18}$$

$$M_\star = \frac{10^{\log g} R_\star^2}{G} \tag{2.19}$$

Following typical propagation of uncertainties, these techniques produce a mass uncertainty floor of 26% due to the uncertainty in $\log g$. The median of mass uncertainties for these techniques is around 28%.

If a giant star has no distance measurement available, we adopt a characteristic

[2]For example the 6 PMS stars from the DR12 catalog were located in the young cluster IC348, so all stars in that cluster were assigned the distance $d = 316 \pm 22$ pc citepHerbig1998.

mass from a TRILEGAL (Girardi et al. 2005) simulation using parameters typical of APOGEE giants. The median mass for all stars in this simulation with $\log g < 3.8$ and 3500 K$< T_{\rm eff} <$ 5000 K in the direction of Galactic Coordinates (ℓ, b) =(0,40) is $M_\star = 1.6 \pm 0.6 M_\odot$ ($\sim$ 40% mass uncertainty), which we adopt as the typical mass for all giant stars without a distance measurement. From this we derive $R_\star = (GM_\star/10^{\log g})^{1/2}$ and d, as for the dwarfs, both with typical estimated uncertainties of 25%. Fortunately, we only need to adopt this type of mass estimate for 1 star run through the apOrbit pipeline.

2.3 Keplerian Orbit Fitting

Once a star has mass and radius estimates, we can attempt to search for periodic signals and derive Keplerian orbits from its RV measurements. Only stars with at least eight "good" visits have enough degrees of freedom to attempt the six and seven parameter Keplerian orbit fits. For each star meeting this criterion, we attempt orbital fits with and without a long-term underlying linear trend. The linear fit accounts for additional long-term RV variability that may be indicative of an additional companion with a period longer than we can detect reliably.

2.3.1 Period-Finding and Selection of Initial Conditions

We employ the Fast χ^2 Period Search (Fχ^2) algorithm (Palmer 2009) to search for periodic signals in our data. This algorithm chooses the period based on the largest reduction in χ^2 between a sinusoidal fit employing the first n_h harmonics of a fundamental period, p_i, compared to a global n_d-degree polynomal fit. The Fχ^2 algorithm uses harmonics of the fundamental period in its fits, which produces improved performance with non-circular orbits compared to the traditional Lomb-Scargle algorithm

(Scargle 1982). Another advantage of the Fχ^2 algorithm is a built-in avoidance of periodic signals introduced by the cadence of the data, i.e., inputting data taken every n days will not return a n-day period as the best fit.

For our purposes, we employ three harmonics ($n_H = 3$), execute a search in four (logarithmic) period bins (0.3 to 3 Days, 3 to 30 days, 30 to 300 days, and 300 to 3000 days), and oversample ten times the default frequency sampling such that the frequency step is $\Delta f = 1/(10 n_h \Delta T)$, where ΔT is the longest temporal baseline of the observations. The search is executed once with a constant ($n_d = 0$) fit and once with a linear fit ($n_d = 1$). The periods in each bin, p_j that produce the greatest reduction in χ^2, $\Delta\chi^2_{max}$, are then assessed for their significance using the following criterion:

$$P_{n-2n_h}(\Delta\chi^2_{max}) \geq 0.997, \tag{2.20}$$

where $P_{n-2n_h}(\Delta\chi^2_{max})$ is the probability for a χ^2 distribution with $n - 2n_h$ degrees of freedom, and n is the number of RV epochs. The above limit is the equivalent of a 3σ detection. Periods that are not deemed significant by this metric are not used for full Keplerian orbit fitting. The significant periods (p_j) and their harmonics (1/3, 1/2, 2, and 3 times each value of p_j) are then each used for Keplerian orbit fitting.

2.3.2 Derivation of Keplerian Orbits

Once the best periods are identified, Keplerian models with those periods are fit to the RV measurements using the `MPFIT` algorithm (Markwardt 2009). `MPFIT` is a Levenberg-Marquardt non-linear least squares fitter implemented in IDL. This code is wrapped in an IDL code `MP_RVFIT` used in the MARVELS survey (De Lee et al. 2013). `MP_RVFIT` takes the input period and searches parameter space of the other

Keplerian orbital parameters (K, e, Ω, T_p,, and global velocity trends) and returns the Keplerian model that satisfies the period with the lowest χ^2.

Having a precise period is extremely important for acquiring an accurate Keplerian model, and simply submitting the periods from our period-finding algorithm to `MP_RVFIT` often leads to unsatisfactory results. Here we describe the bisector method implemented to refine our estimates of the best possible period. We initially submit the periods described above to `MP_RVFIT`, and keep the three periods ($p_{k,0}$) that produce the best fits based on the modified reduced-chi-squared goodness of fit statistic, χ^2_{mod}, described in §2.3.4. For each of these periods we implement a bisector method to narrow in on the exact period. For each p_k we run `MP_RVFIT` with three periods: $p_{k,0}$ and $p_{k,0} \pm \Delta p_0$, where $\Delta p_0 = 0.5 p_{k,0}$. We then compare the χ^2_{mod} for the best fits for the three periods, and update p_k and Δp accordingly:

$$\text{If } \chi^2_{p_{k,i}} \leq \chi^2_{p_{k,i} \pm \Delta p_i} \quad : \quad p_{k,i+1} = p_{k,i}, \ \Delta p_{i+1} = \Delta p_i / 2, \tag{2.21}$$

$$\text{If } \chi^2_{p_{k,i} \pm \Delta p_i} < \chi^2_{p_{k,i}} \quad : \quad p_{k,i+1} = p_{k,i} \pm \Delta p_i, \ \Delta p_{i+1} = \Delta p_i, \tag{2.22}$$

For the $\chi^2_{p_i - \Delta p_i} < \chi^2_{p_i}$ case, if $p_i - 2\Delta p_i < 0.1$, then we use $\Delta p_i = \Delta p_i / 2$ for the next update. This iteration is performed until the change in χ^2_{mod} is less than 0.01 or $n_{iter} = 50$ iterations are reached. The final values of $p_{k,n_{iter}}$ are then submitted to `MP_RVFIT` one final time, and the results saved for the catalog. The data saved are described in §2.4. For a few example Keplerian orbit models see Figure 2.4.

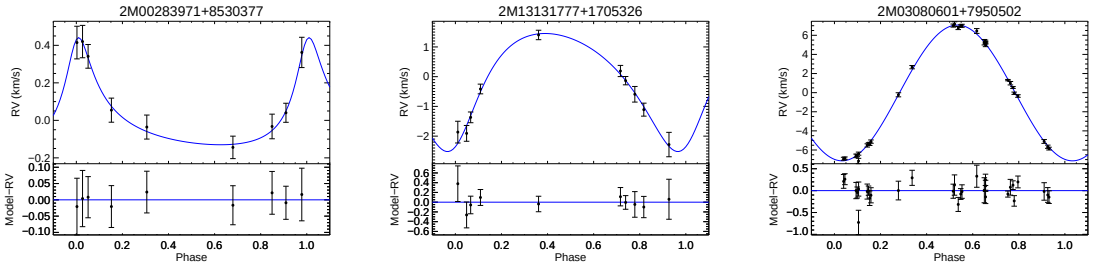

Fig. 2.4.— RV curves for a few example systems. In each plot, the top panel presents the phased RV measurements with a line showing the best fit model and the bottom panel shows the residuals of the fit. Similar figures are available online for every star in our gold sample (see §3.4). *Left Panel:* A planetary-mass ($m \sin i = 4.60 M_{Jup}$) companion in a $P = 41.3$ day, $a = 0.25$ AU orbit with $e = 0.566$, and $K = 0.29$ km s^{-1}. This orbit has uniformity index (See §2.3.4) values of $U_N = 0.886$ and $V_N = 0.737$. *Middle Panel:* A BD-mass companion ($m \sin i = 22.6 M_{Jup}$) companion in a $P = 24.3$ day, $a = 0.15$ AU orbit with $e = 0.293$, $K = 1.99$ km s^{-1}. This orbit has uniformity index values of $U_N = 0.871$ and $V_N = 0.935$. *Right Panel:* Binary System with a $m \sin i \approx 0.304 M_{\odot}$ secondary in a $P = 184$ day, $a = 0.68$ AU orbit with $e = 0.004$, $K = 7.11$ km s^{-1}. This orbit has uniformity index values of $U_N = 0.937$ and $V_N = 0.869$.

2.3.3 From Orbital to Physical Parameter Estimates

Directly from the orbital parameters, we can calculate the projected semi-major axis of the primary star:

$$a_\star \sin i = \frac{KP}{2\pi}\sqrt{1-e^2}. \tag{2.23}$$

From this measurement we can define the mass function of the system:

$$f(m, M_\star) = 4\pi^2 \frac{(a_\star \sin i)^3}{GP^2} = \frac{(m \sin i)^3}{(M_\star + m)^2}. \tag{2.24}$$

This quantity is saved in the catalog, but we also attempt to estimate the secondary mass directly:

$$m \sin i = \left[f(m, M_\star) M_\star^2 (1 + (m/M_\star))^2 \right]^{1/3} \tag{2.25}$$

The general case of this equation cannot be solved analytically, but often when dealing with planetary companions, we can make the assumption that $m \ll M_\star$, and thus can make the approximation $m \sin i \approx (f(m, M_\star) M_\star^2)^{1/3}$. For companions with $m \sin i < 0.1 M_\star$, this approximation is accurate to within 10%, but our sample contains higher-mass companions for which we want reasonable mass estimates. In these cases we solve the above equation iteratively, initially assuming $m = 0$, returning the above estimate, and iterating until $m \sin i$ changes by $< 10^{-4} M_\odot$. Since we are interested in estimating the minimum mass of the companion, we solve for the $\sin i = 1$ case, and thus use $m \approx m \sin i$ after the first iteration. This iterative method for determining m was tested for a variety of mass ratios and a variety of starting points for m (not just $m = 0$). From our tests, we have found this method to be quite robust.

Finally, from the estimate of $m \sin i$, we provide an estimate of the semimajor axis, a, of the secondary:

$$a = a_\star \sin i \frac{M_\star}{m \sin i}. \tag{2.26}$$

2.3.4 Quality Control and Selection of Best Fits

Finally we compile the three best models from the run with no global linear fit and the three best models from the linear fit run, and compare them to select the best overall fit. Ideally the phase and velocity coverage of the model are uniformly sampled by the data, and we aimed to preferably select models that are as close to this ideal

as possible. A useful way to quantify the phase coverage of the data is the uniformity index (Madore & Freedman 2005):

$$U_N = \frac{N}{N-1}\left[1 - \Sigma_{i=1}^{N}\left(\phi_{i+1} - \phi_i\right)^2, \right] \tag{2.27}$$

where the values ϕ_i are the sorted phases associated with the corresponding Modified Julian Date (MJD) of the measurement i, and $\phi_{N+1} = \phi_1 + 1$. This statistic is normalized such that $0 \leq U_N \leq 1$, where $U_N = 1$ would indicate a curve evenly sampled in phase space. Using a similar derivation, we also define an analogous "velocity" uniformity index with the same properties as U_N:

$$V_N = \frac{N}{N-1}\left[1 - \Sigma_{i=1}^{N}\left(\nu_{i+1} - \nu_i\right)^2\right]. \tag{2.28}$$

We define a "velocity phase," $\nu_i = (v_i - v_{min})/(v_{max} - v_{min})$, to have the same properties as ϕ_i above, where the values $\nu = 0$ and $\nu = 1$ indicate the minimum and maximum velocities of the *model*, v_{min} and v_{max}. The values of v_i are the radial velocity measurements, sorted by their value, with the adopted global velocity trend subtracted. For models that do not apply a global linear trend, the trend subtracted is the average of the raw velocities: $v_i = v_{raw,i} - \bar{v}_{raw}$. Measured velocities below the minimum or above the maximum are assigned $\nu = 0$ and $\nu = 1$, respectively. The purpose of this metric is to prevent the pipeline from selecting an extremely eccentric orbit when the data do not support such a model. Values of U_N and V_N are given in the example RV curves of Figure 2.4.

Combining the above statistic with the traditional reduced χ^2 goodness-of-fit

statistic (χ^2_{red}), we define the modified χ^2 statistic,

$$\chi^2_{mod} = \frac{\chi^2_{red}}{\sqrt{U_N V_N}}, \tag{2.29}$$

by which our models are ranked. In the case that $U_N = 0$ or $V_N = 0$, χ^2_{mod} would recorded as a floating-point infinity and automatically be ranked below all other fits. However, there are some conditions where the fit is unacceptable, but still may be selected as the best fit using the above metric. Therefore, we defined criteria that split the fits into "good" and "marginal" fits. Any of the following criteria would warrant a "marginal" classification:

1. Periods within 5% of 3, 2, 1, 1/2, or 1/3 day,
2. Periods, P, longer than twice the baseline, $2\Delta T$,
3. Extremely eccentric solutions ($e > 0.934$)[3],
4. Orbital solutions that send the companion into the host star: $a(1-e) < R_\star$,
5. Poor phase and velocity coverage ($U_N V_N < 0.5$).

The good and marginal fits are ranked by χ^2_{mod} separately, and the best fit is the good fit with the lowest χ^2_{mod}. If all of the fits were deemed marginal, then the best fit is the marginal fit with the lowest χ^2_{mod}. For more details on the verification and performance of the `apOrbit` pipeline, see section 2.5.

[3]This is the eccentricity of HD 80606 b, the largest eccentricity in the exoplanets.org database

2.4 Building the APOGEE Candidate Companion Catalog

In this section, we describe the data available for these stars, and the selection of companion candidates from the best Keplerian orbit fit to these stars. Information on catalog content and access can be found in §3.4.

2.4.1 Selecting Statistically Significant Astrophysical RV Variations

In many cases, the RV variations are within the measurement errors, so the derived semi-amplitude for the orbit may be masked by measurement error. In these cases, we cannot reliably state that the RV variations are astrophysical in nature. However, even astrophysical RV variations may not be due to the presence of a companion. Many stars, especially giant stars, which compose a large part of our sample, can have high levels of intrinsic RV variability. To estimate this stellar RV jitter, we adopted the relation found by Hekker et al. (2008b):

$$v_{jitter} = 2(0.015)^{\frac{1}{3}\log g}\ \mathrm{km\,s^{-1}}, \tag{2.30}$$

where, again, $\log g$ is the logarithm of the surface gravity in cgs units. We define a total RV uncertainty for each point in the model fit by combining this quantity with the RV measurement uncertainties, σ_v:

$$v_{unc} = \sqrt{\sigma_v^2 + v_{jitter}^2}. \tag{2.31}$$

We use the following criteria to select statistically significant companion candi-

dates:

$$\frac{K}{\tilde{v}_{unc}} \geq 3 + 3(1 - V_N)e, \tag{2.32}$$

where $\tilde{v}_{unc}$ is the median RV uncertainty of the model fit, K is the RV semi-amplitude of the best-fit model for the star, and V_N is the velocity uniformity index described in §2.3.4. We include the $(1-V_N)e$ term to increase the significance criteria for eccentric systems, particularly those that have poor velocity coverage. Thus, a perfectly covered eccentric orbit ($V_N = 1$) would be treated the same as a circular orbit ($e = 0$).

2.4.2 Refining the Catalog: Defining The Gold Sample

In an effort to minimize the number of false positives in our sample and reduce the number of systems with incorrectly-derived orbital parameters (see Section 2.5), we eliminate candidates that do not satisfy the following criteria:

- None of "marginal fit" criteria described in §2.3.4 are met.
- The Keplerian fits must be reasonably good, which we quantify as the criteria:

$$\frac{K}{|\Delta\widetilde{v}|} \geq 3 + 3(1 - V_N)e, \tag{2.33}$$

$$\chi^2_{mod} \leq \frac{K/|\Delta\widetilde{v}|}{3 + 3(1 - V_N)e}, \tag{2.34}$$

$$\chi^2_{mod} \leq \frac{K/\widetilde{v}_{unc}}{3 + 3(1 - V_N)e}, \tag{2.35}$$

  where $|\Delta\widetilde{v}|$ is the median absolute residuals of model fit. From simulations and visual inspection of orbits, orbits with large median K/v_{unc} or $K/\Delta v$ reproduced the correct parameters and had reasonable fits at much larger values of χ^2_{mod} than orbits with lower values. A major exception to this trend were large

$K/\widetilde{v}_{unc}$ orbits due to high e or orbits with poor velocity sampling (low V_N), so the metric above includes terms to penalize fits with high eccentricity ($1-e$ term) or low V_N (which inflates χ^2_{mod}) Therefore this "good fit" limit is stricter for such systems by employing the χ^2_{mod} metric discussed above. Previous cuts also guaranteed that no systems with $\chi^2_{mod} \leq 1$ are excluded because of this metric.

- The best fit must not require the maximum number of period iterations to converge; as described in §2.3.2. Systems that reach that maximum limit of iterations in the fitter did not converge on a solution, and the orbital parameters output are likely to be unreliable.

As mentioned above, many of these criteria were inspired by the testing of simulated systems with known orbital parameters described in Section 2.5.

2.5 Verification and Performance

As with all survey reduction pipelines, the goal is to balance speed and accuracy. Our code is reasonably fast, with a typical star taking 30-60 seconds for a complete fit to be performed, as described above. Below, we describe the efforts to verify the accuracy of the `apOrbit` pipeline.

2.5.1 Results from Simulated Systems

RV curves were generated for a suite of simulated systems to verify the output of the `apOrbit` pipeline. The simulations mimic the observations of candidate planet hosting stars by the APOGEE survey (see §2.8 of Majewski et al. 2015), and can be

used to investigate the types of systems that can be identified and characterized in the APOGEE-1 survey.

Generation of Simulated Systems

We simulated 9000 planetary systems with random characteristics. The masses of the primary stars were drawn from the distribution of estimated masses for the actual candidate substellar hosts in the APOGEE data. The companion masses and periods were drawn from the distributions specified by Tabachnik & Tremaine (2002), using a mass range of 1-100 M_{Jup} and periods from 0.1 to 2000 days. Eccentricities were drawn from a uniform distribution with a maximum of $e = 0.934$, which corresponds to the eccentricity of HD 80606 b, the largest eccentricity in the `exoplanets.org` database. Companions with $P < 5$ days were assumed to have circular orbits. The radii of the APOGEE candidate host stars were also estimated, and planets with orbital separations less than 5 $R_\star$ were considered unphysical because the tidal decay of planetary orbits becomes relevant at such small separations. The longitude of periastron and the orbital phase of periastron passage relative to a reference date were drawn from uniform distributions.

With the orbital characteristics of the simulated companions defined, we simply used the `helio_rv` code in the IDL astronomy users library[4] to calculate the measured heliocentric RV for each system on a set of observation dates. The observation dates for each system were designed to mimic the way the survey proceeded. The observations for each star were spread randomly over a 3.2 year time period assuming the telescope was on-sky for 15 days followed by 14 days off sky since APOGEE observed primarily during bright time. The simulated measured RVs consisted of the actual motion of the star at the time of observation plus two sources of noise, drawn from

[4] `http://idlastro.gsfc.nasa.gov`

Gaussian distributions. The first is simply measurement noise, which nominally has $\sigma_v = 100$ m s^{-1} but is increased to $\sigma_v = 130$ m s^{-1} for 20% of the visits to simulate poor observing conditions. The second noise source is intrinsic stellar atmospheric RV jitter, with an amplitude drawn from the distribution in Frink et al. (2001).

A second data set of 9000 simulated system were generated with much of the same parameters as the first, except that it had mass ratios approaching one, all orbital parameters were drawn from a uniform distribution, and it was much sparser in the lower-mass companion regime. We combined these two data sets to obtain complete coverage of parameter space. From the combined data set, we generated RV curves with 9, 16, and 24 visits selected from the 24-visit parent sample with the 100 m s^{-1} RV uncertainty level, as well as a set where the base uncertainty level is inflated to 1 km s^{-1} to emulate RV measurements from the metal-poor host stars in this sample.

Determination of Quality Criteria and False Positive Analysis

The full test suite of simulated systems was run through the `apOrbit` pipeline each time an update to the fitting algorithms was implemented. Many of these updates were inspired by the simulated systems for which the pipeline failed to reproduce the correct orbit in the previous run. In addition, many of the criteria used to select the RV variable and gold candidate sample, described in §2.4, were inspired by these results. Notable failures in previous runs that led to new selection criteria for candidate companions included:

1. **Long-Period Systems:** The longest-period simulated systems demonstrated the largest scatter in their results. This inspired the use of the phase uniformity index (see §2.3.4), as well as a procedure to reject any solutions for which the period was longer than twice the baseline (§2.4.2).

2. **Highly Eccentric Systems:** The code had the most difficulty reproducing the orbital parameters of systems with high eccentricity ($e > 0.9$). However, these systems are extremely rare, so this is not a major issue. Nevertheless, this result still led to the decision to reject all orbital solutions with $e > 0.934$ (§2.3.4), which is the planetary system with the largest known eccentricity anyway. Even with this cut, however, the more eccentric the system, the more trouble the code had in recovering the correct orbital parameters. In particular, systems with low numbers of visits had the most issues. This result inspired the use of the velocity uniformity index in the fitting code (§2.3.4), and it led to the decision to implement more stringent significance cuts for eccentric systems (§2.4.1).

3. **One-day Aliased Systems:** Early tests of the code on simulated systems revealed a tendency for solutions to cluster around integer fractions of one day, despite the initial period selection avoidance of such periods. This inspired the decision to reject any periods within 5% of 1/3, 1/2,1, 2, or 3 days (§2.3.4).

These simulations were also used to understand how RV noise from the star or measurement error can potentially lead to a false positive candidate companion. To accomplish this we ran the simulated systems through the `apOrbit` pipeline following the procedures laid out in §2.3 using just the RV signals from the star's atmospheric jitter and random measurement errors. We ran the simulations using four different numbers of visits (9, 12, 16, and 24) and two uncertainty levels (0.1 and 1 km s^{-1}), and selected candidates using the criteria described in §2.4. The results of the false positive tests are summarized in Figure 2.5. For systems with 24 visits, out of 18,000 simulated systems only two systems at the 1 km s^{-1} uncertainty level registered as false positives. The raw number of false positives increased dramatically from 24 to 16 visits, and the higher uncertainties lead to a higher rate of false positives. Most false

positives clustered around the sensitivity limit corresponding to the RV measurements from which they were derived (see Equation 2.36 below), and are generally assigned eccentric orbits ($e > 0.5$). This information, along with visual inspection of these fits, led to a pre-cut based on the velocity variations of the star which was based on the value of the statistic described in §2.1.2 for these systems.

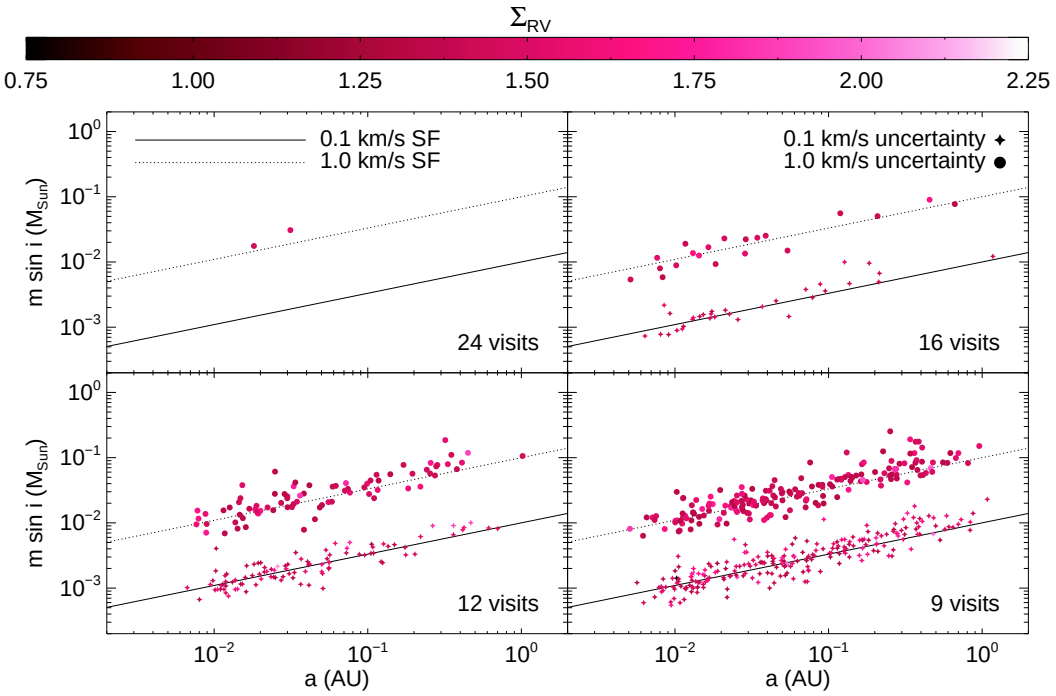

Fig. 2.5.— Distribution of false positive companions in recovered $m \sin i - a$ space, with color representing the Σ_{RV} statistic (see equation 2.2). Each set of points (unique color and shape) is drawn from a sample of 18,000 simulated systems with 9 (bottom right panel), 12 (bottom left panel), 16 (top right panel), and 24 (top left panel) simulated RV measurements based on stellar jitter and random measurement error. Symbol shape indicates the uncertainty level used for the simulation, with circles indicating 1 km s^{-1} and four-point stars indicating 0.1 km s^{-1} uncertainties. The solid and dotted lines show the approximate sensitivity function (SF; see Equation 2.36) for 0.1 and 1 km s^{-1} RV uncertainties. False positive signals such as these are removed from the sample via the velocity cut described in §2.1.2.

Sensitivity Limit, Parameter Accuracy, and Recovery Rate

In the results presented here, we ran the 18,000 simulated systems through the `apOrbit` pipeline as described in §2.3.2 for the four visit levels ($n_{RV} = 9, 12, 16, 24$) and two uncertainty levels ($\sigma_v = 0.1, 1$ km s^{-1}), and selected companion candidates in the same manner as the gold sample, as described in §2.1.2, 2.3.4, and 2.4. The systems correctly recovered (P and K recovered within 10%, and e recovered within 0.1) are shown in Figure 2.6. Systems with large K but small errors can lead to larger values of χ^2 for a fit that still produces the correct orbital parameters. Unfortunately, removing the χ^2_{mod} constraint allows many systems with incorrect solutions to pass, so we err on the side of caution and keep it in place. Due to limits of the period search and the other constraints on the period, a, and χ^2_{mod} of the fit described in §2.4.2, we expect to be able to recover orbits for companions having 0.01AU $\lesssim a \lesssim$ 3AU, depending on the baseline, number of visits, and the RV uncertainty level (see Figure 2.6). By fitting a trendline to the simulated systems with $2.8 \leq K/\tilde{\sigma}_v \leq 3$ for various values of σ_v, we also find that the lower limit on detectability, which we will refer to as the sensitivity function(SF), of $m \sin i$ can be written as:

$$\log(m \sin i) = 0.48 \log(a) - C, \tag{2.36}$$

where the constant offset, C, depends on the sensitivity level (which we interpret as the median RV uncertainty, $\tilde{\sigma}_v$):

$$C/\log(M_\odot) = 2.0 - 0.3 \log_2(\tilde{\sigma}_v / 100\,\mathrm{m\,s^{-1}}). \tag{2.37}$$

We then compared each observed/recovered orbital parameter, X_o, with the actual parameters for the system, X, to determine how accurately the parameters are

recovered as a function of parameter space. These results are summarized in Figure 2.7. For a large portion of the parameter space, the selected candidates reproduce the correct orbital parameters quite well. The systems that give the most trouble appear to be the low-mass companions, companions at large separations, and companions with highly eccentric orbits. Unsurprisingly, parameter recovery is overall worse for stars with fewer visits and higher RV uncertainties, but the drop in performance was not as dramatic between the 24 visit and 16 visit simulations as it was between the 16 visit to 9 visit simulations. However, from these results we can still conclude that in almost all regimes, the recovered orbital parameters are at least characteristic of the true values for the system.

Finally, we construct the recovery rates across the parameter space covered by this catalog. These are summarized in Figure 2.8. Unsurprisingly, recovery rate drops as n_{RV} decreases, and higher RV uncertainties lead to lower recovery rates in general.

2.5.2 Comparisons with Systems with Known Companions

In addition to comparing to the known parameters of simulated RV signals, we also compared our results to the transit periods of 5 Kepler object of interest (KOI) hosts and one non-KOI eclipsing binary (EB) observed by APOGEE (Fleming et al. 2015) that also meet the gold sample selection criteria described in §2.4. This comparison is presented in Table 2.1. We use the radius of the KOI as determined by *Kepler* transit data to split the sample. We assume a KOI with $R_{KOI} = R_{Jup}$ will have $m \sin i \approx M_{Jup}$, and therefore any KOI with a radius less than this will likely be undetectable by APOGEE.

For three of the five APOGEE-detectable KOIs and EBs in the gold sample, the transit period is reproduced almost exactly, and for the remaining two, it appears

that the `apOrbit` code simply selected the wrong harmonic for the period. For example, with KOI-1739, if we assume that the 146.9 day period found by APOGEE is the first harmonic of a fundamental period of 73 days, then the first harmonic period would be 219 days, which is much closer to the transit period. Most of the APOGEE-detectable KOIs have been designated as "False Positives" by the *Kepler* team, meaning that they the companion detected is not a planet, but rather a binary star companion. KOI-1739 is still designated as a candidate, but from APOGEE's RV data, we can conclude that this KOI should have a "false positive" disposition, as its companion is almost certainly not of planetary mass according to the analysis presented here. For the APOGEE-undetectable KOI, the APOGEE results from KOI-2598 may be indicative of longer-period companion previously undetected by transit. Further investigation of these this system is certainly warranted.

Furthermore, APOGEE recovered the known planet HD 114762b (2M13121982+1731016), with which we compare orbit parameters and host stellar parameters derived and adopted by the `apOrbit` pipeline to literature values in Table 2.2. APOGEE's recovered stellar parameters, as well as the recovered period and orbital semi-major axis are in good agreement with the results from Kane et al. (2011), but APOGEE overestimates the eccentricity of the system, and thus the values of K and $m \sin i$. This is in agreement with our findings in §3.4.2. However, this star was selected for use as a telluric standard, and thus is not included in our gold sample. This result may lead us to reconsider excluding stars selected as telluric standards in future versions of this catalog.

Table 2.1. KOIs and Kepler EBs Selected as DR12 Gold Sample Candidates

APOGEE_ID	KOI# (KIC ID)	$m \sin i$[a] (M_{Jup})	RV P[a] (days)	KOI P[b] (days)	R_{KOI}[b] (R_{Jup})	KOI[c] Disposition
KOI Likely Detectable by APOGEE ($R_{KOI} > R_{Jup}$)						
2M19263602+4242028	1739	622	146.0	220.6	···	Cand.
2M19335125+4253024	3546	261	4.286	4.286	2.45	FP (EB)[d]
2M19290626+4202158	6742	615	63.63	63.52	2.76	FP (EB)
2M19352118+4207199	6760	195	10.82	10.82	2.40	FP (EB)
2M19315429+4232516	(7037405)	667	103.3	207.15	···	··· (EB)
KOI Likely Undetectable by APOGEE ($R_{KOI} < R_{Jup}$)						
2M19291780+4302004	2598	111	274.4	2.69	0.093	Cand.

[a]Period as determined by APOGEE RV data (this work).

[b]Transit period as determined by *Kepler* transit data (Mullally et al. 2015).

[c]Official *Kepler* KOI disposition, which refers to the companion's status as a planet. If this field is blank, then the object is not a KOI, and the KIC ID is given for the star rather than a KOI number. A "false positive (FP)" disposition here indicates a companion that was found not to be of planetary mass, not the definition of false positive we used in the rest of this chapter to indicate RV measurements that masquerade as a non-existent companion.

[d]The star in the Kepler Eclipsing Binary (EB) catalog (Slawson et al. 2011; LaCourse et al. 2015)

Table 2.2. Comparison of Recovered Parameters of Known Exoplanet System HD 114762b

Parameter	APOGEE Value	Literature Value[a]
Host Stellar Parameters		
$T_{\rm eff}$	5466 K	5673 K
$\log g$	4.196	4.135
[Fe/H]	-0.832	-0.774
Distance	36.5 pc	38.7 pc
$M_\star$	0.86 $M_\odot$	0.83 $M_\odot$
$R_\star$	1.20 $R_\odot$	1.24 $R_\odot$
Orbital Parameters		
P	85.58 days	83.92 days
K	925.5 m s^{-1}	612.5 m s^{-1}
e	0.594	0.335
$m \sin i$	14.72 M_{Jup}	10.98 M_{Jup}
a	0.361 AU	0.353 AU

[a]Kane et al. (2011)

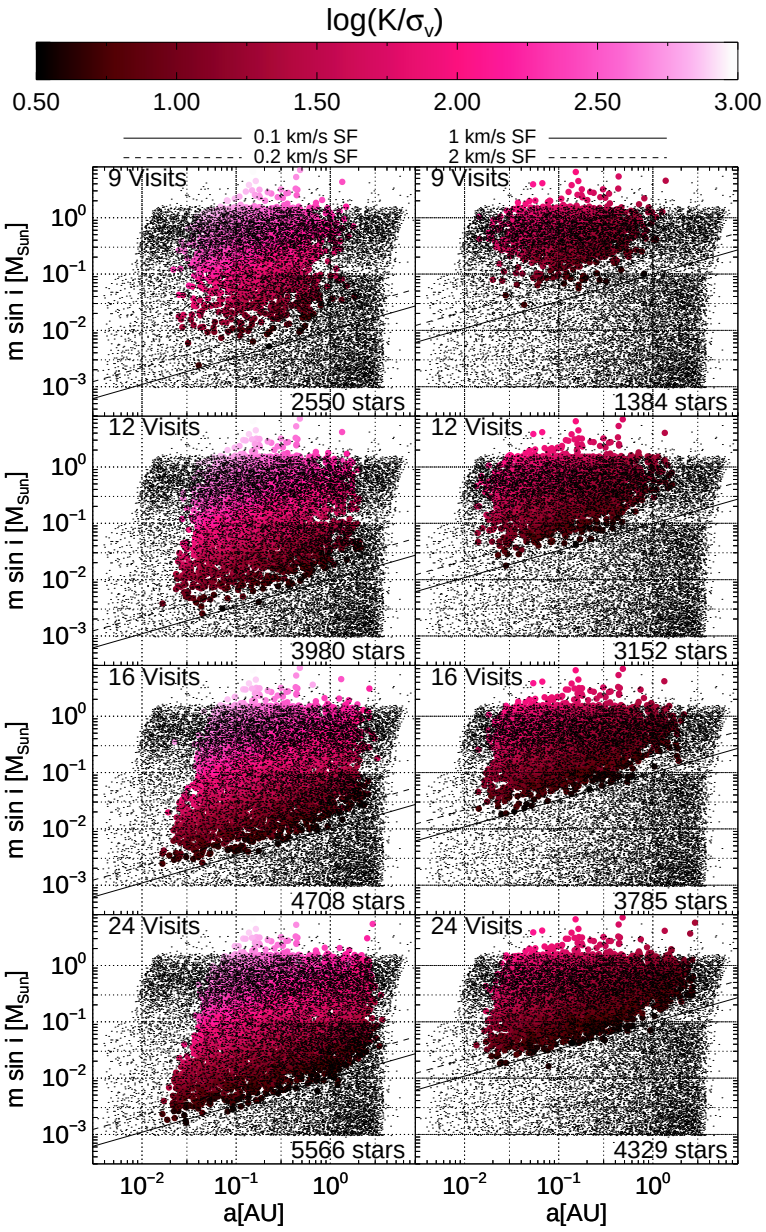

Fig. 2.6.— The grey dots represent the 18k simulated systems. The colored circles indicate the correctly recovered systems that were selected as candidates using the same metric as the "gold sample", color-coded by recovered $\log(K/\sigma)$, with the number of systems correctly recovered indicated in the bottom right corner of each panel. The black solid and dashed lines mark the sensitivity function (SF; equation 2.36) for the baseline and twice the baseline RV uncertainties of 0.1 km s^{-1} (left column) and 1.0 km s^{-1} (right column) used by the simulations. The simulations presented here emulate stars with, from top row to bottom row, 9, 12, 16, and 24 visits.

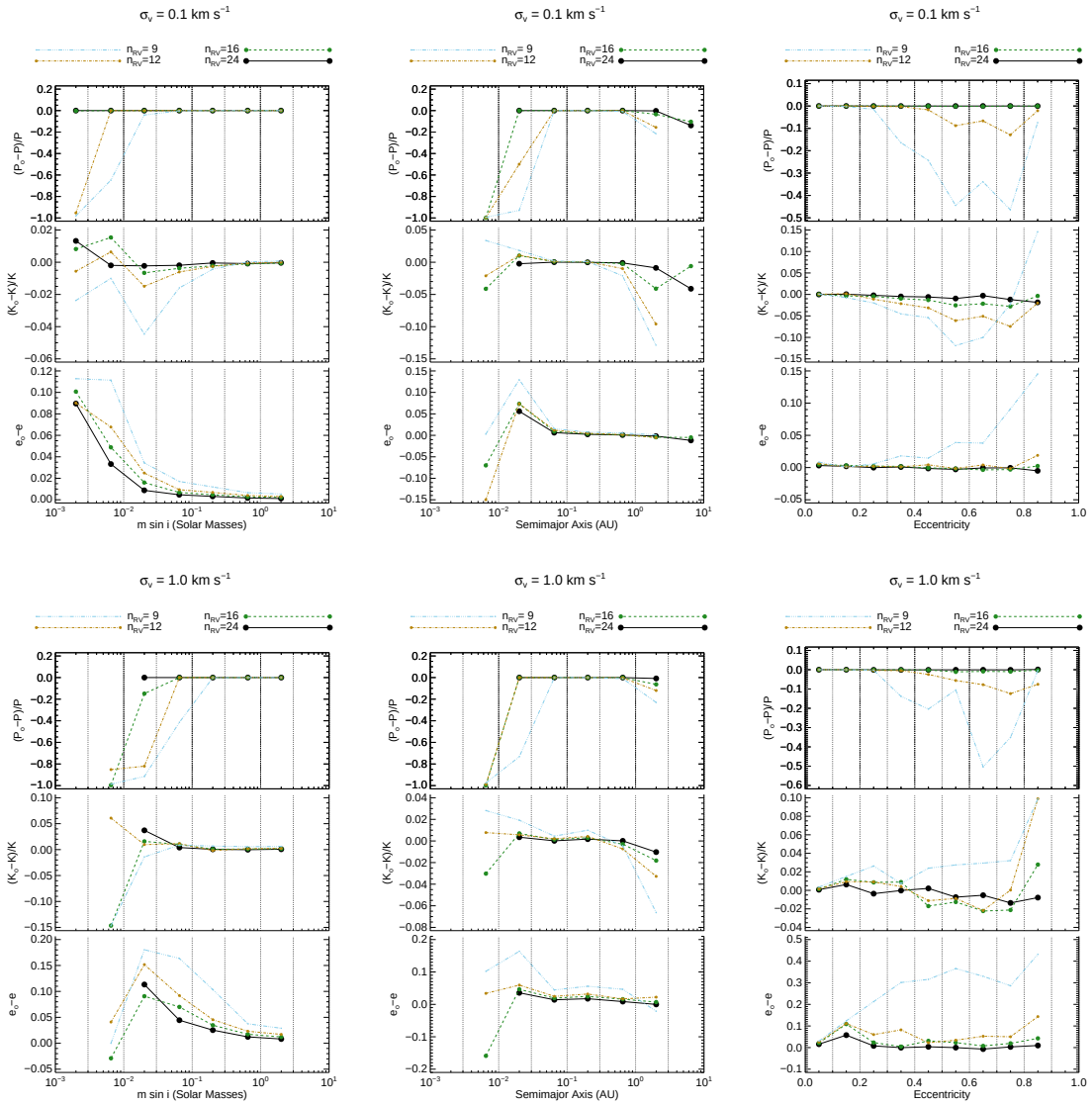

Fig. 2.7.— The recovered simulated systems binned by their recovered companion mass ($m \sin i$; left column), semimajor axis (a; center column), and eccentricity (e; right column). In each plot, the ordinates are the fractional error in period (top panel), fractional error in semiamplitude (middle panel), and eccentricity (bottom panel), where X_o indicates the recovered value of parameter with true value X. The top row of plots present the results using a base RV uncertainty of $\sigma_v = 0.1$ km s^{-1}, and the bottom row shows $\sigma_v = 1$ km s^{-1}. Red, green, blue, and black points (dash triple-dotted, dash dotted, dashed, and solid lines) are from simulations with 9, 12, 16, and 24 visits, respectively. The vertical dotted lines mark the bins used, and for any bin with < 3 stars, the point is excluded.

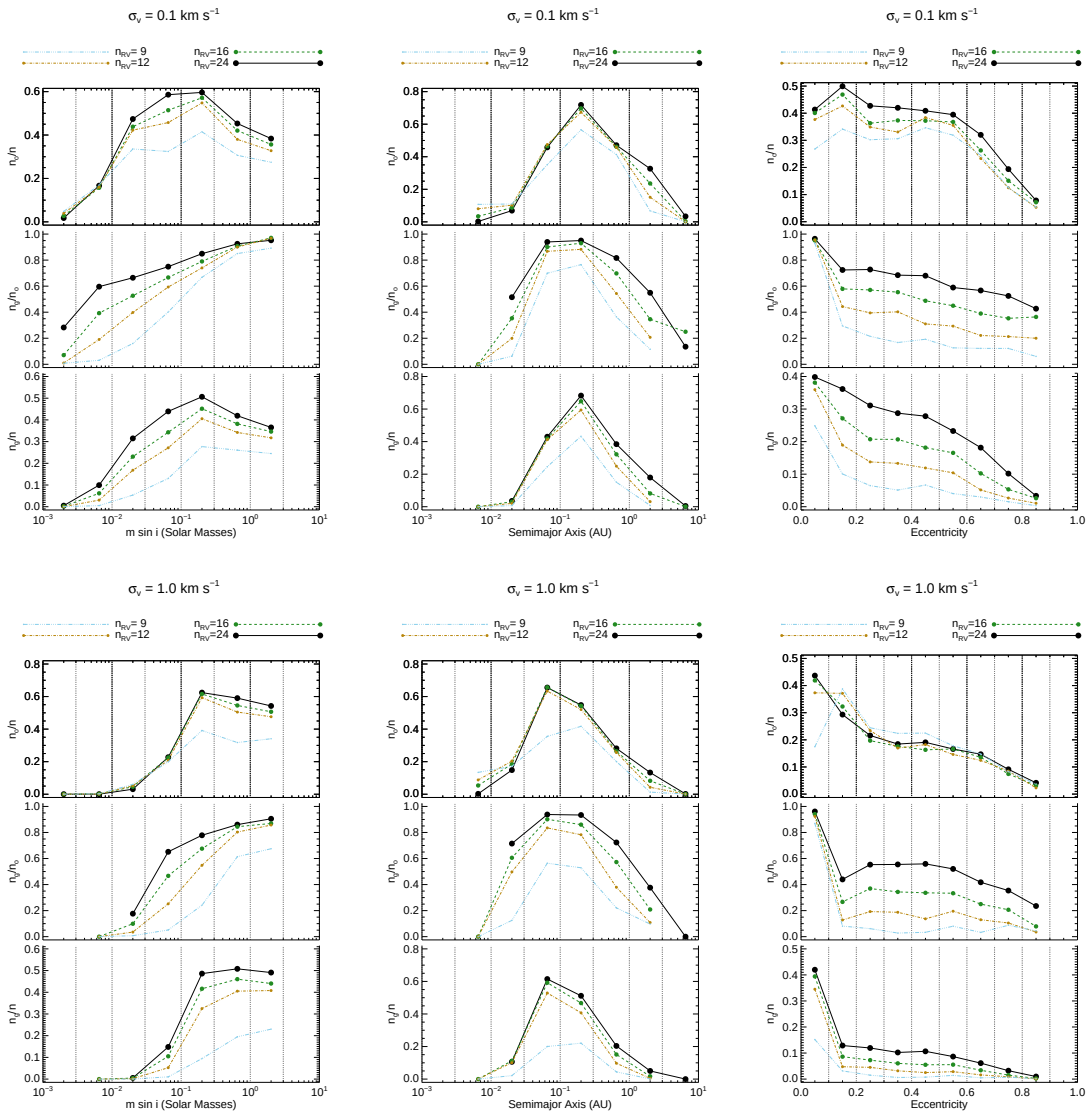

Fig. 2.8.— The same as Figure 2.7, except on the ordinate in each plot, the top panel shows the fraction of systems recovered in the bin, n_o, compared to the total number of simulated systems in the bin, n, the middle panel shows the fraction of systems recovered with correct orbital parameters (P and K within 10% and e within 0.1), n_g compared to n_o, and the bottom panel shows n_g/n. Here a bin is excluded if the denominator of the ordinate is < 2.

Chapter 3

Results from the First APOGEE Catalog of Companion Candidates

In this chapter we outline the results described in Troup et al. (2016), which were derived from the APOGEE data in the final data release of SDSS-III data (DR12 Alam et al. 2015) using the pipeline and procedures described in Chapter 2 (which is also presented in Troup et al. (2016)).

Using the pre-selection criterion described in 2.1.2, a total of 907 stars were selected to run through the `apOrbit` pipeline. Of these, the Fχ^2 period searching algorithm found significant periodic signals for 749, which were submitted for full Keplerian orbit fitting. Using the criteria described in 2.4.1, 698 stars are selected as statistically significant companion candidates. Using the refined "gold sample" selection criteria desribed in 2.4.2, 382 stars (55% of the statistically significant RV variable sample) were selected to be a part of our "gold sample," which represent the best-quality companion candidates in our sample. This is not to say that the other 45% of the statistically significant RV variable sample do not have companions, and there very well may be accurately reproduced companions from the non-gold sample.

However, the likelihood of either false positives or poorly-characterized systems is much higher for the non-gold sample than for the gold sample, hence we only present the 382 stars in the gold sample here.

In the following sections, we present a census of these 382 companion candidates. *Of these, 376 are newly discovered small separation companion candidates.* Table 3.1 provides a broad overview of the distributions of the companion candidates in terms of companion type (planet, BD or binary), host star type (e.g., giant vs. dwarf), and approximate Galactic environment (disk versus halo). We discuss each of these distributions and their implications in more detail in the sections below.

From this point on, we use $\langle m \rangle$ to indicate the maximum-likelihood value of the companion mass, m, based on the expectation value of i, defined as $\langle \sin i \rangle = \int_0^{\pi/2} P(i) \sin i \, di = \int_0^{\pi/2} \sin^2 i \, di = \pi/4$. Therefore, $\langle m \rangle = (4/\pi) m \sin i$, and we use this number to differentiate between companion types to account for inclination effects in a statistical manner.

3.1 Orbital Distribution of Companion Candidates

Figure 3.1 presents the overall distribution of $\langle m \rangle$ and orbital semi-major axis,a of the candidate companions in the gold sample. In this figure, there appears to be two distinct companion mass regimes in which the candidates lie, and thus suggests different companion formation channels. The upper regime is the binary star track, where the companion likely formed with (or shortly after) the primary from fragmentation of the cloud or disk from which the primary formed. The lower regime is the "planet" track, where the companion likely formed after the primary either through core accretion or gravitation instability in the disk surrounding the protostar. The trend of the lower planetary boundary mimics the sensitivity of the APOGEE survey

Table 3.1. A Census of APOGEE DR12 Gold Sample Companion Candidates

Population	Binaries[a]	BDs[b]	Planets[c]	Total
Host Star Classification[d]				
Red Clump (RC)	18	5	0	23
Red Giant (RG)	115	56	9	180
Subgiant (SG)	9	10	3	22
Dwarf (MS)	72	42	45	159
Host Star Metallicity				
$[\mathrm{Fe/H}] \geq 0$	70	36	13	119
$-0.5 \leq [\mathrm{Fe/H}] < 0$	118	62	42	222
$[\mathrm{Fe/H}] < -0.5$	25	14	2	41
Galactic Environment				
$\lvert Z\rvert < 1$ kpc	180	91	56	327
$1\,\mathrm{kpc} \leq \lvert Z\rvert < 5\,\mathrm{kpc}$	31	18	1	50
$\lvert Z\rvert \geq 5$ kpc	2	3	0	5
Catalog Totals	213	112	57	382

[a]Companions with $\langle m \rangle > 0.08 M_{\odot}$

[b]Brown dwarf companions: $0.013 M_{\odot} < \langle m \rangle \leq 0.08 M_{\odot}$

[c]Planetary-mass companions: $\langle m \rangle \leq 0.013 M_{\odot}$

[d]Host star classification discussed in §2.2.1

(see Equation 2.36 with $\tilde{\sigma}_v = 100$ m s^{-1}). However, the trend of the planet track's upper boundary cannot be explained by a selection or sensitivity effect. One interpretation of the gap between the two regimes is a manifestation of the BD desert in the data, but the two tracks appear to merge at larger semimajor axes ($a > 0.1 - 0.2$ AU). The implications of this are discussed below.

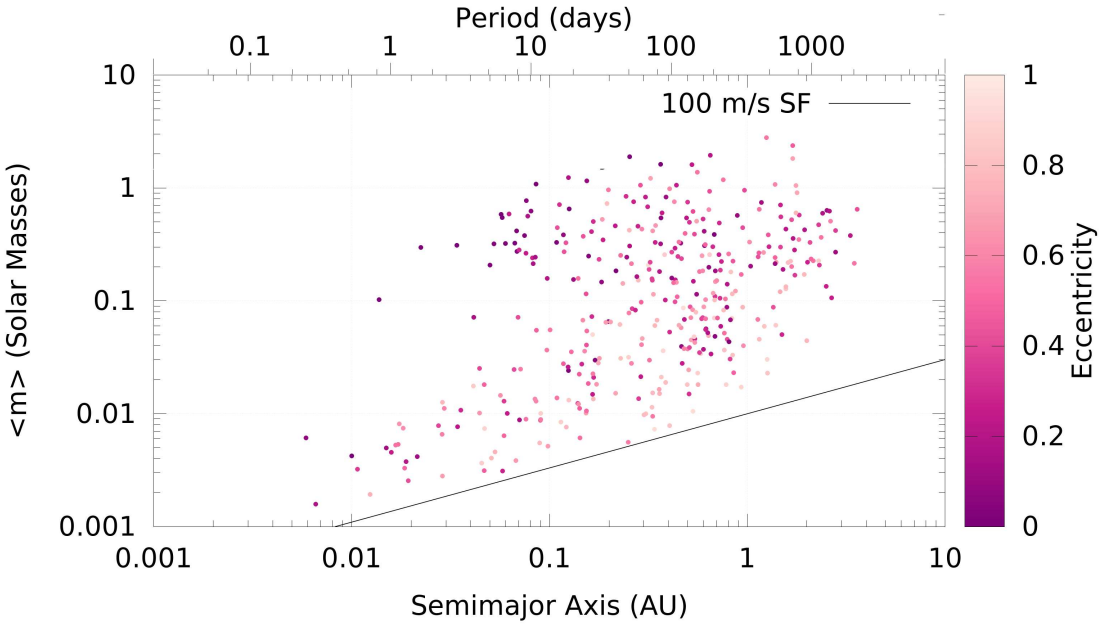

Fig. 3.1.— Orbital distribution of companion candidates in the 382-star gold sample with minimum orbital semi-major axis,a in AU on the abscissa and maximum-likelihood companion mass ($\langle m \rangle = (4/\pi) m \sin i$) in $M_\odot$ on the ordinate. The top horizontal axis gives the approximate period for the companion in days as well. Color represents the orbital eccentricity of the companion, with dark magenta representing circular orbits. The black line is the sensitivity function (SF; Equation 2.36) for 100 m s^{-1} RV precision. Systems below this line would generally be undetectable by APOGEE.

3.1.1 Combing the Brown Dwarf Desert

Figure 3.1 indicates that this sample reproduces the BD desert, but only for orbits with $a < 0.1 - 0.2$AU ($P < 10 - 30$ days), which is significantly less than the 3

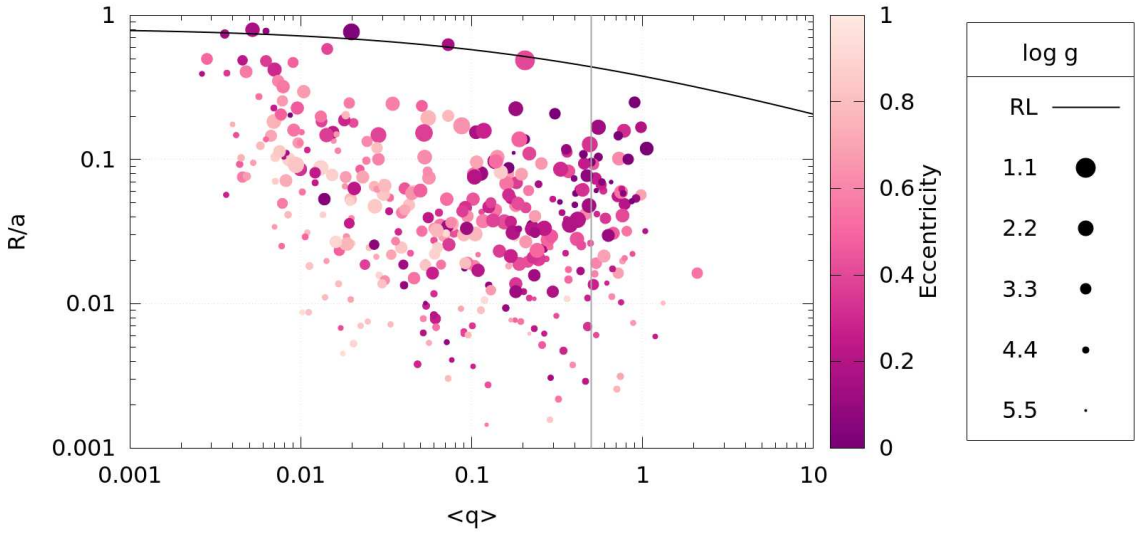

Fig. 3.2.— Orbital distribution of companion candidates with $\langle q \rangle = \langle m \rangle / M_\star$ on the abscissa, and $R_\star/a$ on the ordinate. Color again represents eccentricity, and point size indicates the surface gravity ($\log g$) of the host. The grey vertical line marks systems with $\langle q \rangle > 0.5$, and the black line across the top of the panel indicates the Roche limit (RL; Equation 3.1) of the host star.

AU extent of the desert as stated in Grether & Lineweaver (2006). However, their sample mostly considered solar-like dwarf hosts, while this sample contains stars with a variety of spectral types, as well as many evolved stars. From Figure 3.3, it appears that the relative number of BD companions decreases as host mass increases for MS hosts. Likely M dwarfs (MS with $M_\star < 0.6 M_\odot$) have roughly equal numbers of BD and stellar-mass companions, while K dwarfs (MS with $0.6 < M_\star/M_\odot < 0.85$) have roughly half the number of BD candidate companions as stellar-mass candidate companions. The G dwarfs (MS with $0.85 < M_\star/M_\odot < 1.1$) show a similar relative number of BD companions compared to stellar-mass companions, but they are less uniformly distributed throughout the BD mass regime compared to the lower mass BD candidate hosts, suggesting a higher probability that many of these BD candidates are scattered into the BD mass regime by inclination effects. These results leads

one to believe the interpretation of Duchêne & Kraus (2013) that the BD desert is simply a special case for solar-mass stars of a more general lack of extreme mass ratio ($q \lesssim 0.1$) systems. For example, if, in general, systems with $q < 0.08$ are rare (i.e., a BD companion around a 1 $M_{\odot}$ companion), then a relatively high-mass BD companion ($m > 0.04M_{\odot}$) orbiting a $0.5M_{\odot}$ star should be a more common occurrence.

Out of the 112 BD companion candidates in this sample, 71 orbit evolved stars. All but two of the giant (RC and RG) hosts have masses $> 0.8M_{\odot}$ and only one of the SG hosts has a mass $< 1M_{\odot}$. Considering that stars like the Sun lose up to a third of their mass on the RGB, it is a reasonable assumption that a vast majority of the evolved stars in this sample descended from main-sequence F (or earlier) dwarfs. As can be seen from Figure 3.4, the evolved stars have roughly half the number of BD candidate companions as stellar-mass candidate companions, and the BD-mass candidates are distributed throughout the BD-mass regime, similar to the K dwarf distribution. If the evolved stars are indeed evolved F dwarfs, and we follow the progression from above, one would expect these stars to have a smaller relative number of BD companions compared to even the G dwarfs. However, it has been previously suggested that the BD desert observed for Solar-like stars may cease to exist for F dwarf stars (Guillot et al. 2014). Their proposed explanation of this effect is that G dwarfs are more efficient at tidal dissipation. In general, compared to Jupiter-mass planets, more massive small separation companions undergo stronger tidal interaction with their host star through angular momentum exchange. Stellar-mass companions, however, have sufficient orbital angular momentum to remain in a stable orbit, which explains the demise of small separation BD-mass but not stellar-mass companions. However, dwarfs earlier than F are known to remain rapid rotators

($v_{rot} \sim 20-100$ km s^{-1}) throughout their main-sequence lifetimes due to their smaller outer convective zones leading to weaker magnetic breaking. This means F dwarfs are also less efficient at extracting angular momentum from an orbiting companion. Therefore, rapid rotators such as F dwarfs inhibit tidal dissipation, which explains this "F dwarf oasis" for BD companions. The dynamical model presented in Figure 4 of Guillot et al. (2014) shows that a companion in the BD-mass regime on an initial 3-day orbit around a $1M_{\odot}$ star will survive for $< 40\%$ of the star's main sequence lifetime ($\lesssim 4$ Gyr), while the same companion around a host star with $M_{\star} > 1.2M_{\odot}$ will survive for at least the entirety of the host star's main sequence lifetime (~ 6.5 Gyr for a $1.2M_{\odot}$ star). The presence of a large number BD companions orbiting the evolved stars in this sample strongly supports this "F dwarf oasis" hypothesis.

However, the tidal effects explanation would only strongly affect the closest-in companions. Since the rotation period of a G dwarf is $P_{\star} = 30$ days (compared to a few days for an F dwarf), tidal dissipation could only explain BD companions with orbital periods less than 30 days, and the majority of the BD candidate companions in this sample have periods significantly greater than that. Therefore, tidal dissipation can only explain the BDs (or lack thereof) with orbits within 0.2 AU. Curiously, this sample reproduces the BD desert out to approximately 0.2 AU, suggesting this mechanism may indeed play a role in shaping the BD desert. Another possible explanation for the presence of BD candidate companions is Roche lobe overflow of the star as it evolves off the main sequence onto an orbiting planetary-mass candidate, allowing it to grow to BD mass as the star evolves up the RGB. Eggleton (1983) gives the following approximation for the Roche lobe of a primary donor star with mass

M_1 orbited by a companion with M_2:

$$\frac{r_1}{a} = \frac{0.49q^{-2/3}}{0.6q^{-2/3} + \ln(1 + q^{-1/3})}, \tag{3.1}$$

where, $q = M_2/M_1$, a is the separation of the two bodies, and r_1 is the Roche lobe radius of the potential donor. In Figure 3.2, we mark the Roche lobe as a function of $\langle q \rangle$. As an interesting note, it appears there are seven stars in this sample that are currently at or near Roche lobe overflow, three of which are currently of planetary mass, and three of which are BD mass. These systems will all be the subject of further scrutiny. In general, for a 1-10 M_{Jup} planet to cause a $\sim 1 M_{\odot}$ primary to overflow its Roche lobe, the radius of the primary would have to exceed $\sim 70 - 80\%$ of the separation between the two bodies. This would not be an unreasonable expectation for a companion orbiting within 1 AU, as solar-mass stars can achieve radii approaching 1 AU at the tip of the RGB. Therefore, this mechanism may be a way to explain the relatively large number of BD companion candidates orbiting the evolved stars in this sample. Overall, this catalog's large number of systems with short-period BD companion candidates challenges the notion of the BD desert as we know it, and certainly warrants further investigation.

3.1.2 Eccentricity Distribution

In Figure 3.1, we also see the distribution of orbital eccentricities. As expected, the smallest-separation ($a < 0.1$ AU) stellar-mass companions all have circular orbits. The circularization cutoff period increases with the age of the system with 5-10 Gyr systems having cutoff periods of 12-20 days (Mathieu et al. 2004). All of the binary companions in this catalog with $a < 0.1$ AU have $P < 20$ days. Therefore, the distribution of eccentricities for the binary systems in this sample, with circular orbits

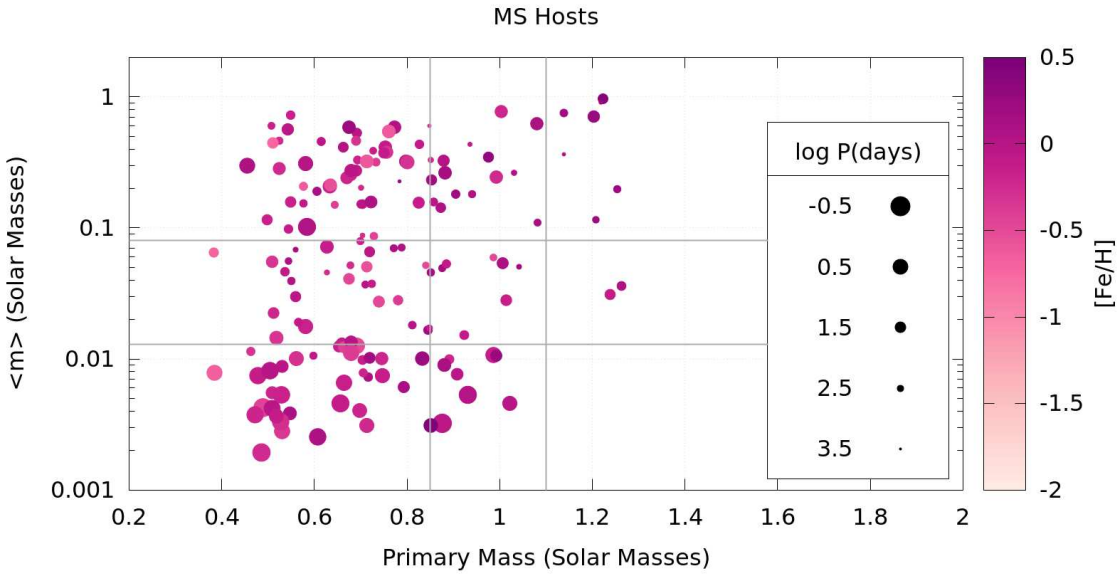

Fig. 3.3.— Modification of Figure 3 from Guillot et al. (2014), with $M_\star$ on the abscissa and maximum-likelihood companion-mass ($\langle m \rangle$) on the ordinate. Color represents the host stars' metallicity, and point size represents the period of the companion in log days. Larger points here indicate companions that are more likely to be undergoing tidal interaction with their host star. This plot shows stars in the gold sample selected as MS stars. The vertical lines mark nominal G dwarfs ($0.85 < M_\star/M_\odot < 1.1$), and the horizontal lines mark the BD mass regime ($0.013 < \langle m \rangle/M_\odot < 0.08$).

at small separation, and eccentric orbits a large separations is not unexpected. The closest ($a < 0.01$ AU) planetary-mass companions appear to have also circularized, as expected, but a surprising result is the relatively large fraction of eccentric orbits for relatively close-in planetary-mass candidate companions. For the RG and RC hosts, on interpretation of these eccentricities is ongoing tidally-induced migration (see §3.2.1 for further discussion of this). However, the majority of the small-separation planetary and BD candidate companions orbit dwarf and SG stars. For these systems, their higher eccentricities may be further evidence for the mechanism suggested by Tsang et al. (2014) whereby stellar illumination heating a gap cleared by a forming planet may excite the eccentricity of the planet in the gap.

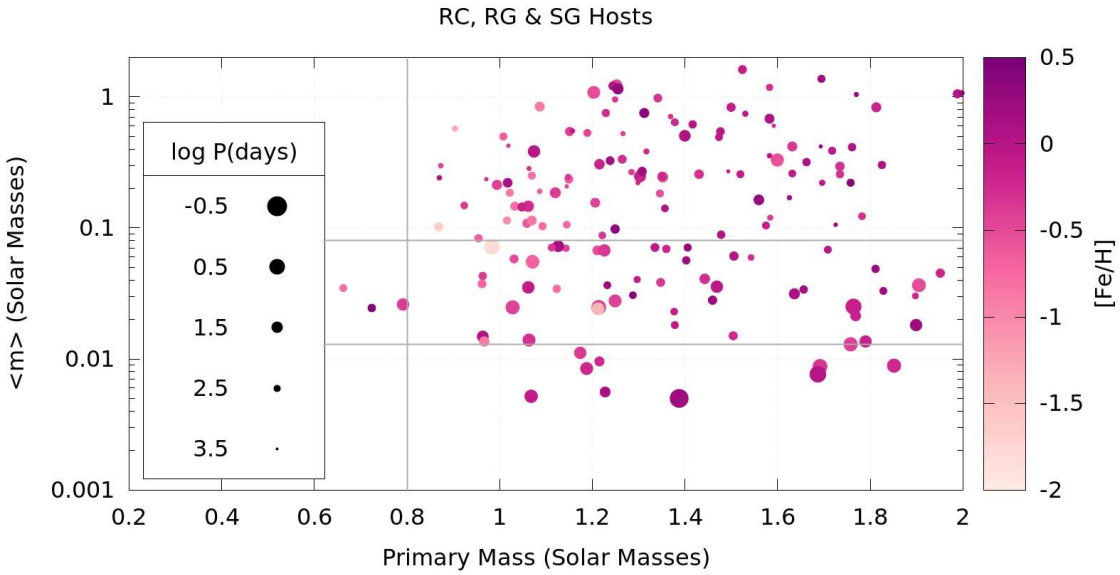

Fig. 3.4.— Same as Figure 3.3, but with the remaining stars in the gold sample with $M_\star < 2M_\odot$. The horizontal lines again mark the BD mass regime, and the vertical line marks $M_\star = 0.8M_\odot$. It would be a reasonable expectation that a giant star above this mass evolved from a star earlier than a G dwarf since solar-like stars loose about one third of their mass on the RGB.

3.1.3 High Mass Ratio Systems

Of this catalog's candidate companion systems, there are 50 systems with a mass ratio $\langle q \rangle = \langle m \rangle / M_\star \geq 0.5$ (see Figure 3.2). One would expect that these systems would manifest themselves as SB2s, but these systems show no strong indication of such behavior in their APOGEE spectra. Of these, 24 are RG stars, which would explain their lack of SB2 behavior, as their companion is likely still on the main sequence, and thus the flux ratio would be too large. However, this still leaves 26 MS and SG hosts, of which one explanation is that they host massive compact objects, such as stellar remnants. These seven companions have $0.3M_\odot < \langle m \rangle < 1.2M_\odot$, which would indicate these systems might host white dwarf companions, eight of which may be low-mass ($\langle m \rangle < 0.45M_\odot$) He-core white dwarfs (Liebert et al. 2005). Furthermore,

two of the systems with a RG host have $\langle q \rangle > 1$, indicating the companion has already completed its evolution, and the recovered $\langle m \rangle$ of the companions (2.8 and $1.6 M_{\odot}$) indicates they may be neutron stars.

3.2 Host Star Distribution

Solar type stars (i.e., G dwarfs) have been the primary focus of exoplanet and stellar multiplicity studies. Out of the 382 stars in this sample, only 36 are solar-type (MS with 5000K $< T_{\rm eff} <$ 6000K) stars. Figure 3.5 reveals that, in addition to the solar-type stars, this sample contains cool dwarfs, subgiant and giant stars, which allows us to probe many different stellar types and stages of stellar evolution. Figure 3.5 also presents distributions of the stellar parameters of the host stars in this sample.

3.2.1 The Fate of Companions: Exploring Evolved Host Stars

Tidal dissipation is thought to play an important role in the destruction of planetary systems as a star evolves off the main sequence and expands (Penev et al. 2012). This sample contains 225 $a < 3$ AU candidate companions to evolved stars, indicating either many initial small separation companions survive engulfment or farther-orbiting planets undergo increasing tidal migration as its host ascends the giant branch, bringing the companion closer to its host star. The nine candidate planetary-mass ($\langle m \rangle < 0.013 M_{\odot}$) companions orbiting giant stars in this sample would be a 20% increase in the number of currently known giant stars hosting a planet ($\sim$ 50 according to the tabulation by Jones et al. 2014a). As Jones et al. (2014a) mentions, there is a small separation cut-off for RG hosts. The current record-holder for smallest separation of an RV-detected planet RG host is HIP 67851b with $a = 0.539$ AU (Jones et al. 2014b). The shortest period planet orbiting a giant star, Kepler 91b,

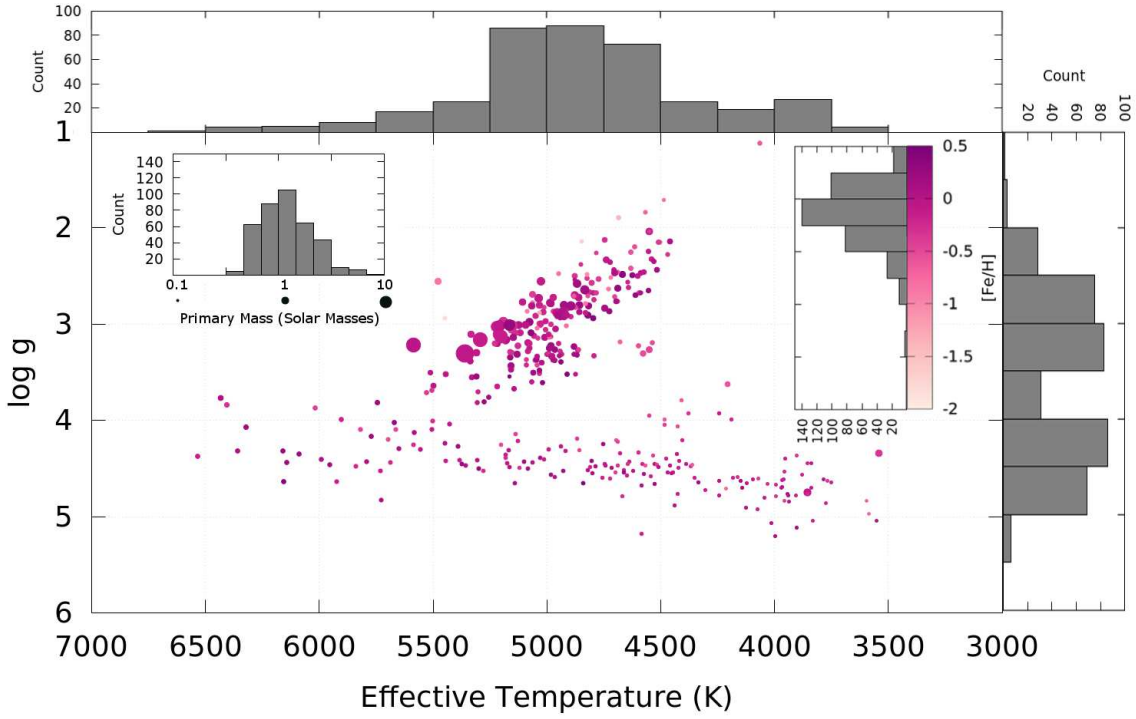

Fig. 3.5.— A spectroscopic HR diagram of the companion candidate hosting stars, with the host stars' $T_{\rm eff}$ and $\log g$ as the abscissa and ordinate. The points are color-coded by host star metallicity ([Fe/H]), and point size indicates the primary mass in Solar masses. The stars along the bottom of the figure are the dwarf stars, and stars along the line connecting $(T_{\rm eff}, \log g)$ = (5500 K, 3.5) and (4000 K,1) are the giants. Histograms of the effective temperature ($T_{\rm eff}$, top panel), surface gravity ($\log g$, right panel), metallicity ([Fe/H], inset with color bar), and primary mass (inset with size legend) of the host stars in this gold sample are also shown.

is on a 6-day orbit (Lillo-Box et al. 2014). Most of the candidate planets orbiting giants lie between these two systems, with a few candidates closer than Kepler 91b.

Of the evolved stars in this sample, 23 are verified Red Clump (RC) stars (Bovy et al. 2014). RC stars are metal-rich stars which have passed through the tip of the red giant branch (RGB) and have contracted due to the ignition of core helium burning. It is expected that stars like the Sun may reach radii up to 1 AU when they reach the tip of the RGB. Therefore, the presence of companion candidates orbiting RC stars at $a < 1\,$AU in this catalog (see Figure 3.6) is a surprising discovery. To investigate

this further we compared the RC stars to RGs in this sample, but we consider only RGs with [Fe/H] > -0.42 ([Fe/H] of the most metal-poor RC in this sample) and $2.4 \leq \log g \leq 3.3$ (the $\log g$ range of the RC stars) to eliminate possible effects from RV sensitivity issues. This also allows us to compare stars approximately half way up the giant branch to stars that have already passed through the tip of the RGB, and have achieved their largest extent. These 92 RG stars have 62 stellar-mass, 25 BD-mass, and 5 planet-mass companion candidates compared to 18, 5 and 0 for the 23 RC giants.

A cursory look at these numbers (and Figure 3.6) shows a lack of smaller companions for Red clump stars, as well as a companion candidates found at smaller separations for the 92 RG stars when compared to RC stars (0.07 AU vs. 0.2 AU at the low-mass end). It is also interesting to note that no companion candidates have circular orbits among RC hosts (smallest $e = 0.284$). This all points to the role of the tidal migration and destruction of companions, particularly planetary-mass companions. However, any tidally induced migration of companions will be much weaker than when the star was in the RGB phase. Therefore any companions with $a < 1$ AU around an RC star likely would have to have survived inside the star's envelope during its RGB phase. Most of the RC hosts with $a < 1$ AU candidate companions are likely post-common envelope systems, and thus may have experienced drag-induced migration to bring them to their current orbit. These systems certainly warrant deeper investigation.

3.2.2 Metal-Poor Companion Hosts

According to the compilation of exoplanets.org (Han et al. 2014), of the confirmed planet-hosting stars with metallicity measurements, only 15 have [Fe/H] < -0.5. this

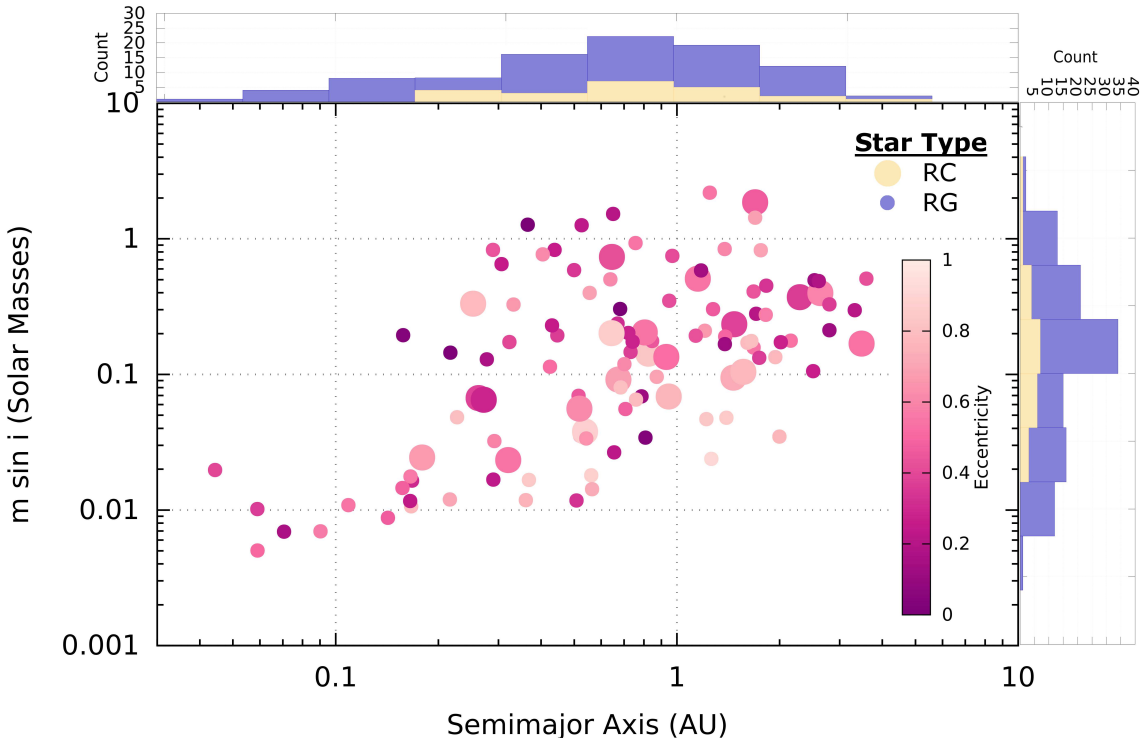

Fig. 3.6.— Orbital distribution of companion candidates to RC stars (large points) and RG stars with similar stellar parameters as this sample's RC stars (small points). Minimum orbital semi-major axis in AU is on the abscissa and minimum companion mass in $M_{\odot}$ is on the ordinate. Color again represents the orbital eccentricity of the companion. The panels above and to the right of main plot show the msini and semi-major axis distribution for the RG comparison sample (purple histogram) and RC (gold histogram) hosts.

sample has 41 stars with [Fe/H]< -0.5, and of these two host candidate planetary-mass companions, and 14 host candidate BD companions. The most metal-poor stars in this sample approach [Fe/H] $= -2$. While there are no candidate planets among the most metal-poor ([Fe/H] < -1) hosts (5 stars), there are two companions in the BD mass regime. The smaller fraction of the lowest-mass companions detected among the most metal-poor stars in this sample is not surprising as the RV uncertainties are higher for metal-poor stars as described in equation 2.1. Also, it is not too surprising to find metal-poor stars hosting binary companions, given the Carney et al. (2003)

result. However, finding a population of metal-poor stars potentially hosting BD companions is surprising in the context of the core accretion model of companion formation, and may suggest an alternate formation mechanism for these companions.

3.3 Galactic Distribution of Candidate Hosts

Most surveys for stellar and substellar companions have focused on stars in the solar neighborhood, especially with the recent interest in M dwarf planet hosts. In contrast, only three of the sources in this catalog are within 100 pc of the Sun, where the vast majority of known planets with distance measurements have been found. In a Galactic context, this sample is truly complementary to previous studies. The current most-distant known planet host is the microlensing source OGLE-2005-BLG-390L at 6.59 kpc (Beaulieu et al. 2006). The most-distant planetary-mass ($\langle m \rangle = 7.26 M_{Jup}$) candidate companion in this catalog orbits the slightly metal-poor ([Fe/H]$= -0.34$), RG ($\log g = 2.5$) star 2M05445028+2847562, which lies at a comparable distance of 6.13 kpc.

Furthmore, this sample has 36 companion candidates farther than this distance. Of these, 12 are BD-mass companions around stars reaching to a distance of 15.7 kpc. Figures 3.7 and 3.8 demonstrate the Galactic reach of this catalog's companion candidate hosts. A large majority of this sample (327 stars) resides in the Galactic Thin Disk ($|Z| < 1$ kpc[1], but these disk stars reach from inner disk ($R \sim 2$ kpc) to the outer disk ($R \sim 15$ kpc). From this preliminary analysis, it is safe to say that companions of all types are ubiquitous across the thin disk. As we move from the

[1]Distinguishing between Thin and Thick Disk stars would require a full analysis of their chemistry and kinematics. Here we simply present a census of companion as a function of height above the midplane, and use these criteria: Thin Disk = $|Z| < 1$ kpc, Thick Disk = $1\,\mathrm{kpc} \leq |Z| < 5\,\mathrm{kpc}$, Halo = $|Z| \geq 5$ kpc.

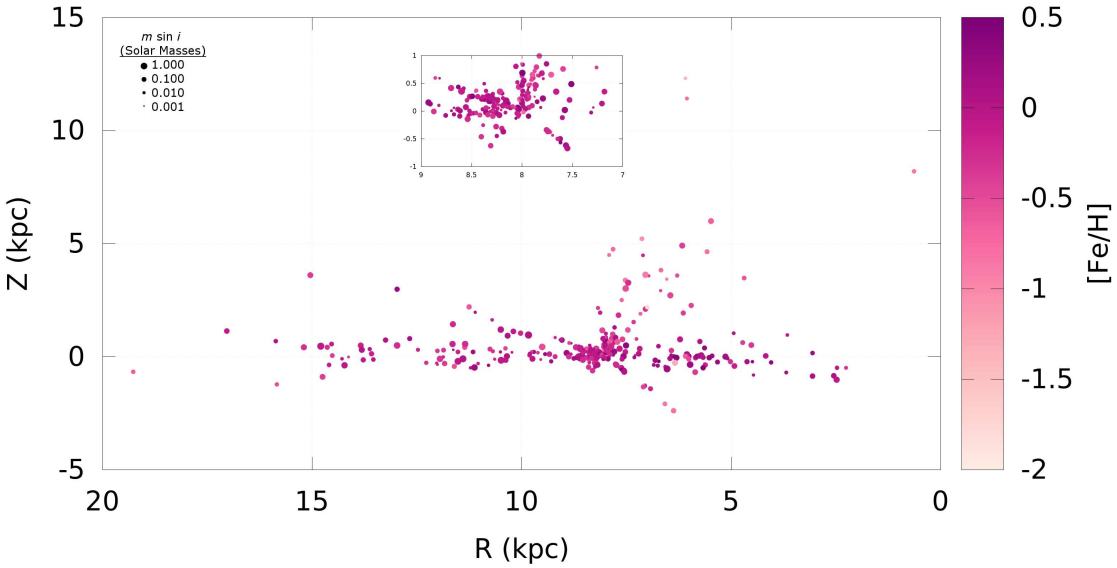

Fig. 3.7.— The Galactic distribution of companion candidate hosts in the DR12 catalog in Galactocentric R and Z, where R is the radial distance from the Galactic Center, and Z is the height above the Galactic midplane. The color of the points indicates the metallicity ([Fe/H]) of host star, and the point size indicates $m \sin i$ of the companion candidate orbiting the star. The inset panel shows a detailed view of the solar neighborhood, which is indicated by the black box in the main plot ($7\,\mathrm{kpc} < R < 9\,\mathrm{kpc}$, $|Z| < 1\,\mathrm{kpc}$).

thin disk to the halo, the proportion of higher-mass companions increases. This trend is likely due to the combination of the sensitivity bias that low-mass companions are less likely to be detected around more metal-poor stars (see Equation 2.1), and the planet-metallicity correlation.

3.4 Catalog Information

For each star in the 382-star gold sample, the following data are available:

1. APOGEE targeting information, 2MASS photometry, proper motions, and reduction flags.

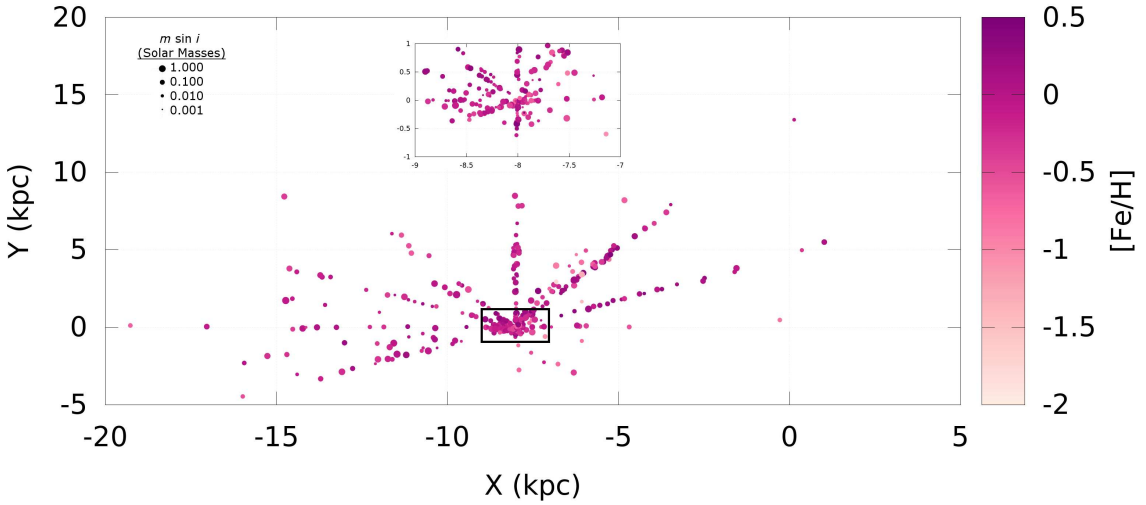

Fig. 3.8.— The Galactic distribution of companion candidate hosts in the DR12 catalog in Galactocentric X and Y rectilinear coordinates, where $(X, Y) = (0, 0)$ and $(-8, 0)$ kpc are the locations of the Galactic Center and the Sun respectively, and $Y > 0$ is in the direction of the Sun's orbit. The color and size of the points indicate the same data as they do in the top panel. Again, the inset panel shows a detailed view of the solar neighborhood, which is indicated by the black box in the main plot ($7\,\mathrm{kpc} < X < 9\,\mathrm{kpc}$, $|Y| < 1\,\mathrm{kpc}$).

2. Adopted APOGEE stellar parameters ($T_{\rm eff}$, $\log g$, [Fe/H]), and estimates of each primary star's mass, radius, and distance, with flags indicating the source/quality of the stellar parameters and mass/radius/distance estimates.

3. Heliocentric RV measurements for each star derived using best-fit ASPCAP synthetic spectra as RV templates.

4. The best-fit orbital and physical parameters of each system's candidate companion.

3.4.1 Data Access

These data are compiled into a `FITS` table, whose content is described in Table 4 of Troup et al. (2016). The catalog is also available as a Filtergraph portal here:

https://filtergraph.com/apOrbitPub. The Filtergraph portal also contains links to webpages containing plots of the RV curves for these systems. Additional data for each star, including spectra and additional photometry, are available publicly via SDSS DR12 (Alam et al. 2015). See http://www.sdss.org/dr12/ for instructions on the access and use of APOGEE DR12 data.

3.4.2 Caveats

Here we present some caveats regarding the quality of the data in this catalog:

- All caveats that apply to all APOGEE data (Holtzman et al. 2015) also apply to this catalog.
- Many stars with the longest baselines were observed during APOGEE commissioning, during which the instrument did not employ dithering. However, these stars were reobserved at the end of the survey with the standard instrument configuration, and RVs derived from commissioning data have been shown to be of similar quality to main-survey RVs.
- The stellar parameters derived by ASPCAP for dwarf stars are uncalibrated, but good enough to establish estimates of the star's primary mass, and sufficiently accurate to distinguish between dwarfs and giants.
- The RV errors output by the APOGEE reduction pipeline may be slightly underestimated. We refer the reader to §10.3 of Nidever et al. (2015) where RV uncertainties are discussed more fully.
- The distances presented here are from a preliminary catalog, and will likely undergo future refinement.

- The most common source of errors in the orbital parameters is the fitter choosing the wrong harmonic for the period. Therefore, the periods presented here may be an integer number (2 or 3) or an integer fraction (1/2 or 1/3) times the true period for the system. The fitter also had a tendency to inflate the eccentricities of the simulated systems, so the eccentricities, and thus the values of K and $m \sin i$ presented here are likely to be slightly larger than their true values.

- The values for argument and time of periastron (T_P and ω) become unconstrained at low eccentricities, and are poorly reproduced by this catalog. We release them so that our model curves can be reproduced, but should be taken with a grain of salt.

Finally we stress that the systems presented here are *candidates*, and that the orbital parameters presented here may only be characteristic of the true values of the system. In particular, the low-mass and low-visit candidates are the most in need of additional observation. We have a significant ongoing observational program to individually investigate the best planetary mass and BD systems in this catalog that includes high-resolution spectroscopy, diffraction-limited imaging, and photometric variability monitoring. These efforts are described further in §6.1.

3.5 Conclusions

Through analysis of multiple epochs of APOGEE spectroscopic data, we have identified 382 stars that have strong candidates for stellar and substellar companions, of which 376 had no previous reports of small separation companions. From an initial analysis of this sample we have found:

1. Two distinct regimes of companions in $m \sin i$ - a space exist that are likely the

result of distinct formation paths for stellar-mass and planetary-mass companions, with the gap between the two regimes being a manifestation of the BD desert. However, we find a smaller and "wetter" BD desert with the BD desert only manifesting itself for orbital separations of $a < 0.1 - 0.2$ AU in this sample of candidate companions, much smaller than the 3 AU proposed in previous studies. We proposed a few potential explanations of this result: (a) Lower mass MS candidate hosts host a higher relative number of BD-mass candidates than their higher-mass MS counterparts, lending evidence to the Duchêne & Kraus (2013) interpretation that the BD desert may be a special case of a more general dearth of extreme mass ratio binary systems. (b) A majority of the candidate BD companions in this catalog orbit evolved F dwarfs, supplying further evidence to the "F dwarf oasis" hypothesis proposed for small separation BD companions by Guillot et al. (2014). (c) The possibility of planetary-mass candidates orbiting within ~ 1 AU initiating Roche lobe overflow of their hosts as it ascends the giant branch, allowing planetary-mass companions to grow to BD mass.

2. A significant number of small-separation eccentric systems which may be evidence for ongoing tidal migration among the giant hosts and the eccentricity-pumping mechanism proposed by Tsang et al. (2014) for the dwarf hosts.

3. A set high mass ratio candidate systems ($\langle q \rangle > 0.5$), of which 28 show indications of containing a stellar remnant, including two neutron stars, and eight potential He-core white dwarfs.

4. 225 candidate companions orbiting evolved (RC, RG, and SG) stars. This includes nine new planetary-mass candidate companions around giant stars,

which, if confirmed, would be a $> 20\%$ increase from the previously known number given by Jones et al. (2014a), as well as 3 planetary-mass candidates orbiting subgiant stars. Among the RC stars, 15 host companion candidates orbiting within 1 AU, the maximum expected extent of a RGB star evolved from a Sun-like star, indicating these systems are likely post-common envelope systems.

5. A population of 41 metal-poor ([Fe/H] < -0.5) candidate companion hosting stars, of which 2 host planetary-mass candidates, and 14 host BD candidates. These systems challenge the planet-metallicity correlation, and thus the core accretion paradigm of companion formation. It is possible the formation pathway for these companions may closer mimic that of binary systems or a gravitation instability scenario.

6. To first order, companions of all kinds are prevalent throughout the disk ($2\,\mathrm{kpc} < R < 15\,\mathrm{kpc}$, $-2\,\mathrm{kpc} < Z < 2\,\mathrm{kpc}$), with planetary-mass companions found out to distances of ~ 6 kpc, and BD-mass companions to distances of ~ 16 kpc.

A campaign is underway to confirm and further characterize the nature of the candidate companion systems reported here. This effort will be augmented with SDSS-IV APOGEE-2 observations. Between APOGEE-1 targets obtaining additional visits and new APOGEE-2 targets obtaining a large number of visits, we expect APOGEE's sample of candidate companions to at least triple by the end of SDSS-IV.

Chapter 4

APOGEE Reduction Software Upgrades for DR13 and DR14

Several improvements to the APOGEE pipelines were incorporated for SDSS-IV DR13 and DR14 that had a direct impact our ability to measure the orbital and physical parameters of systems observed by both APOGEE-2 and APOGEE-1[1]. In this chapter, I present two particular areas of the ASPCAP and APOGEE RV pipelines to which I made major contributions, and which will be published in upcoming APOGEE technical papers. These upgrades improve the ability to exploit APOGEE for the derivations of orbits for stars in exciting new Galactic environments and stellar populations never before probed with long-term RV monitoring.

[1]SDSS data releases include all new data taken as well as data from previously released rereduced using the most up-to-date pipelines.

4.1 ASPCAP Automated Rotational Velocities

4.1.1 Motivation

One of the more glaring shortcomings of the DR12 analysis was the assumption of a fixed macroturbulent velocity with no rotational broadening when building the grids used for ASPCAP. While rotational broadening and pressure ($\log g$) broadening produce slightly different line profiles that can be easily differentiated by a fitting program, an automated fitting routine with no option for rotational broadening would treat the rotational broadening in a star's spectrum as pressure broadening, thus leading to an overestimate of the star's $\log g$ (see Figure 4.1).

The DR12 grids were satisfactory in the analysis of giants, which represents $\sim$ 75% of the overall APOGEE-1 sample, because giant stars with apparent rotational broadening in their spectra are extraordinarily rare. However, as discussed in the previous chapter, dwarfs represent $\sim$ 40% of the DR12 gold sample of candidate companion hosts, and many goal science programs for APOGEE-2, such as the Kepler KOI program and the young cluster program, require reliable parameters for dwarfs, including young rapidly-rotating stars. In addition, acquiring rotational velocities will allow estimates of the ages of the dwarf star hosts in future catalogs via the age-rotation correlation. Finally, because the refined velocities we use in orbit fitting depend on the selected ASPCAP template spectrum for the star, this upgrade will also improve our ability to correctly derive RVs and recover orbital parameters for systems with dwarf hosts.

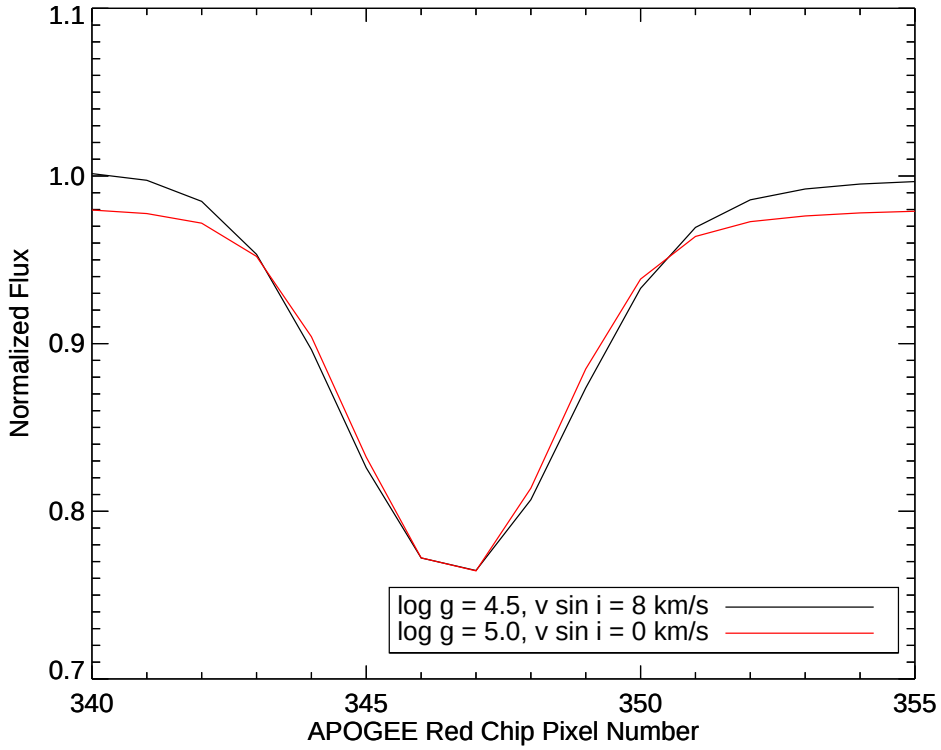

Fig. 4.1.— Example ($T_{\rm eff}$ = 3500K, $[Fe/H]$ = 0.5) synthetic spectra from one of the Kurucz spectral grids used by ASPCAP demonstrating the degeneracy that can arise in line profile shape between pressure ($\log g$) and rotational broadening. The black line shows a model spectrum with the above parameters and $\log g = 4.5$ and $v \sin i = 0$, while the red line shows $\log g = 5$ and $v \sin i = 8$ km s^{-1}.

4.1.2 Implementation

Implementation of the automated rotation fitting required the generation of new libraries of synthetic spectra that included a dimension varying $v \sin i$, in addition to the dimensions varying T_{eff}, $\log g$, v_{micro}, overall metallicity, and select global abundances (α, C, N). The APOGEE `speclib` package, which generates these libraries using provided linelists and model atmospheres (e.g., Kurucz, MOOG), required some modification to allow for the additional dimension, as did the main ASPCAP fitting routines. The rotation dimension was built with logarithmic grid steps from $v \sin i = 1.5$ km s^{-1}, below which rotational broadening is indistinguishable from in-

strumental broadening, to 96 km s^{-1}, the largest rotational velocity expected for a typical $T_{\rm eff}$ = 8000 K dwarf, in $\log v \sin i = 0.301$ increments.

However, running a seven-dimensional[2] grid on the entire APOGEE sample proved to be unwieldy, with each additional search dimension roughly doubling the run time of ASPCAP. This led to the decision to have separate grids for dwarfs and giants so the full sample still employed a six-dimensional search. The giant grids were much the same as the DR12 grids, but instead of a fixed v_{macro} for the entire sample, we employed a relation that set v_{macro} as a function of surface gravity and metallicity. The dwarf grids allow for variable $v \sin i$ and v_{micro}, but since the vast majority of dwarfs are expected to have roughly solar chemical abundances, the global [C/M], and [N/M] are fixed to 0. In addition, M dwarf and giant grids was added, which extended to $T_{\rm eff}$ as low as 2500 K and included spherical geometry, for better treatment of the coolest, most extended giants, as well as pre-main sequence stars and M dwarfs. Furthermore, to mitigate the issues of varying LSF from fiber-to-fiber and across the chip, each giant and dwarf grid had five versions, each convolved with a different LSF representing an average of 60 contiguous fibers. The best LSF grid was chosen based on the median fiber number on which the star was observed. Table 4.1 summarizes the parameter space covered by each grid. In cases of grid overlap, the grid solution with the lowest χ^2 was chosen. Full details will be outlined in the forthcoming APOGEE DR13 data paper (Holtzman, et. al, in prep.).

4.1.3 Performance and Preliminary Results

Our first assessment of the performance of the rotation grid was to compare the ASPCAP-derived rotational velocities with previously published values. The Pleiades

[2]Eight-dimensional if v_{micro} is treated as a free parameter.

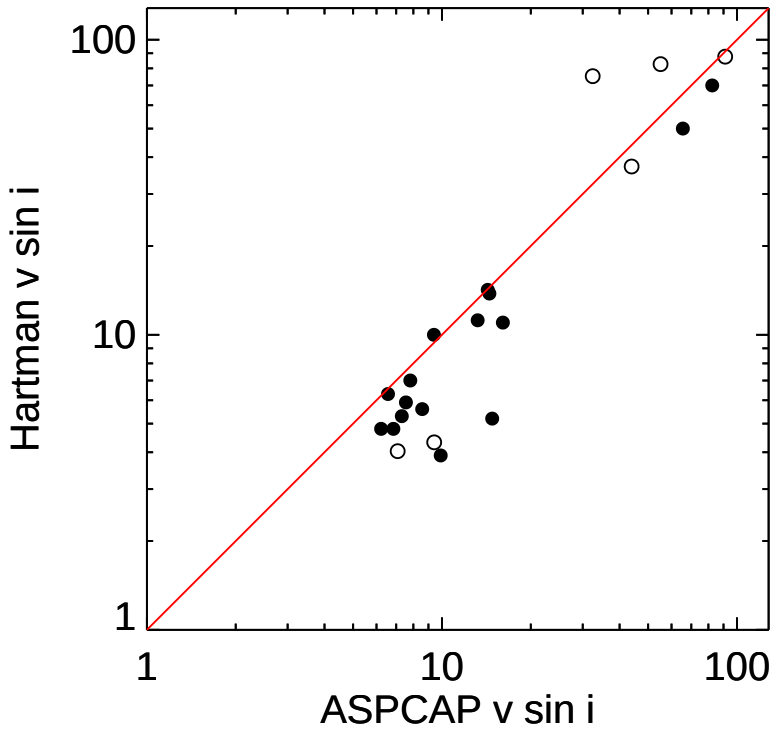

Fig. 4.2.— Comparison of the $v \sin i$ values (in km s^{-1}) from Hartman et al. (2010) to those derived by ASPCAP in DR13 for stars in the Pleiades. The red line is a one-to-one ratio, and open circles indicate stars for which Hartman et al. did not report $v \sin i$ values, only rotational periods, so we derived values for v_{rot}, and thus upper limits on $v \sin i$ from these values.[3]

members observed by APOGEE were a perfect comparison sample because (1) the Pleiades is a young population containing many dwarfs with a wide range of rotational velocites, and (2) the Pleiades are nearby ($d \sim 140$ pc) and therefore bright ($H < 12$) so they were highly likely to have reliable literature $v \sin i$ measurements. In Figure 4.2, we compare ASPCAP rotational velocities from DR13 and those reported by Hartman et al. (2010); a general agreement is seen.

Next we ascertained if the addition of rotational velocity information actually had the desired effect on the stellar parameters, in particular removing the overestimate in

[3] $v_{rot} = \max(v \sin i) = 2\pi R_\star / P_{rot}$, where $R_\star$ is the radius of the star as reported by Hartman et al.

$\log g$. In Figure 4.3, we see no overall change in $\log g$ for stars with $v \sin i < 6$ km s^{-1}, which was the fixed macroturbulent velocity broadening applied globally to all grid spectra in ASPCAP for DR12. For $v \sin i > 6$, the general trend is that DR13 values for $\log g$ are smaller than those for DR12 and the effect is more dramatic at higher values of $v \sin i$, as expected. Some major exceptions to the general trend include:

- The coolest dwarfs (the blue points in the top panel of Fig. 4.3) show a significant scatter in $\Delta \log g$. These changes are more likely due to the inclusion of an M grid in DR13, which extends $T_{\rm eff}$ lower limit from 3500K to 2500K.

- Potential rapidly rotating giants (the blue points in the bottom panel of Fig. 4.3) have significantly larger $\log g$ deviations due to a starker difference between their pressure-broadened and rotationally-broadened spectra than for dwarfs.

- Hot stars (orange/red points in the top panel of Fig. 4.3) experience smaller changes to their $\log g$ values, even for high values of $v \sin i$. These stars have spectra are almost exclusively H lines which are already naturally very broad, so the inclusion of rotational broadening does not have as dramatic of an effect on their derived $\log g$ values.

As a final test we compared the ASPCAP results of clusters with large populations of dwarfs observed by APOGEE, namely M67 and the Pleiades, with appropriate PARSEC (Bressan et al. 2012) isochrones (see Figure 4.4). As expected, the giant branch for M67 largely remains unchanged, and macroturbulent velocity (which is represented by the same grid dimension as rotational velocity in the giant grids) increases up the giant branch to a maximum of ~ 4 km s^{-1} at $\log g = 2$, as expected. [4] The dwarfs in M67 lie much closer to the theoretical isochrone, and rotate at

[4] Based on the relation $v_{macro} = 10^{0.741 - 0.0998 \log g - 0.225[M/H]}$ adopted for DR13.

$v \sin i \sim 6$ km s^{-1}, a reasonable rotational velocity for a 5 Gyr old late F ($T_{\rm eff} \sim 6000$ K) dwarf. We note that this $v \sin i$ value is perhaps slightly too high, but recent aging using gyrochronology dates M67 at 4 Gyr (Barnes et al. 2016), a slightly younger age than indicated by our isochrone fitting. The most problematical feature of the DR12 data for the Pleiades is the large number of stars at the DR12 grid edges ($T_{eff} = 3500$K and $\log g = 5$). This issue no longer manifests itself in the DR13 data through the combined effects of the inclusion of rotation and the addition of the M grid, and the vast majority of the members lie within 0.25 dex of the isochrone.

It is clear that the most rapidly-rotating stars (red and orange points representing stars with $v \sin i > 50$ km s^{-1} in Fig. 4.4) are still problematic. With many lines blended, and weaker lines indistinguishable from the continuum, automated analysis of rapidly rotating stars results in degenerate solutions, and requires more careful, manual analysis. Furthermore, astrophysical events, such as the engulfment of a companion, can lead to anomalously high rotation rates. In Table 4.2, we present a list of such anomalously rapid ($v \sin i > 20$ km s^{-1}) along with moderately rapid (10 km s^{-1} $< v \sin i < 20$ km s^{-1}) rotators in M67. The anomalously rapid rotators contain several blue stragglers and close binaries where a binary companion spun up the star through its engulfment or close orbit. There are also a number of SB2s identified by Chojnowski et al. (2015) from APOGEE spectra, which are not treated well by the APOGEE visit combination routines, nor, by extension, ASPCAP, which assumes single-component spectra. This typically leads to poor, if not nonsense, parameter estimates, including false signals of rapid rotation due to the primary's and secondary's lines being blended together during visit combination. Roughly half of the moderately rapid rotators also include SB2s and older[5] blue stragglers. However, the remaining half have no indications in previous literature as to why they have

[5] i.e., stars that have had more time to spin down after engulfing a companion.

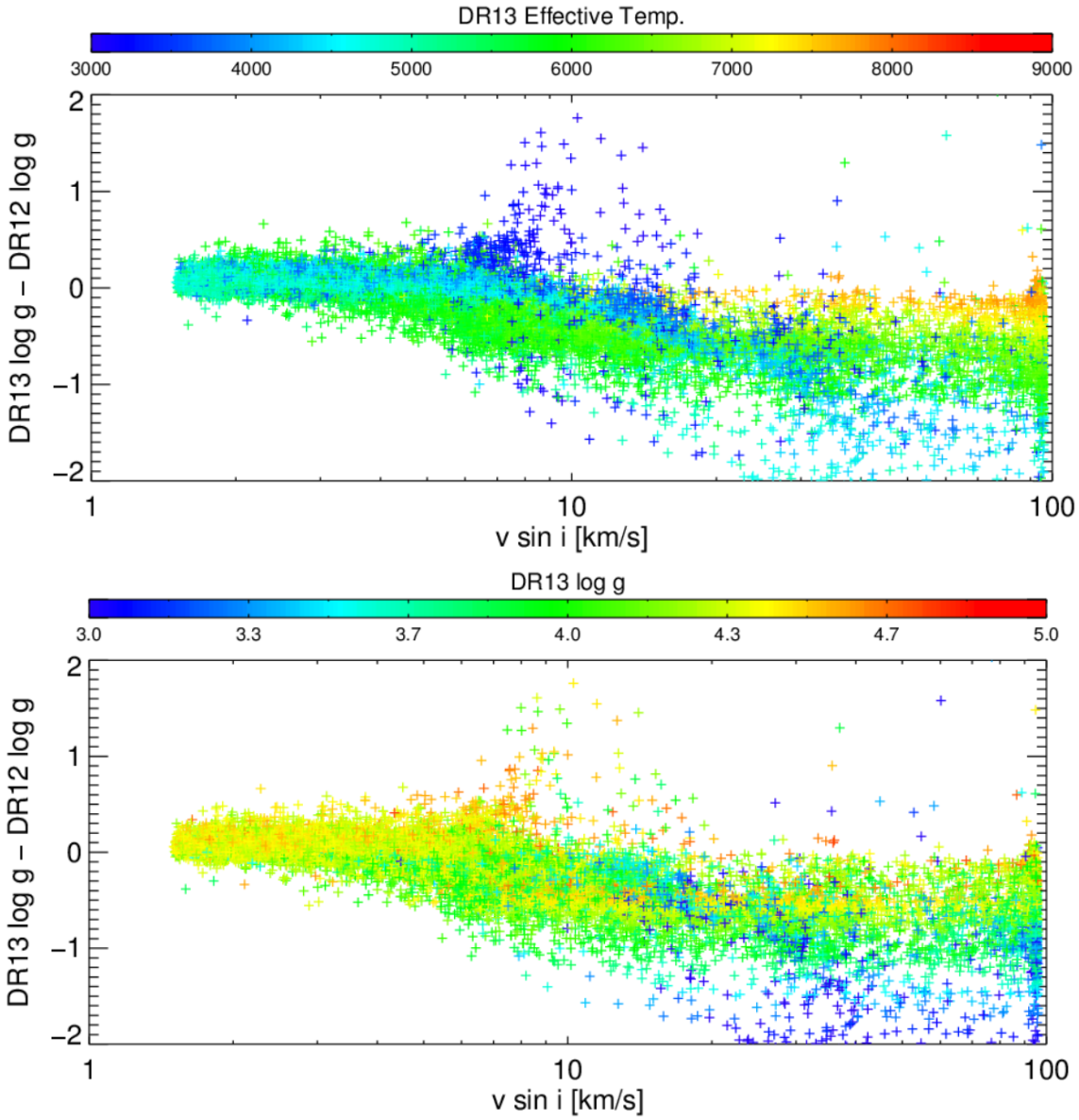

Fig. 4.3.— Difference between $\log g$ values derived in DR13 with rotation and DR12 without as a function of DR13 $v \sin i$, and color coded by DR13 $T_{\rm eff}$ (top) and $\log g$ (bottom). For the analysis presented in this plot, we compare the raw FERRE output because the calibration relations for stellar parameters changed from DR12 to DR13, and DR12 did not provide calibrated stellar parameters for dwarfs (Holtzman et al. 2015). Furthermore, any star with the ASPCAP `STAR_WARN` flag set for DR13 was excluded.

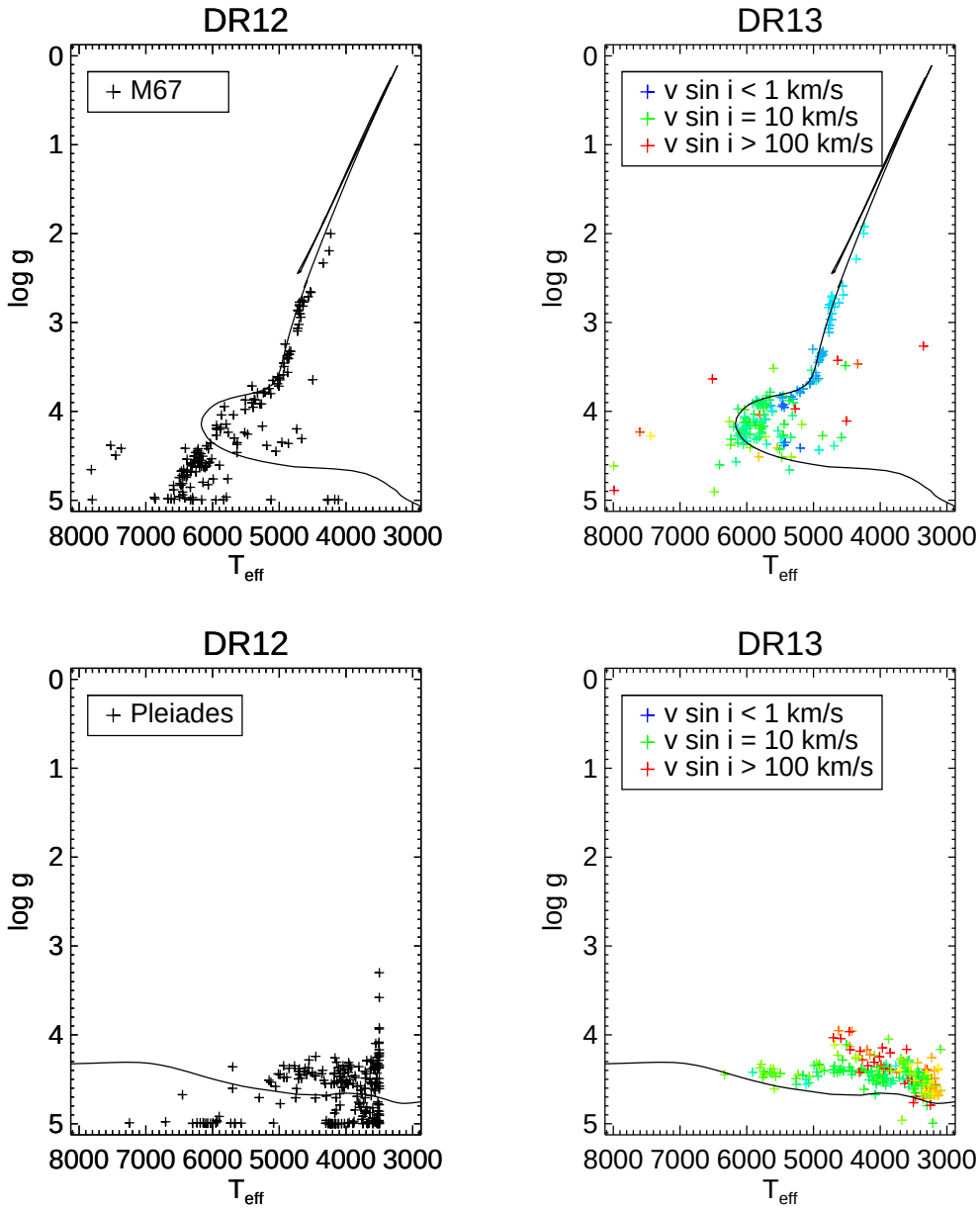

Fig. 4.4.— Spectroscopic HR diagram of M67 (top) and Pleiades (bottom) cluster members constructed using APOGEE DR12 (left) and DR13 (right) data. The DR13 data are color-coded by $v \sin i$. On each panel solar metallicity PARSEC isochrones are over-plotted, with a 5 Gyr isochrone used for the M67 plots and a 100 Myr isochrone used for the Pleiades. Note that for stars on the giant branch ($\log g < 3.8$), $v \sin i$ represents macroturbulent velocity rather than rotational.

higher rotation rates than expected for a cluster the age of M67. These rapi rotators are good candidates to search for signs of rocky planet engulfment, such as lithium enhancement in the atmosphere of the star (e.g., Carlberg et al. 2012).

4.2 Improved RV Extraction and Visit Combination for Low S/N Sources

4.2.1 Motivation

As can be seen in Figure 4.5, APOGEE-1 survey targets went as faint as $H = 13.8$, which were expected to achieve SNR ~ 20 per one-hour visit (Zasowski et al. 2013). However, the APOGEE-2 survey targeted a few thousand objects fainter than this, pushing as deep as $H = 15.5$. With such faint targets, the standard APOGEE observing scheme ($\sim$ 1 hour visits) results in visit SNR in the single digits for these targets.[6] This becomes an issue for RV determination and, as a consequence, visit combination. The DR12/DR13 version of RV determination code relied on using the observed visit-combined spectra of the star for cross-correlation template, which, in the case of low S/N, often was not combined well, and thus was not representative of the true spectrum of the star, or had significant noise artifacts that influenced the cross-correlation. Therefore, there was a strong motivation to investigate alternative methods for RV extraction and visit combination for these faint targets. Not only is getting RVs correct important for visit combination, but it is crucial for the RV companion search, particularly because these faint APOGEE2 targets include interesting new environments (see §1.2.2 for background) to probe for binarity, such as in Milky

[6]This issue was partially mitigated by employing double-length exposures for plates targeting faint stars.

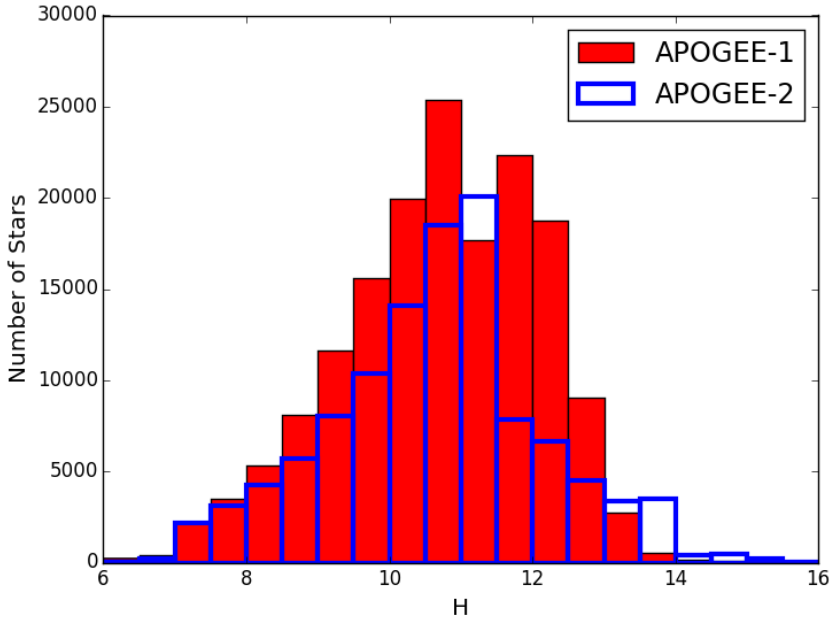

Fig. 4.5.— A comparison of the APOGEE-1 target H magnitude distribution (blue open histogram) to the distribution of the first year of APOGEE-2 targets (red filled histogram).

Way satellite dwarf spheriodals (dSphs) and the Magellanic Clouds (MCs).

4.2.2 New Features Implemented

With these issues in mind, I was tasked with analyzing the current RV determination and visit combination routines to ascertain ways the code could be improved to mitigate some of the concerns raised above. Here I describe some of the new features I implemented to improve the performance of the pipeline for low S/N spectra.

Signal-to-Noise Visit Rejection

While the visit spectra are weighted by S/N when combined, reporting RVs from spectra with abnormally low S/N resulted in erroneous signals of RV variability.

Furthermore, visits with abnormally low S/N would not significantly contribute to the signal of the final combined spectrum in the weighting scheme, so determining RVs for these visits and attempting to incorporate them into the combined spectrum is a poor use of processing time. Therefore, we elected to implement the following visit rejection scheme *before* the visits are submitted for RV determination and combination: If a visit spectrum's S/N is three standard deviations below the median S/N of the star's visit spectra, or if the S/N of the visit is below 1, then the visit is rejected. However, we also ensure that a visit is not rejected if its $S/N > 10$, regardless of these other two criteria.

Color-Temperature and $\log g$ Grid-Selection Prior

As discussed in §2.1 and below, RVs at the `apStar` level are *relative* RVs derived by cross-correlating the actual visit spectra against themselves and the visit-combined spectrum. However, to put them on an absolute scale a synthetic template is chosen by finding the best fit to the combined spectrum from within a grid of synthetic spectra. One of the issues the DR12 RV code often encountered was choosing a poor synthetic template from which to determine the absolute RVs. Most commonly, metal-poor stars were mistaken as hot stars due to their weak lines, and noisy spectra were mistaken as being from metal-rich cool stars. This latter case was a major concern for these faint targets as noise artifacts would be treated as real spectral lines, thus leading to erroneous RV measurements. To mitigate this problem, we used the $(J-K)_0$ color of the star to construct a "temperature prior" using the color-temperature relations from González Hernández & Bonifacio (2009):

$$\frac{5040\mathrm{K}}{T_{\mathrm{eff}}} = b_0 + b_1(J-K)_0 + b_2(J-K)_0^2 + b_3(J-K)_0[\mathrm{Fe/H}] + b_4[\mathrm{Fe/H}] + b_5[\mathrm{Fe/H}]^2, \quad (4.1)$$

where the b_i coefficients are given in Table 5 of González Hernández & Bonifacio (2009). The dereddened color is calculated from the A_K value adopted for targeting [7]. Because the metallicity of the star is not known *a priori*, we input the range of metallicity expected for stars in APOGEE ($-2.5 \leq [M/H] \leq 0.5$) into equation 4.1, and adopt the range of values for $T_{\rm eff}$ output, extended by 500K in both directions, as the range of grids we allow the code to search. Under most conditions, this resulted in a $\sim 1500 - 2000$ K range of permitted $T_{\rm eff}$. Furthermore, if the star was identified as a dwarf or giant from Washington photometry, we restricted the $\log g$ range of the grid that the code was permitted to search, with giants required to have $\log g < 4$, and dwarfs required to have $\log g \geq 3.5$.

Updates to RV Refinement Iterations

Previous versions of the `apStar` RV determination and visit combination routines involved an iterative procedure where, ideally, after a first iteration using the highest S/N visit spectrum as a template, an ever improving combined spectrum was used as the RV template against which the visits were cross-correlated, leading to a rapidly-convergent RV solution. Only at the very end of the routine were synthetic templates invoked both to put the aforementioned relative RVs on an absolute scale, and as a final check on the reproducability of the RVs and reliability of the visit combination. This procedure worked extraordinarily well for even moderately faint ($H \sim 14$) stars, which covered the vast majority of APOGEE-1 targets. However, if the initial iteration loops derive largely incorrect RVs that lead to a poor combined spectrum, then the iterative process is often *divergent*, with the combined spectrum getting worse on each iteration. There were three main changes to the iteration loop implemented to

[7] Or the A_K value derived from WISE if the targeting value is negative or NaN. If no reported A_K value is positive, then we do not restrict the grid in T_{eff} space.

avoid such a scenario:

1. **Inclusion of synthetic template in iterations** – The visit spectra are cross-correlated against *both* the synthetic template and observed combined spectrum (placed on the same velocity scale) to get velocities relative to the templates. The calculated velocities at this stage are always relative to the previous combination, so they are added to the previous results to get the true relative velocities. Heliocentric velocities and their scatter are then calculated for each method, excluding any visits that would be rejected using that method (see next point), and the method that produces the lowest scatter is selected for the combination.

2. **Outlier rejection** – We found that a single visit with a significantly deviant RV often caused other visits to diverge from their well-behaved solution. Therefore, we elected to reject visits, and not include them in the combination if:

   - The velocity or its uncertainty become non-finite, which is usually indicative of an error in correlation or combination,
   - The cumulative relative velocity selected for combination exceeds 1000 km s^{-1},
   - If $|v^i_{helio} - \mathrm{median}(v_{helio})| > \max(10 \times \mathrm{mad}(v^i_{helio}), 4\ \mathrm{km\ s^{-1}})$, where v^i_{helio} is the Heliocentric RV for visit i, $\mathrm{median}(v_{helio})$ is median RV for the star, and mad indicates the median absolute deviation of the visit compared to the median RV for the star.

   Since DR14 will be the first large-scale implementation of these rejection criteria, we chose to keep them relatively relaxed as to not eliminate true RV variations.

3. **Adjustment to masking procedures** – When a combined spectrum is produced, a bad pixel mask for the spectrum is produced by performing a bitwise OR operation on the individual visit bad pixel masks. When this new combined spectrum becomes the RV template for the next iteration, these pixels are ignored in cross-correlation. However, in low S/N spectra too many (in some cases up to 90%) pixels being masked out, since even the weakest sky lines are prominent in the spectrum. This results in the combined spectrum not being useful as an RV template. Therefore, if over half of the pixels in the combined spectrum are masked out in the OR combined mask, we use a bitwise AND combined mask. This ensures that more pixels are usable in the combined spectrum, with the only masked pixels being those where every visit provided a bad pixel. Since bad pixels from visit spectra are heavily downweighted both in combination and when the combined spectrum is cross-correlated against a visit, this masking paradigm still eliminates the impact of bad pixels.

As before, the iterative procedure ends after 10 iterations unless velocity adjustments between iterations are below 0.01 km s^{-1} or if all visits have been rejected. Once the iterations are complete, all velocities are put back on a absolute scale, and the velocities derived both from using the synthetic template and from the observed combined template are stored under the `SYNTHVHELIO` tag and the new `OBSVHELIO` tag in the `apStar` files, respectfully. The velocity method that produced the smallest scatter, and thus used in combination, is indicated by the new `COMBTYPE` tag, and the actual values are stored in the `VHELIO` tag, as usual. As before `SYNTHSCATTER` = stddev(`OBSVHELIO` − `SYNTHVHELIO`), and we use the following

relation to test the reliability of the RVs, and of the combined spectrum:

$$\texttt{SYNTHSCATTER} > \max(n\,\mathrm{km\ s^{-1}}, n\sigma_v), \tag{4.2}$$

where σ_v is the standard deviation of `VHELIO`. If the above relation is satisfied with $n = 2$ then the `SUSPECT_RV_COMBINATION` flag is set, and if it satisfied with $n = 10$, a new `BAD_RV_COMBINATION` flag is set. I recommended these flags be propagated into the `STAR_WARN` and `STAR_BAD` flags in ASPCAP, respectively. The most common culprits for triggering these flags are double-lined spectroscopic binaries (SB2s), so these flags are a quick and easy way to select potential SB2s from the APOGEE data.

4.2.3 Overall RV Performance

In measuring the overall performance of the APOGEE RVs, `vscatter` = stddev(v_{helio}) represents a more realistic measure of a star's velocity scatter due to instrumental (and astrophysical) effects. In Figure 4.6, we see that the RVs derived using the DR14 routines overall produce a smaller scatter than those used for DR13, with the peak of the distribution moving from ~ 80 m s^{-1} in DR13 to ~ 50 m s^{-1} in DR14. As in DR12 and DR13, the long tail of higher `vscatter` are from the binary stars in the APOGEE sample.

Figure 4.7 shows the visit-to-visit velocity scattter (`vscatter`) of DR14 stars with at least three visits as a function of the median visit S/N achieved for the stars and demonstrates RV performance as a function of stellar parameters. As expected, stars with the least line-profile broadening (low values of $v \sin i$ and $\log g$[8]), and the most lines (metal rich cool[9] stars) produce the best RVs, with `vscatter` approaching

[8]The increased median `vscatter` values for stars with $\log g < 1$ is due to the large intrinsic atmospheric RV jitter for these stars (see Equation 2.30).

[9]The upturn in median `vscatter` for the coolest stars ($T_{\rm eff} < 4800$ K) is related to RV jitter

$\sim$ 10m s^{-1} levels for the highest S/N sources.

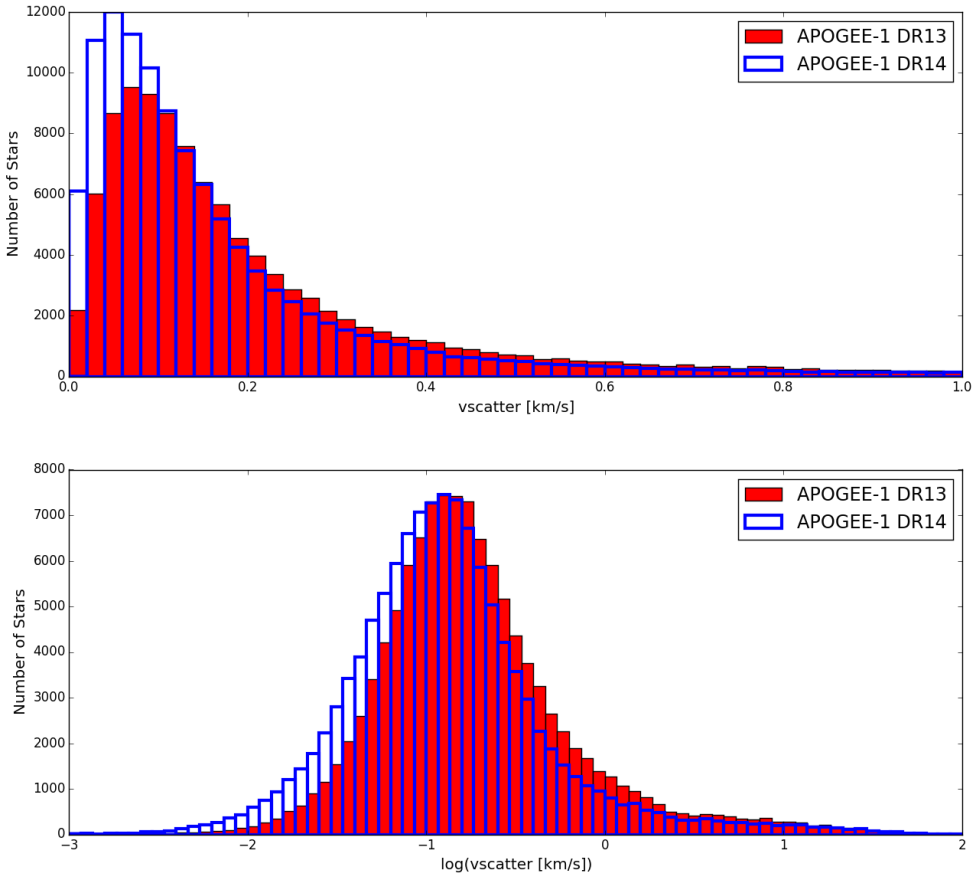

Fig. 4.6.— A comparison `vscatter` (or $\log of$`vscatter` in the bottom panel) distribution of APOGEE-1 targets in DR14 (blue open histogram) to the distribution in DR13 (red filled histogram). Stars included in this figure had at least three independent RV measurements and did not have the `SUSPECT_RV_COMBINATION` reduction flag set.

4.2.4 Dwarf Spheroidal Membership and Multiplicity

In Figure 4.8 we demonstrate the capability of the DR14 data to identify RV membership of the Ursa Minor dSph compared to the data derived using the DR13 routines. The current accepted median RV for Ursa Minor is $v_{helio} \sim -247$ km s^{-1} (Young

effect, as most of the coolest stars are giants, and T_{eff} and $\log g$ is correlated for giants.

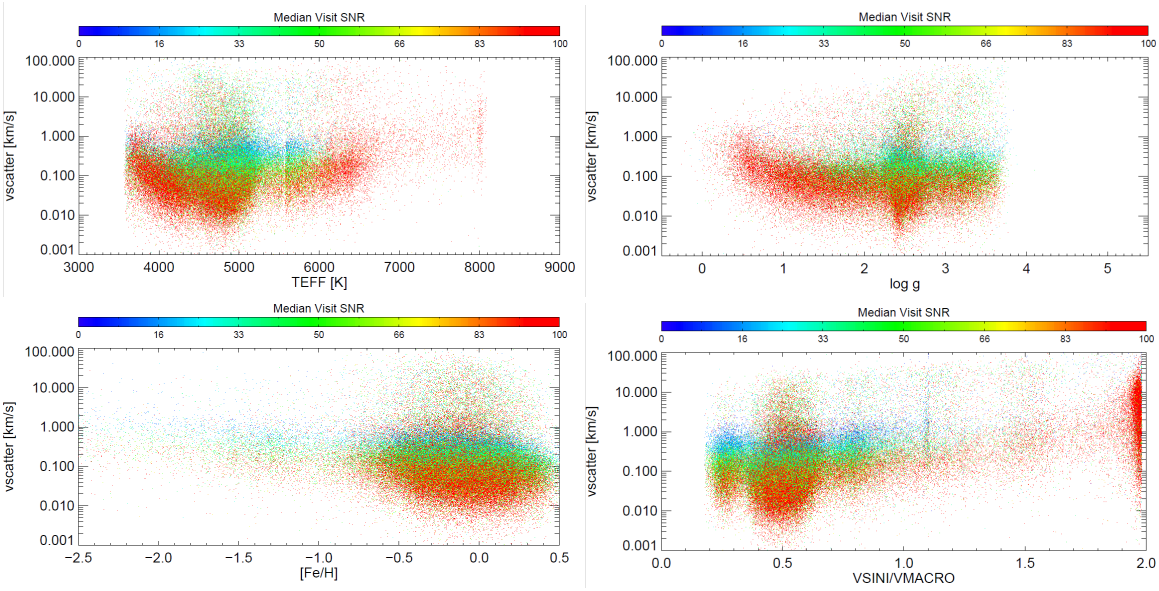

Fig. 4.7.— Visit-to-visit velocity scatter for stars in DR14 as a function of ASPCAP calibrated stellar parameters: $T_{\rm eff}$ (upper left), $\log g$ (upper right), [M/H] (lower left), $\log v \sin i$ or $\log v_{macro}$ (lower right). Points are color-coded by median visit S/N.

2000), so for this test any star that had $-300\,\mathrm{km\ s^{-1}} < v_{helio} < -200\,\mathrm{km\ s^{-1}}$ that did not have the `SUSPECT_RV_COMBINATION` flag set was considered an RV candidate. Overall the DR14 routine provide a vast improvement, providing 38 RV candidates, including three with median visit $S/N \leq 5$. This is to be compared to only nine RV members identified when using data derived using the DR13 routines. In addition, the typical visit-to-visit RV scatter for selected RV candidates is smaller in DR14 with the median scatter being 1.2 km s^{-1} compared to 2.2 km s^{-1} using the old routines. Furthermore, the new routines have a lower rate of visit rejection per star.

With the new RV routines, APOGEE's ability to pick out binary stars from the dSph members is also vastly improved. In the top panel of Figure 4.8, nearly every RV candidate looks like it may be a binary. However, in the bottom panel, we are able to distinguish between single stars (the darker blue points indicating `vscatter` < 1 km s^{-1}), and likely binaries, and a cursory investigation of the data in this panel indicates

that the binary fraction in the Ursa Minor dSph is ~ 0.40, which is consistent with the results of Minor (2013) who found a binary fraction of $0.46^{+0.13}_{-0.09}$ from a sample of four dSphs. Of course, more careful analysis of the binary fraction in dSphs observed by APOGEE will be undertaken in the future.[10]

Indeed, the improvements to the RV routines allow us to move beyond just gross identification of binaries in dSphs to Keplerian orbit fitting to determine orbital parameters. Figure 4.9 and Table 4.4 present the binary systems identified as Ursa Minor candiates selected using the "gold sample" quality criteria described in Troup et al. (2016). While orbital fits were also found to some of the members of the Draco dSph also observed by APOGEE-2, none of them yet meet the "gold sample" criteria, and are not included here. However, observations for Draco are incomplete and were taken over a relatively short baseline (about two months), so we expect more robust detections after Draco has acquired its full suite of visits.

4.2.5 Potential Future Improvement

Results from DR14 indicate that our currently implemented velocity outlier visit rejection criteria were slightly overzealous, leading to stars with only a few "good" visits out of a dozen or more. One particular issue is that the code calculates velocity scatter after rejection, which means the code will choose the method (velocities derived using a synthetic template versus the combined spectrum) that rejects a visit even if the other method keeps all of its visits with slightly greater scatter. In future short-term implementations of this code we will not reject visits unless it is flagged as an outlier in both velocity-derivation methods, which can be fixed simply by moving the scatter calculation before outlier rejection.

[10] For example, Hannah Lewis is attempting to determine a revised velocity dispersion of the Ursa Minor and Draco dSphs by removing influence of binary stars.

The current grid of synthetic spectra used for RV templates is very coarse, does not include potential rotational broadening (which is a problem when attempting to derive RVs for hot and young stars), and has not been updated since very early in survey. An obvious solution would be to make a new RV grid from a subset of the ASPCAP libraries. In fact, the "coarse" grids used in the first stage of ASPCAP to determine which full library is the most appropriate for the star may be well suited for this purpose.

The visit level RV derivation routines have the option to use a direct-pixel matching method to derive the RVs whereby the spectrum is split into chunks and the RV shift for each chunk that results in the lowest χ^2 when matching the spectrum to a template is found (See §8.1 of Nidever et al. 2015). This works well for cool metal rich stars, and provides a more realistic estimate of the RV uncertainty (which is often underestimated in cross-correlation). We have some infrastructure in place to perform this at the visit combination level, both using synthetic and observed spectra as templates, but it is not fully implemented or tested. As APOGEE-2 collects more spectra this may be a worthwhile upgrade to pursue.

Finally, to fully trace instrumental drift in the RVs, we have considered using the sky lines, which remain at a fixed wavelength in the star's spectrum, as a secondary wavelength calibration source. Taking this a step further, eventually we would like to install a Fiber-Fabery Perot Interferometr (FFP) calibration source on the APOGEE instrument. We discuss these potential improvements further in Chapter 6.

Table 4.1. ASPCAP DR13 Grid Parameters

Grid	$T_{\rm eff}$ (kK)	$\log g$	v_{micro} (km s^{-1})	[M/H]	[C/M]	[N/M]	[α/M]	$v \sin i$ (km s^{-1})[a]
Fd	5 - 8	1 - 5	0.5 - 8	-2.5 - 0.5	0	0	-1 - 1	1.5 - 96
GKd	3 - 6	3.5 - 5	0.5 - 8	-2.5 - 0.5	0	0	-1 - 1	1.5 - 96
GKg	3 - 6	0 - 4	$f(g, [M/H])$	-2.5 - 0.5	-1 - 1	-1 - 1	-1 - 1	$f(g, [M/H])$
Md	2.5 - 4	3.5 - 5	0.5 - 8	-2.5 - 0.5	0	0	-1 - 1	1.5 - 96
Mg	2.5 - 4	-0.5 - 4	$f(g, [M/H])$	-2.5 - 0.5	-1 - 1	-1 - 1	-1 - 1	$f(g, [M/H])$

[a]Projected rotational velocity for the dwarf(d) grids and v_{macro} for giant(g) grids.

Table 4.2. Anomalously Rapid ($v \sin i > 20$ km s^{-1}) Rotators in M67

APOGEE_ID	$T_{\rm eff}$ (K)	$\log g$	$v \sin i$ (km s^{-1})	Comment[a]
2M08504952+1217158	4507.	4.11	68.6	SB2
2M08510351+1145027	6515.	3.64	78.5	BS
2M08510483+1145568	5274.	3.97	95.8	W UMa (X-Ray) EB
2M08510576+1143469	5542.	4.41	35.0	SB2
2M08510723+1153019	4639.	3.43	77.1	X-Ray EB
2M08511178+1145220	7987.	4.89	82.4	BS
2M08511759+1139359	5807.	4.04	48.8	SB2
2M08512530+1202563	4336.	3.47	55.3	RS CVn EB
2M08513259+1148520	7443.	4.28	28.0	BS
2M08513553+1139469	5821.	4.51	33.4	SB2
2M08513784+1150570	3354.	3.27	92.8	W UMa (X-ray) EB
2M08514864+1149156	7604.	4.23	60.0	BS

[a]Comment on the potential source of rapid rotation: SB2 = Double-lined spectroscopic binary confirmed by Chojnowski et al. (2015) using APOGEE spectra, BS = Blue Straggler(BS) identified by Liu et al. (2008), EB = Some kind of Eclipsing Binary(EB) identified in SIMBAD, with specific class available if noted in SIMBAD.

Table 4.3. Moderately Rapid ($v \sin i > 10$ km s^{-1}) Rotators in M67

APOGEE_ID	$T_{\rm eff}$ (K)	$\log g$	$v \sin i$ (km s^{-1})	Comment[a]
2M08502698+1148313	6487.	4.91	15.0	SB2
2M08505923+1146129	5722.	4.29	17.5	??
2M08511176+1150018	4866.	4.27	10.8	??
2M08511698+1150093	6244.	4.38	12.8	??(BS?)
2M08512079+1153261	6262.	4.11	16.0	BS
2M08512175+1152378	5600.	3.52	14.3	BS
2M08512467+1143061	5477.	4.52	12.5	??
2M08512643+1143506	7995.	4.62	15.3	BS
2M08512788+1155409	5787.	4.19	10.9	??
2M08513701+1136516	5330.	4.51	16.5	??
2M08513724+1146557	5948.	4.41	14.3	SB2
2M08514742+1147096	5178.	4.15	15.8	??
2M08515104+1137025	6037.	3.98	12.4	?? (BS?)
2M08515309+1140536	5754.	3.96	11.8	SB2

[a]Comment on the potential source of rapid rotation: SB2 = Double-lined spectroscopic binary confirmed by Chojnowski et al. (2015) using APOGEE spectra, BS = Blue Straggler(BS) identified by Liu et al. (2008), ?? = No explanation in the literature for high rotation rate, BS? = indicates stars that may be previously unidentified blue stragglers.

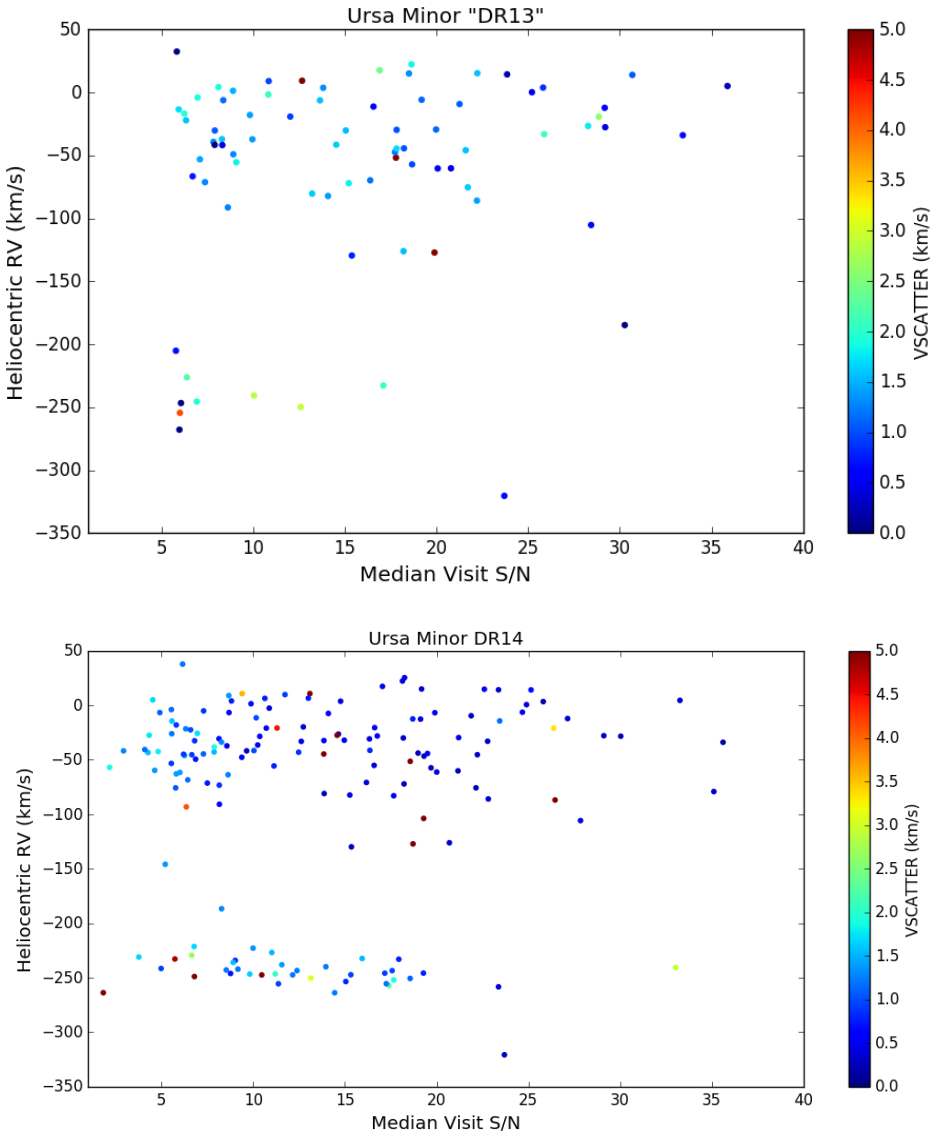

Fig. 4.8.— Heliocentric RV vs. median visit S/N for all stars in the Ursa Minor dSph field that did not have the `SUSPECT_RV_COMBINATION` flag set. Color indicates the visit-to-visit velocity scatter for each star. The top panel shows the results using DR13 reduction methods, and the bottom panel presents the DR14 results.

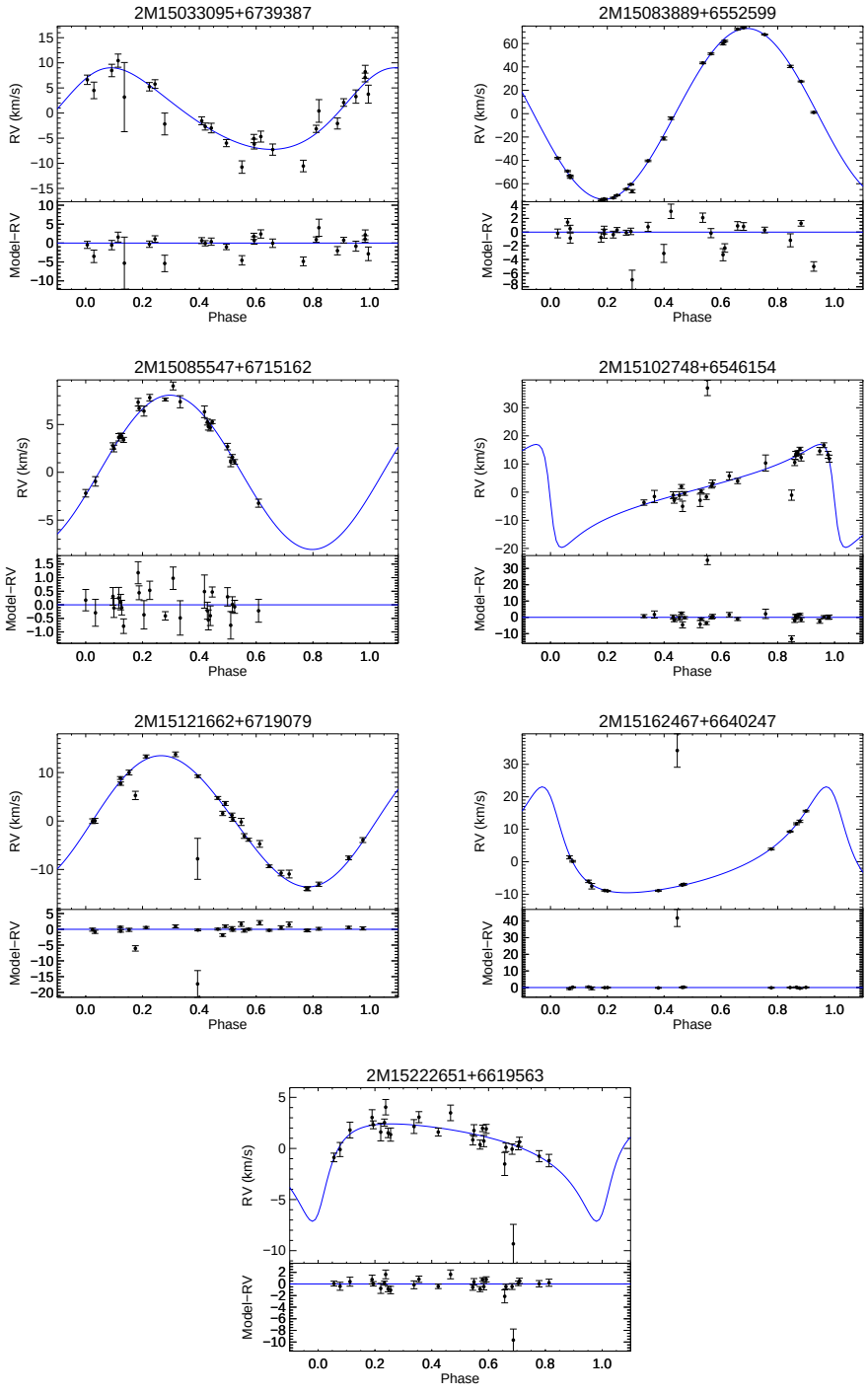

Fig. 4.9.— RV curves of "gold sample" binaries identified as Ursa Minor candidates. Draco has fewer epochs over a shorter baseline (two months compared to a year) than Ursa Minor, but has more observations scheduled, so we expect "gold sample" binaries from Draco in the next data release. Orbital parameters for these systems can be found in Table 4.4

Table 4.4. Orbital Parameters of Binary Ursa Minor dSph Candidates

APOGEE_ID	P (days)	K (km s^{-1})	e	$m \sin i$ ($M_\odot$)	a (AU)
2M15033095+6739387	45.95	8.12	0.15	0.123	0.206
2M15083889+6552599	3.30	73.15	0.01	0.568	0.024
2M15085547+6715162	291.94	8.07	0.00	0.399	0.868
2M15102748+6546154	272.42	18.32	0.71	0.412	0.523
2M15121662+6719079	3.72	13.54	0.03	0.080	0.038
2M15162467+6640247	89.33	16.30	0.51	0.244	0.241
2M15222651+6619563	230.30	4.77	0.59	0.099	0.611

Chapter 5

Combing the Brown Dwarf Desert with the APOGEE-2 DR14 Companion Catalog

The APOGEE-2 survey is a six-year extension of the APOGEE survey as a part of SDSS-IV. APOGEE-2 continues the APOGEE-1 survey of the Northern Hemisphere at Apache Point Observatory (APO), and implements a new, second observing facility, the DuPont Telescope at Las Campanas Observatory (LCO), to cover the Southern Hemisphere. Operations in the Southern Hemisphere began in the (Southern) summer of 2017, and the first data from the Southern Hemisphere will be made available with the next APOGEE data release (DR15). In the mean time, the northern instrument has been collecting additional data since the summer of 2014, and we use these data to build a new catalog of APOGEE-2 stellar and substellar companions, which we present in this chapter.

5.1 New Techniques and Data Sources

In this work, we use data from the fourteenth data release (DR14) of the Sloan Digital Sky Survey (SDSS-IV), in particular the high-resolution, time-domain, infrared spectroscopy of the Apache Point Observatory Galactic Evolution Experiment (APOGEE; Majewski et al. 2015). APOGEE DR14 includes the first two years (2014 - 2016) of Northern Hemisphere APOGEE-2 observations as well as the three years (2011-2014) of the original SDSS-III APOGEE-1 survey. In total, APOGEE has taken observations of 258,475 stars as of July 2016, the cutoff date for DR14. As described in Chapter 2, to perform reliable Keplerian orbits, we require a star to have > 8 visits, and not have the STAR_BAD or BAD_RV_COMBINATION flags set. In contrast to our work with DR12, here we also study stars used as telluric standards in APOGEE, because we have found that many of these stars are actually quite suitable for RV work. Using these initial selection criteria, we processed a parent sample of 15,536 stars with the `apOrbit` pipeline. As can be seen in Figure 5.1, this parent sample spans a wide range of evolutionary states and spectral types with an observational baseline of up to 1800 days over as many as 48 epochs.

The methods we use to determine host star properties, derive orbital parameters, and select companion candidates for APOGEE's DR12 catalog of stellar and substellar companion candidates are described in Chapter 2. Here we describe new data products used to produce the DR14 catalog.

5.1.1 Updated methods for determining stellar parameters

With the inclusion of APOGEE-2 data in our survey along side APOGEE-1 data, the situation arose where stars would have multiple entries in the DR14 database[1], but with slightly different stellar parameters due to varying SNR of the entries' combined spectra. For stars with multiple entries, we average the pipeline-derived stellar parameters ($T_{\rm eff}$, $\log g$, $v \sin i$) and abundances ([Fe/H], etc.), weighting by each entry's combined S/N, with a weight of zero applied to commissioning entries, or entries with the `STAR_BAD` flag set or missing parameters.

With the release of the Tycho-Gaia Astrometric Solutions (TGAS; Gaia Collaboration et al. 2016), we can use TGAS parallaxes to derive distances for the nearby stars in the APOGEE sample, as long as $\sigma_\pi/\pi < 0.2$.[2] Even with this limited Gaia release, 944 stars ($\sim 6.1\%$) of our APOGEE parent sample have distances derived from the APOGEE-TGAS sample. Our ultimate goal is to have all of our distances uniformally derived from Gaia parallaxes, when the are available. In the mean time, we continue to use a variety of means to ascertain the distance to the star, including using the APOGEE Red Clump catalog as standard candles (892 stars; Bovy et al. 2014) and Bayesian statistical distances derived by members of the APOGEE team (12011 stars). We also added a provision that if a star is identified as a cluster member we adopt the cluster's mean distance (and uncertainty) as the distance to the star (four stars). If a star has multiple distance measurements, then the source with the smallest estimated distance uncertainty is adopted. If no distance measurement is available, we derive the distance from the calculated mass of the star (1585 stars). For more details on how these calculations are performed, we refer to the reader back

[1] If a star is observed in more than one APOGEE field, then the reduction pipeline treats them as separate stars, resulting in multiple entries in the APOGEE database.

[2] Based on the original recommendation of Lutz & Kelker (1973).

to §2.2.4.

Masses are derived independent of the distance whenever possible; for example, attempting to calculate the mass of dwarf stars from the Gaia-derived distances often produced erroneous results such as a star with $T_{\rm eff} = 7000$ K having a derived mass of only 0.5 $M_{\odot}$. Therefore, for all dwarfs and subgiants (9065 stars) we elected to continue to use the Torres et al. (2010) relations to derive masses from their measured $T_{\rm eff}$, $\log g$, and [Fe/H] (see Equation 2.11) regardless of whether the star has a distance measurement. We also added functionality so that catalogs containing direct mass measurements could be incorporated. As of DR14, the only such catalog was the DR14 APOKASC catalog, and nine stars from our parent sample adopted their primary mass from this catalog. For the remainder of the stars, the primary mass is derived from the distance (6439 stars). We refer to the reader back to §2.2.3 and §2.2.4 for how host star masses can be determined from calculated distances in our sample. For field giants, if no mass or distance measurement is available, we use a mass of $1.6 M_{\odot}$, determined by Trilegal (Girardi et al. 2005) simulations (see §2.2.4). This was required for only 22 stars. We plan on implementing a more robust "default" mass using each star's parameters in conjunction with Trilegal simulations rather than a global median as we currently use.

5.1.2 Check against rotational velocity aliasing

Starting in DR13 (SDSS Collaboration et al. 2016), APOGEE uses separate spectral grids to analyze giants and dwarfs. The grids for dwarfs included a dimension to measure rotational velocity (see also §4.1). This new information allows us to add a new false-positive check to our orbit-fitting pipeline by flagging orbital solutions where the orbital period matches the rotational period.

The rotational period can be derived from observable quantities:

$$P_{rot} = \frac{2\pi R_\star}{v_{rot}} = \frac{2\pi R_\star}{v \sin i} \sin i = P_{rot}^{max} \sin i, \tag{5.1}$$

where $P_{rot}^{max} = 2\pi R_\star/(v \sin i)$ depends only on quantities for which we have observed or derived values, and represents the maximum possible rotational period of the star. We do not know the inclination of the system, so we must treat it statistically. The probability distribution function of inclination is

$$p(i) = \sin i, \tag{5.2}$$

so the probability that a system has an inclination in the range $[i_{min}, i_{max}]$ is

$$\mathbf{P}[i_{min} \leq i \leq i_{max}] = \int_{i_{min}}^{i_{max}} \sin i di \tag{5.3}$$

$$= \cos i_{min} - \cos i_{max}, \tag{5.4}$$

where i can take values in the range $[0, 90°]$.

If there is a maximum and minimum orbital period, P_{max} and P_{min}, we wish to consider then the corresponding inclination values are

$$i_{max} = \arcsin(P_{max}/P_{rot}^{max}) \tag{5.5}$$

$$i_{min} = \arcsin(P_{min}/P_{rot}^{max}). \tag{5.6}$$

Therefore,

$$\mathbf{P}[i_{min} \leq i \leq i_{max}] = \sqrt{1 - (P_{min}/P_{rot}^{max})^2} \tag{5.7}$$

$$-\sqrt{1 - (P_{max}/P_{rot}^{max})^2} \tag{5.8}$$

If $P_{max} \geq P_{rot}^{max}$ then $\mathbf{P}[i_{min} \leq i \leq i_{max}] = \sqrt{1 - (P_{min}/P_{rot}^{max})^2}$ due to the second term becoming imaginary, and if $P_{min} \geq P_{rot}^{max}$ then $\mathbf{P}[i_{min} \leq i \leq i_{max}] = 0$ by definition.

We want to find the probability that an orbital period suggested by our pipeline is within 5% a multiple ($n = 1, 2, 3$) of the rotational period, so for each orbital solution with period P_{orb}, we set the maximum and minimum orbital periods to consider in Equation 5.8 to $P_{max} = \frac{1.05 P_{orb}}{n}$ and $P_{min} == \frac{0.95 P_{orb}}{n}$. If we can rule out with 95% confidence ($\mathbf{P} < 0.05$) that the orbital period and rotation period are not the same, then the orbital solution is acceptable, otherwise a new `PROTWARN` flag is set for the solution. This flag being set has been added to the marginal fit criteria described in 2.3.4, selecting an alternative orbital solution if one is available. However, we also need to consider systems where the companion's orbital period has synchronized with the rotation period of the host star. Therefore, the `PROTWARN` flag will not result in a system being rejected from the gold sample if no suitable alternative orbital solution can be found.

5.1.3 CCF Bisectors

Another false positive check involves investigating the cross-correlation functions (CCFs) produced when deriving the RVs from the stellar spectra (e.g., Dall et al. 2006; Batürk et al. 2011). When a sufficiently bright companion is orbiting a star, the influence of the companion will manifest itself as a second peak in the CCF. While we are able to flag systems where the peak of a companion star clearly breaks from the primary (known as double-lined spectroscopic binaries, or SB2s), we had no mechanism to detect situations where a secondary star does not cause strong enough RV variations to be resolved out from the main peak. In this situation, we can instead

measure changes in the shape of the CCF that indicate the presence of a luminous companion. We do this by calculating a bisector of the CCF at each epoch, and observing changes in the bisector inverse slope (BIS) and the bisector's curvature (c_b), which are defined as:

$$BIS = \bar{v}_{55-85} - \bar{v}_{10-40} \tag{5.9}$$

$$c_b = (\bar{v}_{70-90} - \bar{v}_{40-60}) - (\bar{v}_{40-60} - \bar{v}_{10-30}), \tag{5.10}$$

where $\bar{v}_{X-Y}$ is the average velocity deflection between a normalized flux level of $X\%$ and $Y\%$ with the deepest point of the CCF defined as 0% and the continuum level is defined as 100%. While the CCF is generally reported as a positive function, this convention is used to emulate similar measurements with traditional line bisector methods.

We have implemented methods to perform this calculation on all APOGEE stars of interest. Typically this technique requires both high resolution (typically $> 50,000$) and high S/N. To accommodate APOGEE's lower resolution we perform Gaussian smoothing on the CCFs before calculating the bisectors, and we do not perform bisector calculations on data from visits with $S/N < 20$. For each star with at least three epochs in which bisectors were calculated, we report the standard deviations of BIS and c_b, as well as the linear correlation coefficient of $BIS(R_{BIS})$ and $c_b(R_{c_b})$ with the star's RV measurement.

Moving forward, we will further automate this process, allowing us to determine the flux ratio required to create such variations given derived orbital parameters. This, in turn, will allow us to determine the true mass of the companion, and break the inclination degeneracy inherent in RV observations. In the mean time, we wanted to at the very least flag systems where the bisector variations indicate the mass

derived from the orbital solution may not be representative of the true mass of the companion.

To mark candidate systems where we believe the bisector variations represent potential false-positive signals, we introduce a new `BISECTOR_WARN` flag. Systems where the companion would provide a significant fraction of the flux for the system are *expected* to have some kind of bisector variation, so we do not set the `BISECTOR_WARN` flag if the companion flux would be expected to be $> 5\%$ of the primary star, which, for a pair of main sequence stars, corresponds to a mass ratio $q \sin i = m \sin i / M_\star > 0.425$. For candidate systems with $q \sin i < 0.425$, we found a correlation between σ_{BIS} and median RV uncertainty for the star ($\tilde{v}_{unc}$ from §2.4.1), as can be seen in the top panel of Figure 5.2. Visual inspection of the bisectors revealed that systems where BIS and RV measurements were highly correlated ($|R_{BIS}| > 0.5$) had a higher probability of being astrophysical (due to an unresolved luminous companion) rather than bisector variations due to instrumental effects (such as spectra experiencing differences in focus depending on the exact position of the focal plane). Therefore, we adopted the following flagging criteria:

$$\frac{\sigma_{BIS}}{\tilde{v}_{unc}} \geq 3 + 3(1 - R_{BIS}) \tag{5.11}$$

From the visual inspections, we also learned that for $\sigma_{BIS} < 0.4$ km s^{-1}, bisector variations are dominated by fiber-to-fiber variations of the instrument LSF (see middle panel of Figure 5.2). Therefore any star with $\sigma_{BIS} < 0.4$ km s^{-1} is *not* flagged.

5.2 Building the DR14 Catalog of RV Companion Candidates

All stars in the parent sample have primary stellar parameters determined. However, only stars that demonstrate significant RV variations (as determined by Eq. 2.2) are subjected to period finding in our study. In DR14, this results in only 3358 stars out of 15,536 from the parent sample being considered. From these only stars for which significant periodic signals are found are subjected to full Keplerian orbit fitting, which, with DR14, results in Keplerian orbital solutions being determined for 2862 stars. Again, this procedure is in place to lower the number of potential false positives permitted through the pipeline and to reduce the run time of the pipeline.

These 2862 stars were processed through the `apOrbit` pipeline and gold sample selection criteria described in Chapter 2 with the modifications described in the previous section. Of the 2862 stars for which full orbital solutions were derived, 1053 had at least one potential solution (typically out of six) where the `PROTWARN` flag was set, which, in some cases, means that a previous best solution would no longer be eligible for gold sample status and another best solution was chosen. In all, 832 candidate systems would have been included in the "gold sample" using the DR12 criteria with the additional rotation criterion. Of these, 106 stars (out of 552 for which bisector statistics were calculated) had the `BISECTOR_WARN` flag set, and were rejected from the DR14 gold sample, reducing it from 832 to 726. Any star with this flag set is then subsequently removed from the gold sample, as the reported $m \sin i$ no longer accurately reflects the nature of the system. We performed addition quality checks on this initial sample of 726 stars which we describe below. These checks led to adjustments of the gold sample criteria, and led to the final DR14 gold sample

presented in §5.2.2.

5.2.1 Comparison to DR12 Catalog

An alarming initial find was that there were 189 stars in the DR12 orbit catalog that are now excluded from this initial DR14 gold sample. Of these, 16 no longer met the criterion for even the parent sample. Of the remaining stars, 27 had revised RV measurements leading them to longer be RV variable based on the criteria $\Sigma_{RV} \geq 2.5$ (see Eq. 2.2) and seven stars no longer registered strong enough periodic components. These stars were not submitted for complete Keplerian orbit fitting in DR14. Of the 139 systems where orbits were derived, only eight had additional epochs in APOGEE-2, meaning most of the newly rejected systems are solely due to either the new rejection criteria (see §5.1.2 and 5.1.3), or updated stellar parameters and/or RVs since DR12 that changed the system's orbital solution. Of the 139 DR12 candidate systems now rejected, 115 were rejected based on applying the original DR12 gold sample criteria (see §2.4.1 and §2.4.2) to their newly derived values in DR14, while the new bisector criteria (see §5.1.3) led to the rejection of the other 24 DR12 gold sample systems. Note, that of the 139 systems, a total of 20 had the rotation flag set (see §5.1.2) for what would have been its best solution, leaving a new best fit that no longer meets the original DR12 gold sample criteria. A complete accounting of retracted DR12 gold sample systems can be found in Table 5.1.

The 193 systems that overlap between the initial DR14 and DR12 gold sample are shown in Figure 5.3. There is generally good agreement between the orbital parameters derived in DR14 and DR12, and when comparing the top panel of Figure 5.3 to Figure 3.1, the general distribution of orbital parameters is also similar. The most notable difference is the lack of systems with $P < 10$ days (see bottom left

panel of Figure 5.3), which perhaps indicates that our sensitivity to this regime is not as robust as we originally thought. We also see in the bottom right panel of Figure 5.3 a continuation of the known pipeline issue that the eccentricity (e) is one of the less-well constrained orbital parameters. A large plurality of DR12 systems not in DR14 were rejected due to fit quality criteria (the three numbered equations in §2.4.2), which led us to re-evaluate some of our gold-sample selection criteria. To identify selection criteria where we may have previously been too lax, we used the systems that matched between DR12 and DR14 but that had no additional data taken in DR14, and found the ones that were closest to crossing each exclusion threshold. These are outlined in Table 5.2, where values closer to one means that the criterion is robust, not requiring modification, while criteria that deviate $> 10\%$ from unity in the DR14 overlap samples were reconsidered. Based on these results, the following stricter gold sample standards were adopted:

- $\frac{K}{|\Delta\tilde{v}|} \geq 5 + 5(1 - V_N)e$,
- $n_{iter} < 45$,
- $\frac{a(1-e)}{R_\star} \geq 1.2$,
- $V_N \geq e$.

The last three were added to the "marginal fit" criteria described in §2.3.4, with the second being the new maximum number of iterations the orbit fitting pipeline is allowed to perform (see §2.3.2). The final criterion was inspired by further visual scrutiny of individual orbital fits.

Table 5.1. Retracted DR12 Candidate Systems

DR14 Exclusion Cause	n	APOGEE_IDs
Not Eligible for DR14 Orbit Fitting		
Parent Sample Criteria	16	2M03033027+7944165, 2M03431065+3235323,2M03452106+3218178, 2M03543039+7939477, 2M04294257+5629439, 2M05202674+4251053, 2M06171599+0019388, 2M08150160+3151012, 2M11462469+010224, 2M11481919+0118185, 2M12211197+2704339, 2M12253745+2546127, 2M12274075+0007367, 2M17140626+4307331, 2M19335125+4253024, 2M19474741+2321103
$\Sigma_{RV} < 2.5$	27	2M00475315+8504023, 2M01471839+8454501, 2M03360422+4600053, 2M03475791+4759452,2M06373467+1702080, 2M07003681+0419556, 2M07323237+2100401, 2M08532372+1119098, 2M11512380+0033387, 2M12135300+1419452, 2M12161612+1411251, 2M12163377+1410469, 2M12192456+0000171, 2M12213892+1425172, 2M12415580-0809155, 2M13071335+1659591, 2M13084943+1705275, 2M13133317+1542134, 2M13414217+1805294, 2M13435045+2800384, 2M13454310+1819440, 2M18315033-0019362, 2M18575650-0315315, 2M19130255-0625100, 2M20531937+5012375, 2M21000032+5047506, 2M21254515+4412510
No Periodic Components	7	2M06315647+0504364, 2M12045063+1911396, 2M12105030+1910562, 2M12112555+1908295, 2M13461152+2653184, 2M17172331+4256556, 2M19292561+2626538
Best-Fit Orbit Removed From DR14 Gold Sample due to DR12 Criteria		
$K/\tilde{\sigma} < 3 + 3(1 - V_N)e$	7	2M00283971+8530377, 2M00301928+6648359, 2M00330093+8454150, 2M00394524+8449597, 2M08194758+3104102, 2M12401224-0648362, 2M13104680+1759363
Phase Coverage Criteria	8	2M00225114+6202031, 2M03360098+8032080, 2M04223850+5550407, 2M06172325+0000514, 2M06295025+1739189, 2M13150364+1806426, 2M18404988-0205151, 2M19541546+2141090
Fit Physicality Criteria	5	2M05311298+2718532, 2M12244488+2640386,2M14053944+2744230, 2M19123733+2724276,2M19424644+2318442

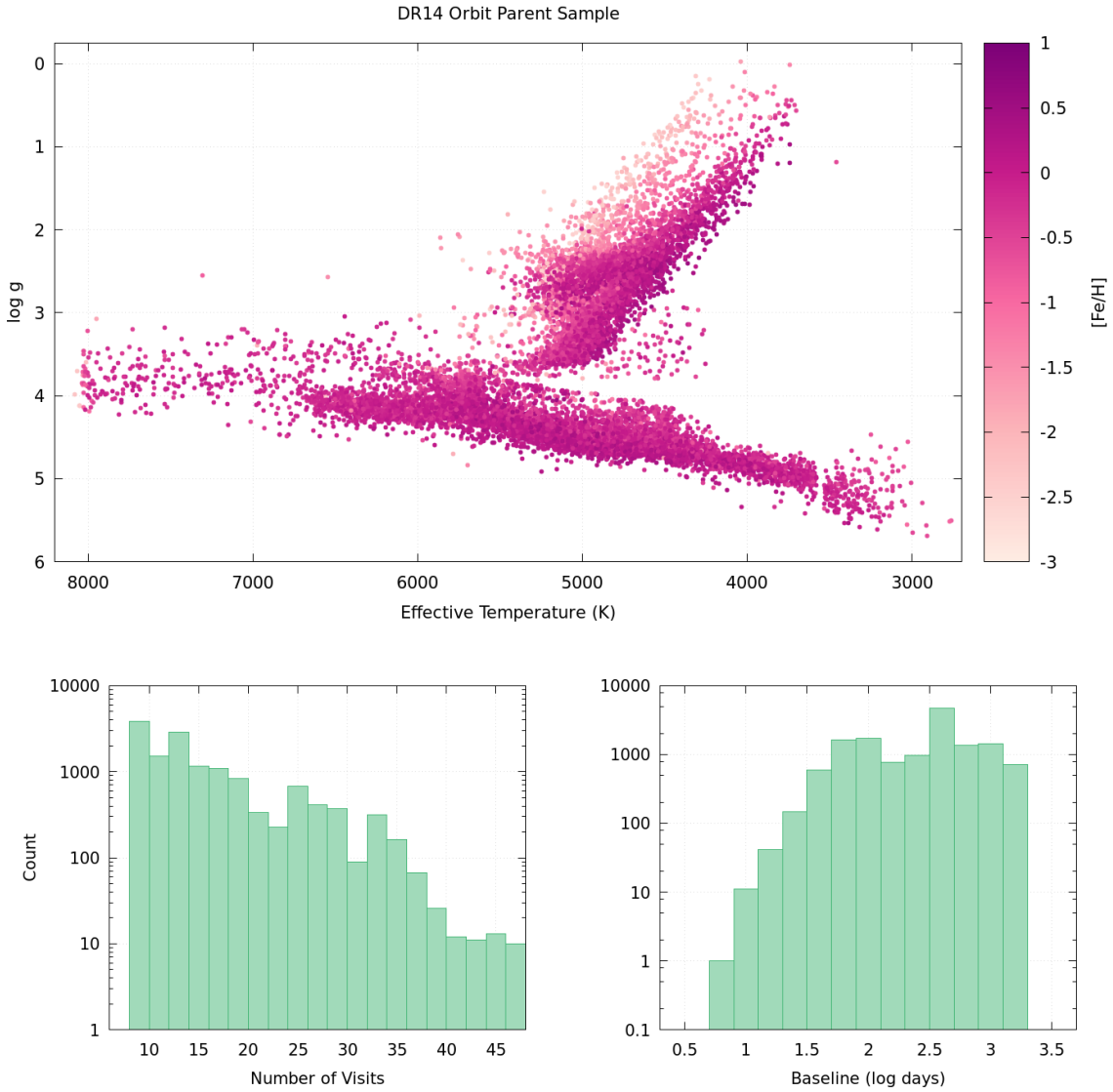

Fig. 5.1.— Distributions of the 15,536 star parent sample drawn from APOGEE DR14 for Keplerian orbit fitting. *Top panel:* Spectroscopic HR diagram ($\log g$ vs. $T_{\rm eff}$) color-coded by host star metallicity ([Fe/H]). *Bottom Panel:* Histograms of the number of epochs(visits) acquired (*left*) and the maximum temporal baseline of the observations (*right*).

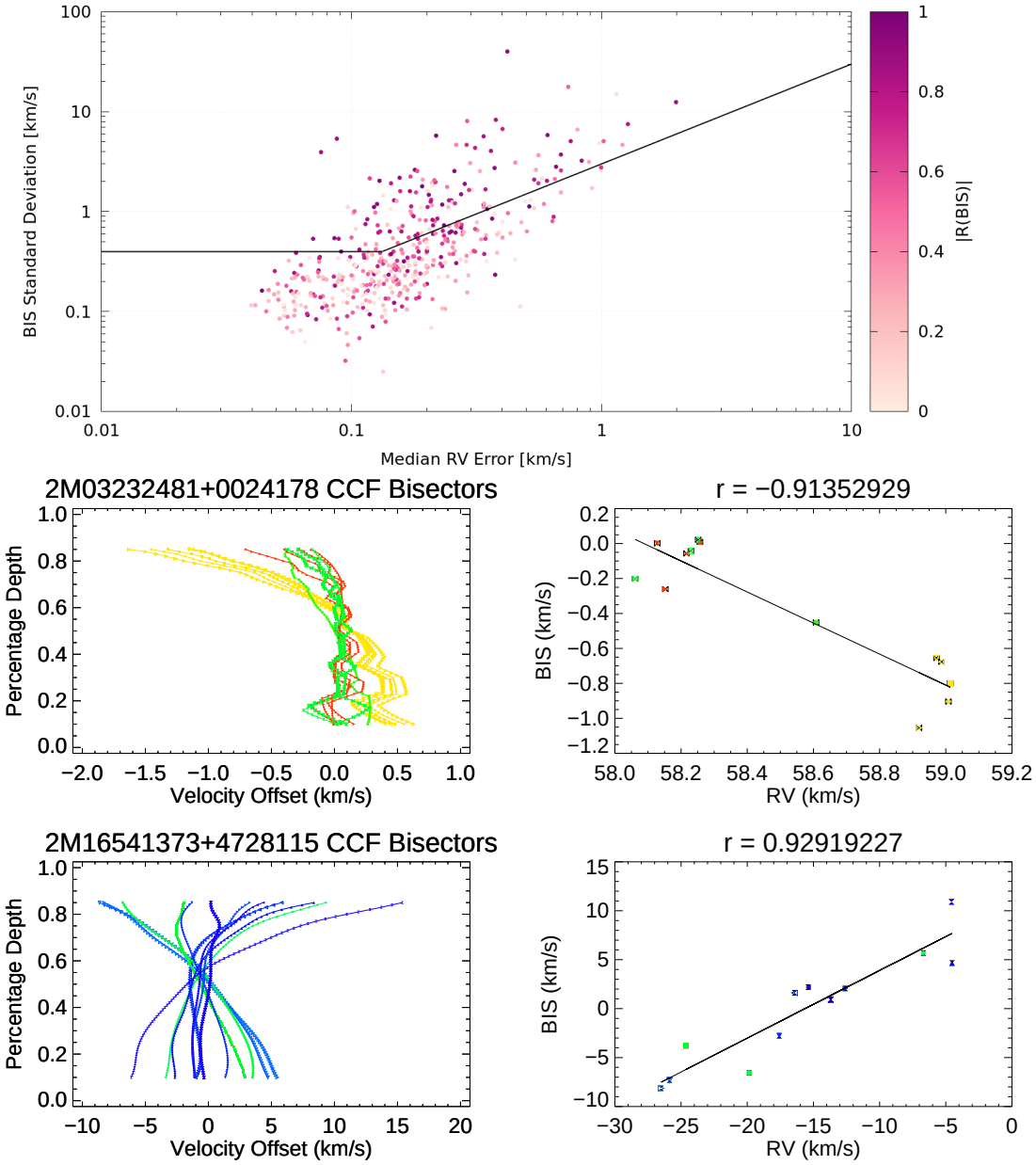

Fig. 5.2.— *Top Panel:* Demonstration of the criteria used to set the `BISECTOR_WARN` flag on the 466 stars selected using DR12 gold sample criteria for which $q \sin i < 0.425$ and ≥ 3 epochs of bisectors were calculated. The horizontal line indicates $\sigma_{BIS} = 0.4$ km s^{-1} and the diagonal line is $\sigma_{BIS} = 3\tilde{v}_{unc}$, which are the lower limits for which the flag is set. Color represents the correlation between each star's BIS and RV measurements. *Middle Panels:* Example of a system not flagged due to bisector variations correlated with fiber number (indicated by the color of the bisector). *Bottom Panels:* Example of a flagged system whose bisector variations are most likely due to a previously unresolved luminous companion.

Table 5.1—Continued

DR14 Exclusion Cause	n	APOGEE_IDs
Fit Quality Criteria (See 3 Numbered Eqns. in §2.4.2)	95	2M00110648+6609349, 2M00334291+6236198 2M00471754+8456301, 2M03123190+8018137, 2M03145671+8003470, 2M03252046+7909078, 2M03325390+8047161, 2M03405638+8018109, 2M03464334+4926498, 2M03553099+5203331, 2M03585279+5155016, 2M04073011+7923186, 2M04184590+5604107, 2M04212706+5543164 2M04373998+5736454, 2M04504284+5753538, 2M05225538+4304332, 2M05454972+3008464,2M05490717+2835566, 2M05495459+2808249, 2M05504316+2808440, 2M06070031+3040121, 2M06142559+3313468, 2M06171890-0012568, 2M06200704-0037219, 2M06343799+0645031, 2M06355361+0539085, 2M06575827+0350135, 2M06592037+0539140, 2M07163554+0608507, 2M07185787+0534187,2M08122482+3307108, 2M08474740+1248544, 2M08480285+1157534, 2M08483429+1225079, 2M11431623+0055135, 2M11434636+0030400, 2M11435456+0033196, 2M11440094+0034363, 2M11452461+0125173, 2M12164821+1455510, 2M12170968-0042550, 2M12182567+0048289, 2M12183673+1446115, 2M12205051+1356340, 2M12211694+1358233, 2M12220451+1413438, 2M12222252+1434366, 2M12224798+1333258, 2M12242433+0000450, 2M13131777+1705326, 2M13384893+1840175, 2M13405513+2709430, 2M13424327+1743151, 2M13431527+1910491, 2M13472690+2744293, 2M13483077+1745228, 2M13501100+1818464, 2M15142280+0024103, 2M15182185+0147091, 2M16355605+3552193, 2M16490085+4714427, 2M16514260+4703248, 2M17105698+4301117,2M17194150+4305034, 2M17214931+4221402, 2M18481414-0251133, 2M18504195-0311203, 2M19110770+2747154, 2M19114515-0725486, 2M19160171+2714504, 2M19270523+4105530, 2M19291780+4302004, 2M19315429+4232516, 2M19352118+4207199, 2M19405532+2401157, 2M19471487+2244208, 2M19565473+2206194, 2M20032039+2127112, 2M20111794+1908468, 2M20183197+1953430, 2M20511111+5054053, 2M20525666+4958258, 2M20533921+4948286, 2M20544193+5133387, 2M20544823+5017406, 2M20551781+5012028, 2M20555422+5036211, 2M20563173+5153589, 2M21182361+4817275, 2M21262850+1138426, 2M21264913+4515101, 2M21324071+1224030, 2M21380962+4208595, 2M21492557+4203285

5.2.2 The Refined DR14 Catalog

With the refined selection criteria described in the previous section, the final DR14 gold sample, presented in Figure 5.4, contains 736 stars, an $\sim$ 90% increase over the DR12 catalog published by Troup et al. (2016). Among the detected companion candidates in this sample, 242 are substellar mass ($\langle m \rangle = \frac{4}{\pi} m \sin i \leq 0.08 M_{\odot}$) including 178 candidate brown dwarf companions. The general distribution of candidate companions in this catalog confirms our previous findings in Chapter 3 of a highly truncated brown dwarf desert, since at separations of $a > 0.3$ AU there is no drop in the density of points in Figure 5.4 in the brown dwarf regime (0.013-0.08 $M_{\odot}$). This catalog contains orbital solutions for candidate systems with periods up to 2000 days (5.5 years), and semimajor axes up to 3.5 AU.

This catalog contains 552 host stars that were not in the DR12 orbit catalog, including 277 stars for which data were available in DR12. Of these, 103 acquired additional epochs of data in DR14, and the remaining 174 included 39 stars used as telluric standard stars that were not analyzed in DR12 with the rest either having updated stellar parameters that permitted their inclusion in the DR14 gold sample, or improved RV precision allowing for better orbital solutions to be found.

5.3 High Mass Companions and Host Star Interactions

As was the case in DR12, there are a substantial number of systems with relatively high mass companions. Systems with a mass ratio $\langle q \rangle = \frac{(4/\pi) m \sin i}{M_{\star}} > 0.425$ would be expected to manifest themselves as double-lined spectroscopic binaries. As can be seen in Figure 5.5, there are 167 candidate systems in the DR14 catalog with

Table 5.1—Continued

DR14 Exclusion Cause	n	APOGEE_IDs
Best-Fit Orbit Removed From DR14 Gold Sample due to New Criteria		
`BISECTOR_WARN` set	25	2M00293898+6641295, 2M03225614+7935522, 2M03281799+4621291, 2M04302445+5458419, 2M04473998+3846403,2M04481529+3734462, 2M05155531+2319522, 2M05452339+2829265,2M06143169-0043009, 2M06321756+0057557, 2M06472969+0110556, 2M07041952+0409549, 2M08463712+1055189, 2M11450339+0121238, 2M12212053+1352596, 2M13122184+1635340, 2M13474582+1728364, 2M16321854-1347536, 2M16473251+3727163, 2M20564020+5021315, 2M20574795+5015567, 2M21301297+1133164, 2M21325045+1206334, 2M21442136+4312587, 2M21442136+4312587

Table 5.2. Gold Sample Selection Criteria Values for the DR12/DR14 Overlapping Gold Sample

Criteria	DR14 Value	DR12 Value
$\min(\Sigma_{RV}/2.5)$	1.045	1.023
$\min\left(\frac{K/\tilde{\sigma}}{3+3(1-V_N)e}\right)$	1.018	1.007
$\min(n_{iter}/50)$	**0.860**	**0.740**
$\min\left(\frac{K/\lvert\Delta\tilde{v}\rvert}{3+3(1-V_N)e}\right)$	**1.913**	**2.140**
$\min\left(\frac{(K/\tilde{\sigma})/(3+3(1-V_N)e}{\chi^2_{mod}}\right)$	1.031	1.030
$\min\left(\frac{(K/\lvert\Delta\tilde{v}\rvert)/(3+3(1-V_N)e}{\chi^2_{mod}}\right)$	1.043	1.097
$\min\left(\frac{U_N V_N}{0.5}\right)$	1.000	1.003
$\max\left(\frac{P/\Delta T}{2}\right)$	0.977	0.978
$\min\left(\frac{a(1-e)}{R_\star}\right)$	**1.236**	1.047
$\max(e/0.934)$	0.969	0.999

$\langle q \rangle > 0.425$. Of these, 83 are giant stars and 22 are subgiants, where we would not expect the companion to be luminous enough to influence the companion's spectrum. However, the 27 evolved star systems with $\langle q \rangle > 1$ are interesting because their companion would either have already undergone its evolution, making the companion a stellar remnant, or a significant amount of mass transfer has occurred between the companion and the host star. Two of particular interest are 2M00393636+8359378, a $1.16 M_{\odot}$ giant star that has a companion that is $5.69 M_{\odot}$ on a 648-day orbit, and 2M14203191-0554436, a $1.38 M_{\odot}$ subgiant that has a companion that is $3.15 M_{\odot}$ on a 470-day orbit. These are extraordinarily interesting systems because, according to their fitted parameters, their companions would need to be black hole remnants of relatively massive stars, with the current host stars having survived the companions' progenitors' supernova explosion. We note that both systems have second less-preferable solutions that suggest a lower mass companion. These stars are slated to acquire additional epochs in APOGEE-2, so their orbital solution will be revisited when more data are available. Of the remaining 62 main sequence hosts, 18 have $\sigma_{BIS} > 1$ km s^{-1}, indicating a luminous massive companion. The remaining 44 then are potential hosts of white dwarf companions, which includes 20 potential low-mass white dwarfs with $\langle m \rangle < 0.5 M_{\odot}$. In total, this catalog contains 71 potential stellar remnant companions.

It is well established that a short-period massive companion will synchronize its host star. We see evidence of this in Figure 5.6, with nearly all of the hosts of short-period ($P < 20$ days) stellar-mass companion candidates in the DR14 gold sample exhibiting rapid rotation rates. This implies that these companions are spinning up their companion rather than being native rapid rotators, especially since planetary-mass companions in the same period range are largely non-rapid rotators, as can

be seen with the systems in the bottom-left of Figure 5.6. It is interesting to note that of the 96 candidate brown dwarf companions with $P < 100$ day orbits, 40 have hosts with $v \sin i > 6$ km s^{-1}, and 33 are slow-rotating giants and subgiants that likely evolved from F dwarfs that were rapidly-roating throughout their main sequence lifetime. As discussed in Chapter 3, Guillot et al. (2014) suggested that tidal dissipation plays a role in shaping the brown dwarf desert, and the lack of short-period brown dwarfs orbiting G dwarfs can be attributed to the slow-rotation rate ($P_{rot} \sim 30$ days) of these stars, which decreases the timescale of tidal dissipation (which scales as $(1 - P_{orb}/P_{rot})^{-1}$) compared to more-rapidly rotating stars such as F dwarfs (with $P_{rot} \sim 1$ day). The presence of such a large number of rapidly-rotating (or previously rapidly rotating) stars among the short period brown dwarfs is evidence that this effect plays a role in shaping the inner bound of the brown dwarf desert. However, this cannot be a complete explanation for our apparent filling in of the BD desert, because there are 23 slow-rotating dwarfs with candidate BD companions that this effect cannot explain, as well as a substantial number of brown dwarf companions at longer periods for which tidal interaction is not applicable. These issues are probed further in the next section.

5.4 Connecting Occurrence Rates of Companions with their Formation

In this section we investigate the occurrence rate of companions as a function of host star parameters to gain insights into the formation mechanisms of the companions in this catalog.

5.4.1 Determining Companion Occurrence Rates

When calculating occurrence rates of binned data, first we calculate a "raw occurrence rate" of each bin, which is simply

$$f_{raw} = \frac{n_{gold}}{n_{parent}}, \tag{5.12}$$

where n_{gold} and n_{parent} are the number of gold sample and parent sample objects in a given bin. Uncertainties for the raw rates in each bin are calculated using propagation of error on Poisson ($\sigma/n \sim n^{-0.5}$) statistics:

$$\sigma_{raw} = \frac{n_{gold}}{n_{parent}} \sqrt{n_{gold}^{-1} + n_{parent}^{-1}}. \tag{5.13}$$

We call these "raw" because we must consider how detection efficiency affects the calculation.

To calculate detection efficiency, ϵ, for a bin, we employ the suite of simulated systems described in §2.5. In, particular, we adopt similar methods that produced recovery rates as a function of n_{RV} and $m \sin i$ from Figure 2.8. This simulated suite was passed through the orbit fitting portion of the `apOrbit` pipeline simulating 9, 12, 16, and 24 epochs of observations. For each bin, we use the results that corresponds closest to the median number of visits to parent sample stars in the bin. We trim the selected simulated suite so that it matches systems under consideration. For example, if a bin was only considering Brown Dwarfs within the orbit of the Earth, then the simulated suite would only include systems with $13 M_{Jup} < m \sin i < 80 M_{Jup}$, and $a < 1$ AU. The orbit fitting results from the trimmed simulated suite are passed through the DR14 gold sample selection criteria using the median velocity uncertainty, $\tilde{v}_{unc}$ of parent sample stars in the bin when a velocity uncertainty value is needed.

The detection efficiency is then calculated

$$\epsilon = \frac{n_{gold}^{sim}}{n_{parent}^{sim}} \tag{5.14}$$

where n_{parent}^{sim} is the number of simulated systems in the trimmed simulated suite, and n_{gold}^{sim} are the number of those simulated systems which satisfy the DR14 gold sample criteria using $\tilde{v}_{unc}$. The uncertainty of ϵ is calculated in a similar manner as f_{raw}:

$$\sigma_\epsilon = \epsilon \sqrt{(n_{gold}^{sim})^{-1} + (n_{parent}^{sim})^{-1}}. \tag{5.15}$$

An example of these correction factors are shown in Figure 5.7.

The raw occurrence rate is then divided by this correction factor to get a corrected occurrence rate:

$$f = \frac{f_{raw}}{\epsilon}, \tag{5.16}$$

with uncertainty:

$$\sigma_f = f \sqrt{\left(\frac{\sigma_\epsilon}{\epsilon}\right)^2 + \left(\frac{\sigma_{raw}}{f_{raw}}\right)^2}. \tag{5.17}$$

5.4.2 The Role of Host Stellar Type

It is known that the stellar multiplicity rate varies by stellar type with multiplicity increasing towards earlier spectral types (Duchêne & Kraus 2013). We wished to verify this result with this sample, and determine the occurrence rate of brown dwarfs as a function of stellar type. To perform this analysis, gold sample systems were binned by primary mass, and the occurrence rate calculations were performed as described in the previous section. In both this section and the next, we focus on main sequence stars because we are interested in the formation mechanisms and these systems will

be closer to their birth configuration. Furthermore the masses for the dwarfs in our sample are derived in a more uniform manner than for the giants, and we also wish to match our results to previous samples, which typically are exclusively dwarfs. A more complete analysis including the evolved stars in our sample will be undertaken at a later date.

The results of this analysis is shown in Figure 5.8. The occurrence rates of stellar mass companions around dwarf stars in this sample (blue points in this figure) increases with host star mass which is in general agreement with Duchêne & Kraus (2013). The occurrence rates of brown dwarf companions (red points in Fig. 5.8) seem to follow a fundamentally different trend, with brown dwarf occurrence rates decreasing with stellar mass, reaching a minimum around $1.0 - 1.2 M_{\odot}$ before a slight upturn at higher masses. Damiani & Díaz (2016) predicted a similar result from their modeling of massive substellar companions orbiting convective stars. However, their arguments stemmed from tidal decay, which would only effect companions with $P < 30$ days, while the majority of BD companions around main sequence stars in this catalog are orbiting at $P > 30$ days, with some at $P > 1000$ days. This suggests that tidal decay is likely not driving this trend, and that something applicable to companions at all periods, such as the formation mechanism of the companion, is at work here. We discuss this further in the next section.

5.4.3 Revisiting the Planet-Metallicity Correlation

As discussed in §1.1.2, giant planets formed by core accretion should follow the planet-metallicty correlation (PMC). While the general consensus has been that brown dwarfs form like stars, recent work has shown that core accretion may be able to form companions up to 38 M_{Jup} (Mordasini et al. 2009). Determining the metallicity

trend of the substellar companion hosts compared to the known PMC could shed some light on this debate. To accomplish this, we binned both the gold sample orbits and the APOGEE parent sample by metallicity ([Fe/H]), and used the procedure described above to determine binary, BD, and planet occurrence rates in each bin. We compare these occurance rates to the form of the PMC from Fischer & Valenti (2005):

$$\mathcal{P}(\text{planet}) = 0.03 \times 10^{2[Fe/H]}, \tag{5.18}$$

which is the probability of an FGK dwarf star forming a gas giant planet with $P < 4$ years.

In Figure 5.9, we present the results of this analysis on the dwarf and giant hosts in the DR14 gold sample. Unfortunately, planetary-mass companions ($\frac{4}{\pi} m \sin i \leq 13 M_{Jup}$) are not numerous enough in this catalog to perform meaningful statistical analysis. However, we will note that the overall lower occurrence rate for planetary mass companions for giants is due to the inability to probe the shortest orbital periods accessible to dwarfs. Also the lower occurrence rates of binary companions around dwarf stars compared to giants is likely due to the exclusion of strong SB2s in the gold sample, which would select against near equal-mass binaries for dwarf stars, while allowing inclusion of similar systems for giants. Furthermore, the interpretation of the trends for the giants stars is less clear than for the dwarfs, so we will focus on the latter for the remainder of this section.

The brown dwarf occurrence rate generally decreases with [Fe/H], reaching minimum around solar metallicity for dwarf hosts. Above solar metallicity, the BD occurrence rate increases, and is fit well by a form of the PMC that has a weaker dependence on [Fe/H]: $\mathcal{P}(\text{planet}) = 0.03 \times 10^{[Fe/H]}$. This trend could imply that core accretion plays a role in the formation of brown dwarf companions for high metallicity

host stars, but at lower metallicities, brown dwarf companions are more likely to be formed via disk instability. This is supported by the conclusiions of Maldonado & Villaver (2017), who found that low-mass BD companions ($m < 42.5 M_{Jup}$ in their work) had a tendency of having slightly higher metallicity than non-hosts and stars hosting more massive brown dwarfs. Our data also supports their conclusion that the core accretion mechanism becomes efficient in the formation of low-mass brown dwarfs at high metallicities, while gravitational instability is the preferred method in turbulent protostellar discs at lower metallicities.

The results in Figure 5.9 also suggest that disk instability is metallicity dependent as we also see in our catalog that the occurrence rate of stellar-mass companions, for which disk instability is the most plausible formation mechanism, decreases with metallicity. Tanaka & Omukai (2014) calculated disk structures at a variety of metallicities, and found that lower metallicity protostellar disks become Toomre unstable due to less efficient cooling, increasing the likelihood of fragmentation and binary formation. If we follow this interpretation, disk instability is more efficient in general than is core accretion at forming brown dwarf companions (i.e. the occurrence rate for BDs around sub-solar metallicity hosts is higher than that for BD companions around hosts of higher metallicity.).

It is also interesting to note that the discrepancy in occurrence rate between binaries and brown dwarfs around dwarf hosts reaches a maximum around solar metallicities. This finding combined with the result from the previous section would explain why we would observe a brown dwarf desert for approximately solar mass stars having around solar metallicity, but not for other types of stars.

5.5 Conclusions

Using APOGEE-2 DR14 data and refined candidate selection criteria, we produced a gold sample sample of 699 companion candidates from a parent sample of $\sim 15,000$ stars having multi-epoch RV data and spanning a wide range of spectral types and evolutionary states. Using this catalog we found:

- A highly truncated brown dwarf desert, consistent with our results from Chapter 3(Troup et al. 2016), despite the retraction of number of the DR12 candidate systems after this reanalysis with DR14 data.
- A total of 71 candidate systems with potential stellar remnant (white dwarf, neutron star or black hole) companions, including two possible black hole companions and 16 potential low-mass white dwarfs.
- Clear evidence that short-period binary companions are spinning up their host stars.
- Evidence that tidal dissipation plays a role in shaping the brown dwarf desert in the $P < 100$ days regime. However, this mechanism cannot explain all of the brown dwarfs in the DR14 sample.
- Brown dwarf companions may have two formation pathways, with higher metallicity hosts forming BD companions via core accretion and lower metallicity host employing via disk, and with disk instability overall being the more efficient mechanism.
- BD occurrence rates around main sequence stars reaching a minimum around solar mass and metallicity may explain why previous studies have found a Brown

Dwarf Desert, while the present analysis of the APOGEE catalog lacks such a feature.

We can expect continued improvement in our understanding of all these phenomena just from the APGOEE project alone. In addition to the planned dedicated fields for this purpose described in the next chapter, we expect many additional APOGEE-2 fields will have companion candidates discovered serendipitously, as was the case in the work described in the previous chapters. In APOGEE-1, $\sim 10\%$ of the targeted stars had ≥ 8 visits, and of those, $\sim 2.6\%$, or a cumulative $\sim 0.26\%$ of all survey stars, were selected as having companion candidates. APOGEE-2 will bring the cumulative total number of stars observed by the APOGEE instrument to $\sim$500,000 stars. Therefore, assuming a similar detection rate and visit distribution, as well as the "gold sample" selection criterion used here, we expect to detect a cumulative total of at least 1300 companion candidates by the end of APOGEE-2. Furthermore, the next data release of APOGEE-2 will include the first data from the Southern Hemisphere, which will bring probes of multiplicity in exciting new environments such as the Magellanic Clouds, a variety of dSphs, and the Galactic bulge.

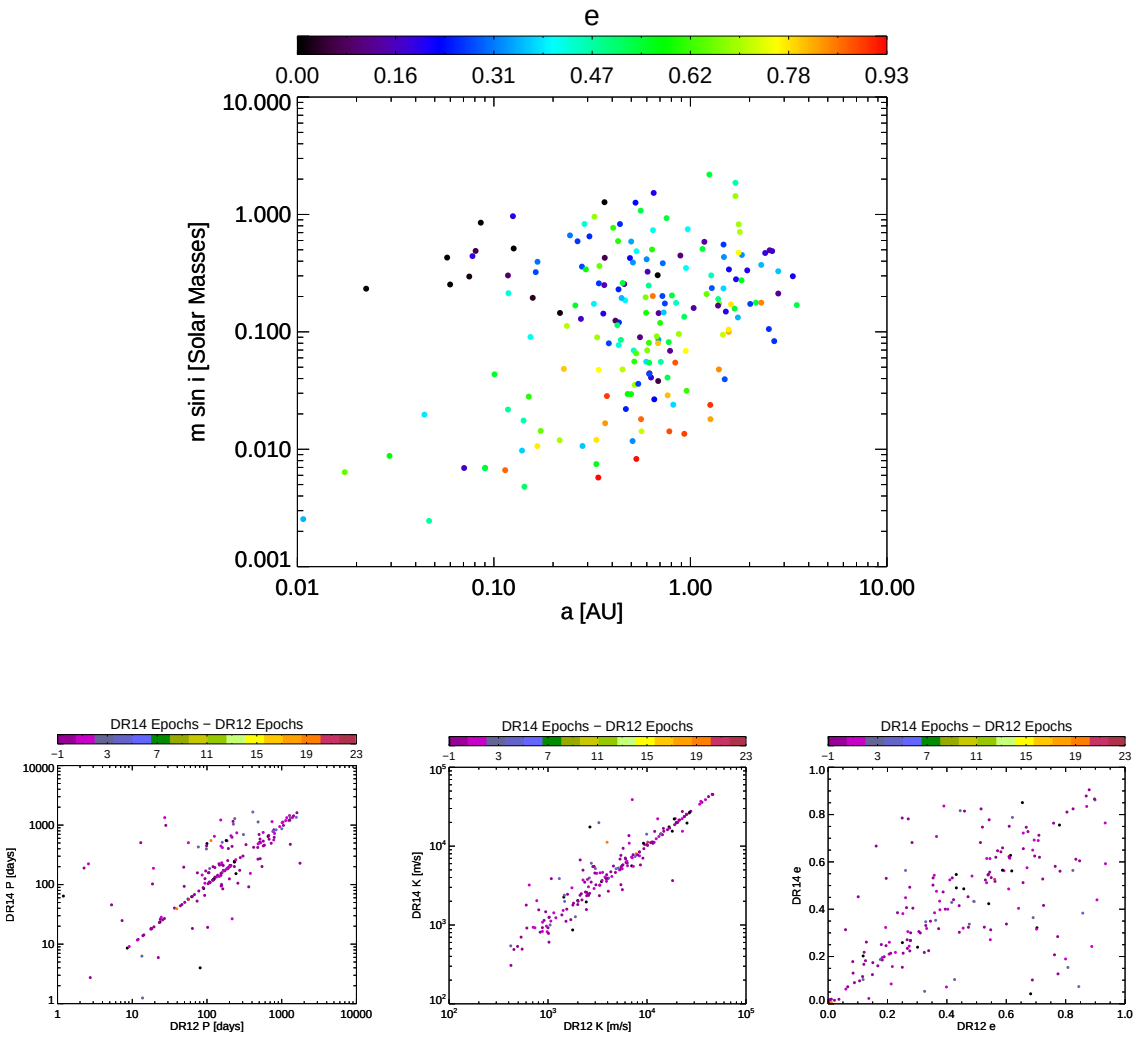

Fig. 5.3.— *Top Panel:* Orbital distribution of the 188 systems in common between the DR12 and the DR14 gold samples. Compare to Figure 3.1. *Bottom Panels:* Comparison between the derived period (*left*), semi-amplitude (*center*), and eccentricity (*right*) in the DR12 catalog versus the DR14 gold sample, with color indicating the difference in number of APOGEE visits for which data are reduced between the two DRs.

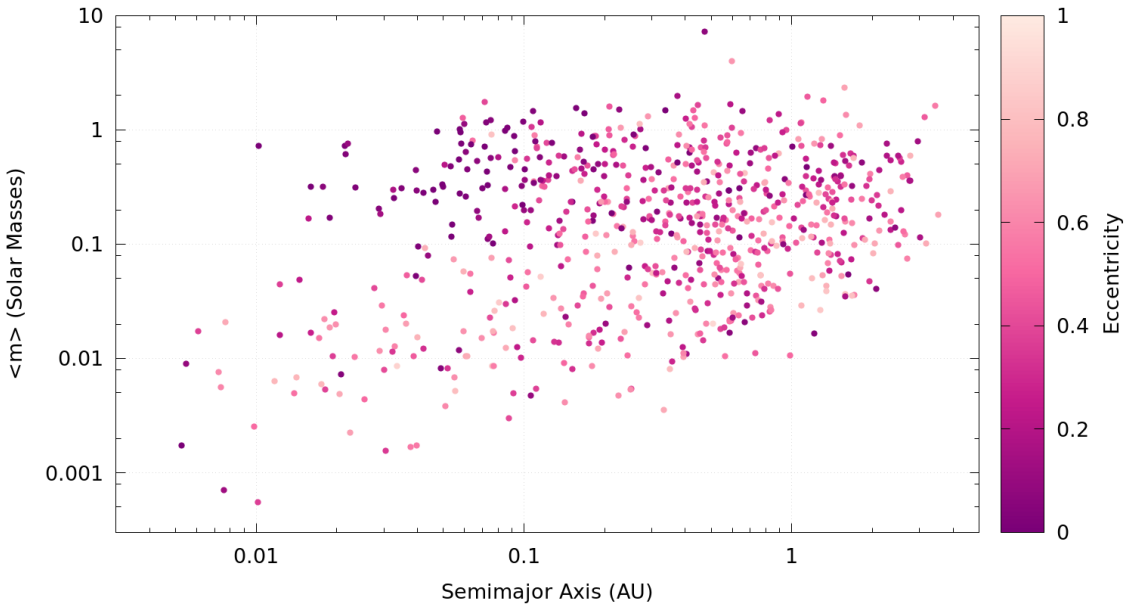

Fig. 5.4.— Distribution of orbital parameters in the DR14 gold sample of companion candidates. The vertical axis is the most likely companion mass ($\langle m \rangle = (4/\pi) m \sin i$) in $M_\odot$, the horizontal axis shows the orbits semimajor axis (a) in AU. Color indicates the eccentricity (e) of the orbit, with the darkest shades indicating circular orbits.

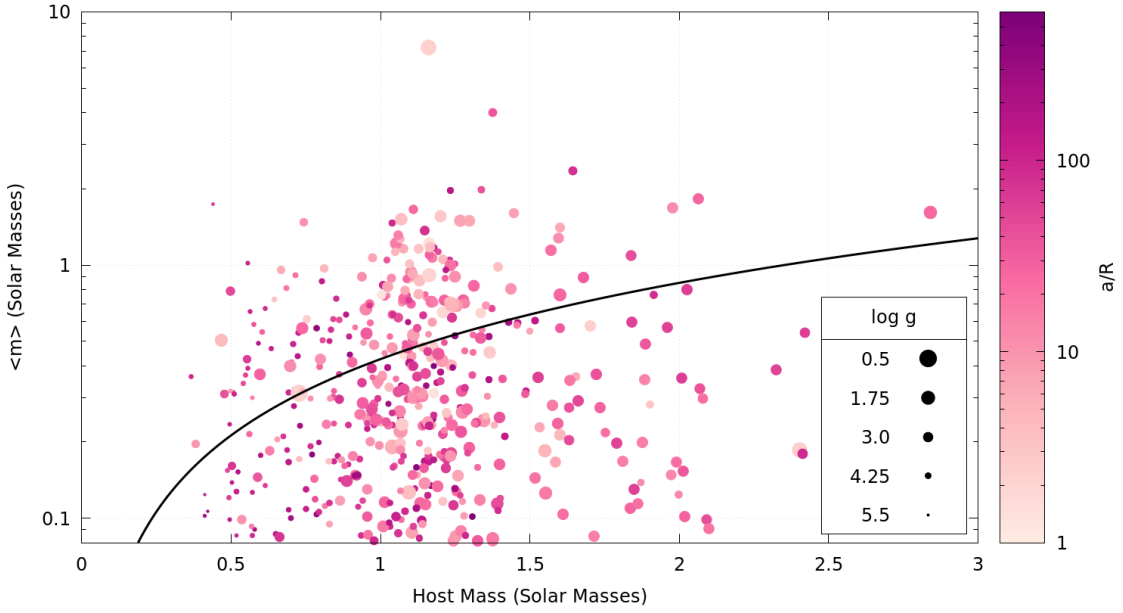

Fig. 5.5.— Candidate systems in the DR14 gold sample with a stellar-mass companion. The horizontal and vertical axes are the host mass and companion mass, respectively, with the black line marking $\langle q \rangle = \frac{(4/\pi) m \sin i}{M_\star} = 0.425$. Point size represents the host star's $\log g$, and color indicates how many stellar radii at which the candidate companion is orbiting.

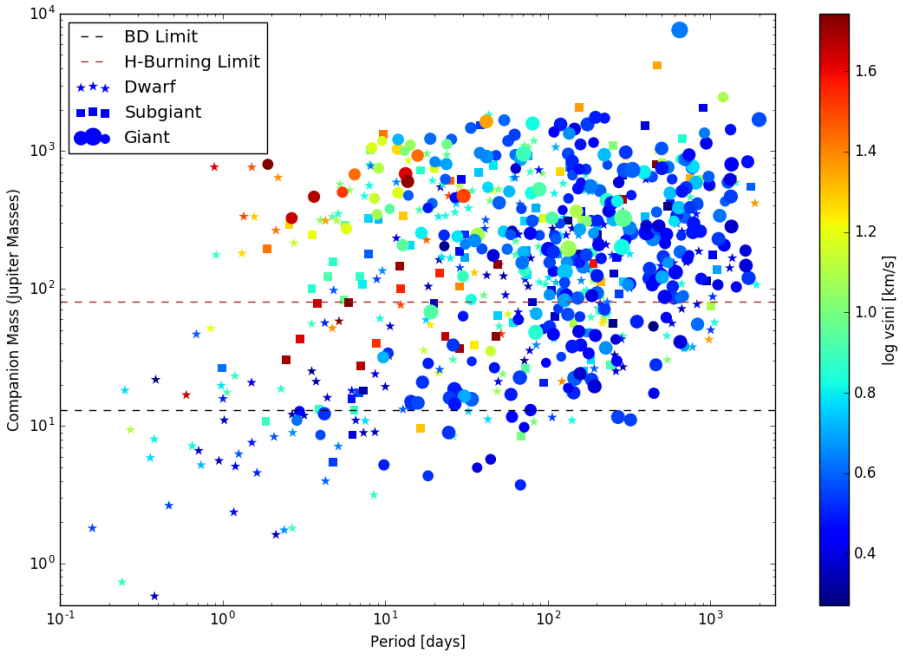

Fig. 5.6.— Similar to Figure 5.4, but with orbital period on the horizontal axis, and symbols color-coded by the logarithm of the rotational velocity. The vertical axis is an inclination-corrected maximum likelihood mass ($\frac{4}{\pi} m \sin i$) in Jupiter Masses. Symbol shapes indicate evolutionary stage of the host star.

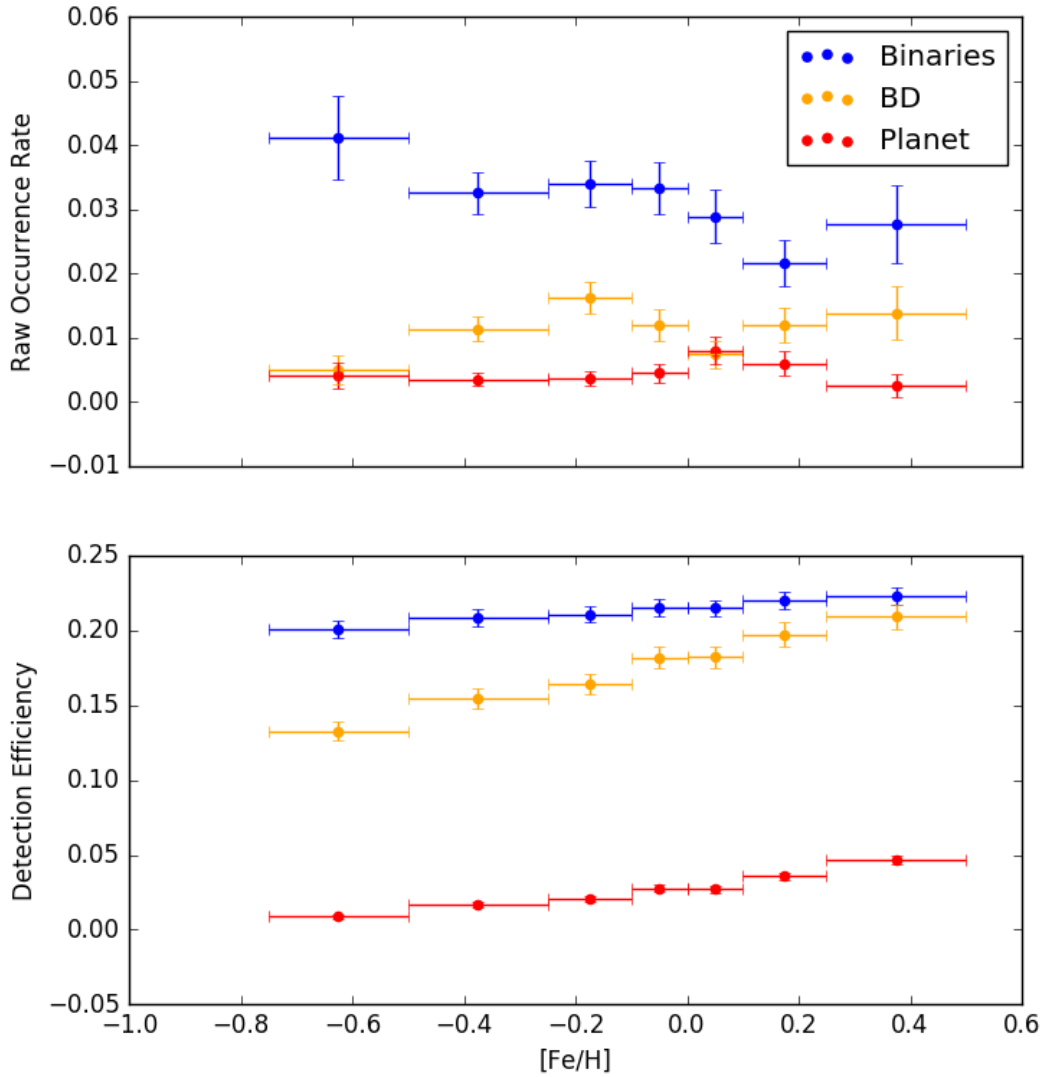

Fig. 5.7.— *Top Panel:* Raw occurrence rates (f_{raw}) of binaries (blue), brown dwarfs (red), and gas giant planets (black) as a function of host star metallicity The horizontal error bars are the bin sizes, and the vertical error bars were calculated by propagating Poisson statistics as described in the text. *Bottom Panel:* Detection efficiencies as a function of metallicity calculated using the methods in the text.

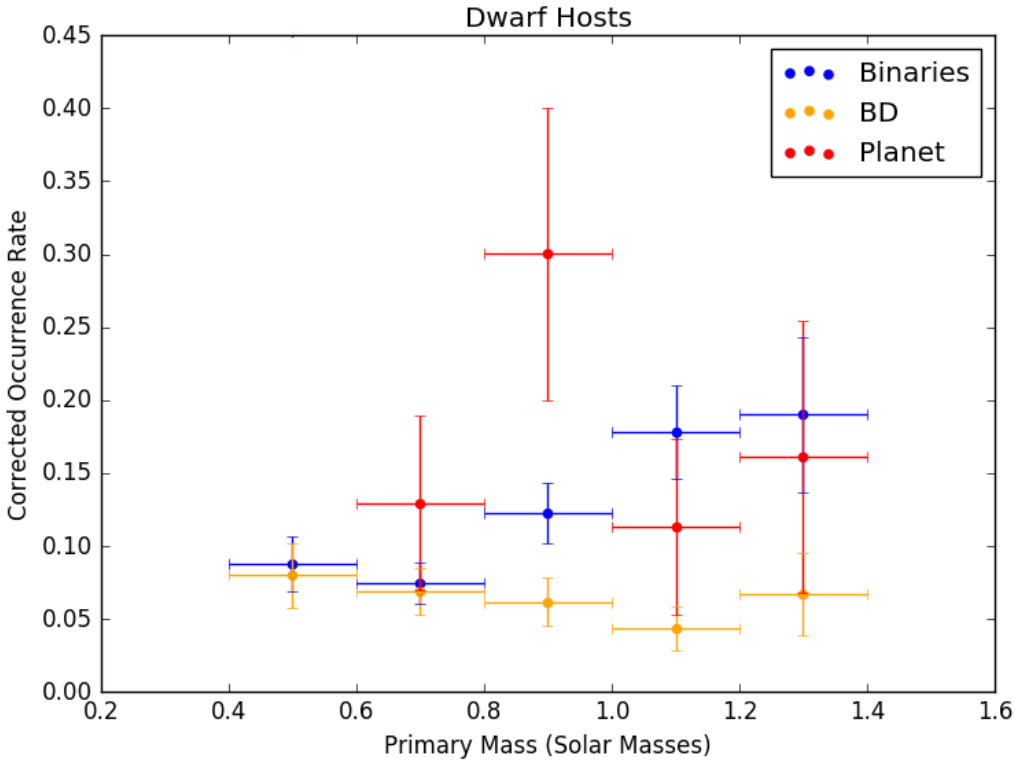

Fig. 5.8.— Corrected companion occurrence rates of main sequence stars in the DR14 gold sample as a function of host mass. The colors and horizontal error bars are the same as in Fig. 5.7. The vertical error bars are σ_f, whose calculation is described in the text.

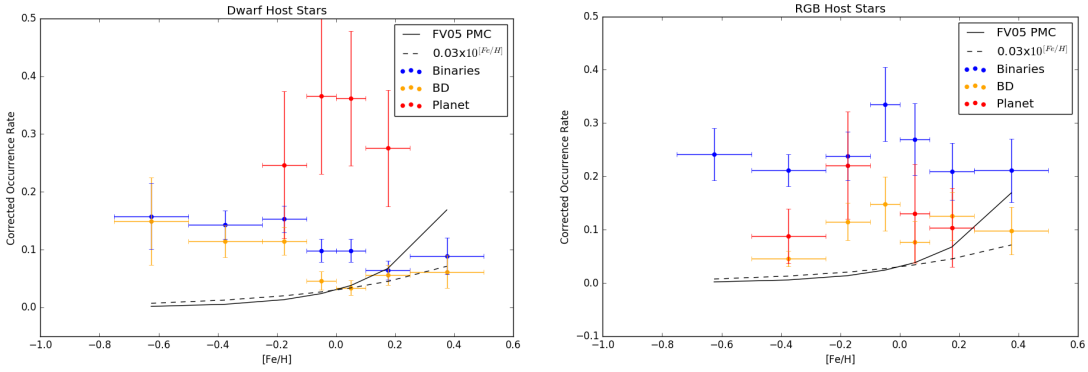

Fig. 5.9.— Same as Figure 5.8, but binned by host star metallicity. The solid line is the form of the planet-metallicity correlation (PMC) from Fischer & Valenti (2005) (FV05), and the dotted line is a similar form, but with a weaker dependence on [Fe/H]. The left and right panels are the results for dwarfs and giants respectively.

Chapter 6

Ongoing Follow-up Efforts and Future Survey Planning

In this chapter, I outline our ongoing program and plan for external monitoring of our candidate companion systems with the primary goals of false-positive testing and more accurate characterization of each system (§6.1). I also describe the target selection and observing strategy of the APOGEE-2 substellar companion goal science program (§6.2), which was motivated by the results from APOGEE-1 as described in Chapter 3. Finally, I present our proposed survey for inclusion in the successor to SDSS-IV (§6.3).

6.1 External Monitoring and Follow-up Data

A large fraction of our catalog is companion *candidates* in need of further vetting with additional observations to (1) rule out false positive signals, and (2) better constrain fitted orbits. We have ongoing observational programs to investigate individually the best planetary mass and BD systems in this catalog that include high-resolution

optical spectroscopy, diffraction-limited imaging, and photometric variability monitoring. Our overall strategy for these observations has been to use relatively inexpensive and/or non-competitive resources readily available to our group to build a high-priority follow-up sample free of obvious false-positives before requesting more precious telescope resources such as high-cadence high (~ 1 m s^{-1}) precision RV observations on more competitive and expensive platforms such as the High Accuracy Radial velocity Planet Searcher (HARPS) on the La Silla telescope, the High Resolution Spectrograph (HRS) or Habitable Zone Planet Finder (HPF) on the Hobby-Eberly Telescope (HET), or the soon-to-be publicly available NEID spectrograph on the WIYN telescope (See §7.2).

6.1.1 High-Resolution Optical Spectroscopy

We are collecting complementary high-resolution optical spectroscopy to rule out potential sources of false positive signals, and obtain additional RV epochs when possible. One potential source of false-positive RV signals is stellar chromospheric activity. We require *optical* spectroscopy because the strongest proxies for this activity are emission in Hα (6563Å) and Ca II H&K (3968.5Å and 3933.7Å, respectively). Furthermore, high-resolution optical spectra also provides access to lithium abundances, which provide a useful signpost of planetary engulfment (e.g., Carlberg et al. 2012).

For APOGEE fields with a high density of targets, we have employed Hectochelle (Szentgyorgyi et al. 2011) on the 6.5-m MMT, a high-resolution ($R \sim 32,000$), multi-object (240 fiber), queue-scheduled echelle spectrograph with demonstrated RV precision similar to APOGEE when employing the RV31 filter (specifically designed for precision RV work). We prioritized APOGEE-1 fields with many DR12 gold-sample

targets and that will get continued monitoring in APOGEE-2. Because chromospheric activity is most common among young stars, and is less common among giants, we focused our efforts on the APOGEE-1 fields containing the young cluster IC 348 and the open clusters NGC 188 and M67, both which contain a large population of dwarfs surveyed by APOGEE. We requested two epochs of observations using the Ca41 and RV31 filters[1], which give us access to the region surrounding the Ca H&K lines and a region with many narrow lines suitable for precision RV work, respectively. This will allow us to determine if the star's activity level is correlated with its radial velocity variations.

In each field, we prioritized targets with DR12 gold sample orbits, RV variable objects, and objects identified as SB2s. The remainder of the fibers were filled with additional APOGEE targets, which may prove useful if APOGEE-2 uncovers long-term RV variability in these stars. Unfortunately, Hectochelle's field of view is much smaller than APOGEE's (one degree in diameter vs. three), so one or two Hectochelle fields were created for each APOGEE field in the locations with the highest density of priority targets. For gold sample targets that did not lie in a region dense enough to justify a Hectochelle pointing, we employed the single-object ARCES echelle spectrograph on the ARC 3.5-m.

Initial analysis of the Hectochelle data from NGC 188 by UVa undergraduate Duy Nguyen has shown that only five stars out of 84 analyzed exhibited significant Ca II emission. Of these five, only one (2M00344509+851205) was a DR12 gold sample star. Curiously, this star is a 1.2 $M_{\odot}$ G subgiant, a star that one would not typically expect to have strong activity. However, its best fit orbit indicates an orbiting M dwarf companion, so it is possible the observed emission is from the companion rather than

[1]Hectochelle employs filters that select a single order from each star's full echelle spectrum so that the spectral region of interest from multiple stars can be recorded on the same detector.

the host star. More careful analyses of these spectra would be required to confirm this. In any case, this initial analysis suggests that stellar activity is not a prevalent false-positive signal in our catalog, affecting $< 6\%$ of stars. However, we will continue this analysis on a star-by-star basis, and continue to collect observations as systems are uncovered in DR14.

6.1.2 Diffraction-Limited Imaging

For a variety of reasons, diffraction-limited imaging plays a key role in the follow-up efforts of our companion candidates:

1. It allows a search for previously unresolved background/foreground stars affecting the RV measurements or transit signals of our candidates.

2. For nearby candidates, direct imaging can test and clarify the derived orbital parameters for RV-detected companions, either directly though imaging of the detected companion or through detection of other companions in (moderately) longer orbits.

3. The presence of a longer-period companion could potentially affect the RV data, and thus the orbital interpretation, of RV-detected companion candidates. In particular, we can investigate candidate lower-mass companions to ensure they are not face-on binaries masquerading as a short-period planet.

4. Although many of our targets will be too distant to allow direct imaging of RV-detected companions, or additional companions affecting derived orbital solutions, searching for widely-separated companions (even on 1000 AU scales) to stars with short-period companions still contributes to a primary science goal of investigating higher-order multiplicity and the Kozai Mechanism (see §1.2.3).

As giant-giant binaries are exceedingly rare, we focused our efforts in this area on the subgiant and dwarf stars in the DR12 gold sample. We also prioritized our targets by distance, as the closest targets allow us to detect companions at the smallest physical separations. For the faintest targets ($H > 12$), we would need to pursue AO options on large telescopes to accomplish these tasks, but many of our targets can be done much more cost-effectively through speckle interferometry on a modest-sized telescope. We acquired simultaneous R and I band speckle observations of a dozen targets using the Differential Speckle Survey Camera (Howell et al. 2011, DSSI), a duel-channel speckle imager on the WIYN 3.5-m, Of these, only one (2M03432820+3201591) showed clear indication of a binary companion.We also performed pilot observations with LMIRCam on the LBT, observing four $H > 13$ targets in H and, if the H observations showed evidence of a binary companion, K band as well. Of these four, one target (2M04473998+3846403) showed evidence of a binary companion. A more thorough analysis of these data will be undertaken in the future, as well as additional follow-up data of the new companions uncovered in the DR14 catalog.

6.2 The APOGEE-2 Substellar Companion Search Goal Science Program

The results described in the previous chapters were largely derived from serendipitous discoveries of APOGEE main survey targets. Unfortunately, the cohorting scheme APOGEE employs in its main survey fields results in bright stars (i.e., those most conducive to detecting the lowest-mass companions) receiving the fewest epochs, limiting the potential yield of detected companions. To increase this yield, particularly

for low-mass companions, a dedicated search for substellar companions was approved as a goal science program in APOGEE-2, where targets and observing plans are optimized for companion detection. Furthermore, unlike most other RV surveys, APOGEE's multiplexing capability allows us to continue monitoring all targets in a field in a uniform manner. This is important to us because statistical analyses to understand the factors influencing multiplicity requires a sample of stellar targets with a relatively simple targeting strategy that is not dependent on a star's "RV interest."

6.2.1 Approved Observing Program

To maximize the temporal baseline of this program, three disk fields with observations from APOGEE-1 (see Table 6.1) were selected in the under-subscribed 22h<RA<6h region based on the number of bright ($H < 12.2$) giants in the field with >3 epochs observed in APOGEE-1. A secondary consideration was to sample the widest range of environments as possible. These three fields probe stars in the subsolar metallicity environments of the outer disk. To further add to the diversity of environments studied, the open cluster NGC 188 was chosen to provide a sample for which stellar mass and age are known, and in which potential abundance signatures in host stars can be tested against non-host stars of similar chemistry. The field COROTA2-RV includes stars with asteroseismically determined masses from COROT (Bordé et al. 2003), which decreases the uncertainty in the mass of the companions. The evolutionary stage information also allows discrimination between first-ascent red giant and red clump stars, to study the process of tidal engulfment of planets on the RGB.

These fields will be observed in APOGEE-2 between 11 and 24 times, to reach a final count of 24 epochs for all stars in the field, which simulations and experience

have shown to be the minimum amount required for well-constrained Keplerian orbits (Kane et al. 2007a,b). The visits are cadenced such that the RVs are sensitive to companions with a range of periods from a few days to nearly a decade (the temporal baseline of the observations). Within each field, the stars are selected from those targeted by APOGEE-1, prioritized first by the number of APOGEE-1 epochs, and then by the stars' H magnitude with bright stars receiving higher priority. Telluric calibration stars are also repeated from APOGEE-1, and prioritized in the same manner as, but ranked separatelt from, the science targets. By the end of APOGEE-2 in 2020, we will have acquired $\geq$ 24 epochs of RV measurements over a nine-year baseline of 1074 red giant stars across these five fields.

6.2.2 APOGEE-2 Bright-Time Extension

A streak of remarkably good weather and improved observing procedures resulted in the APOGEE-2 survey operating at nearly 150% efficiency in its first two years. Because of this, the survey is projected to run out of available plates as early as the Summer of 2018. To fill this time, goal science programs were prompted to submit possible expansions to their program proportional to their program's original allocation. For the substellar companions program, this equated to 50-100 field visits depending on precisely how much open time there will be. Our highest priority fields to fill this time are listed in Table 6.1. As before, we chose APOGEE-1 fields that have already already amassed a substantial number of visits ($>$ 8) to substantially increase the sampled temporal baseline and sensitivity to companions.

Our current goal science fields restrict us to the outer Galaxy ($120^\circ < l < 240^\circ$), largely due to restrictions on the available LST ranges for goal science programs. In particular, all of our current disk fields lie in the 2nd Galactic quadrant, so three

APOGEE-1 disk fields at $l = 30, 60, 90°$ and $b = 0$ were chosen to expand our program's disk coverage. In addition, we aim to include stars in a variety of *cluster* environments with a wide range of ages, metallicities, and densities to determine what role environment has to play in the formation and evolution of stellar systems containing companions of various masses. With the ever-growing sample of companions (both stellar and substellar) being discovered around stars from ever more diverse environments, population studies comparing host environments are now becoming possible. For example, recent work suggests the hot Jupiter occurrence rate in M67 is higher than in the field (Brucalassi et al. 2016), although it is not clear whether this is the norm for open clusters generally.

For the substellar goal science expansion we have chosen several APOGEE-1 fields containing open clusters, globular clusters, and young embedded clusters (see Table 6.1). Here we outline the clusters chosen for this expansion. M67, a "solar analog" (solar metallicity and age) open cluster with known substellar companions (Brucalassi et al. 2014), was chosen to act as the "lynchpin" for our comparisons. These observations combined with those of NGC 188, an older (6.8 Gyr) open cluster of similar metallcity, will allow us to probe binary parameter distributions as a function of age in open cluster environments. Furthermore, M67 is in the K2 campaign 5 and 16 fields, which provides synergistic opportunities with programs seeking asteroseismology and transit follow-up. M3 is an older (11.4 Gyr) relatively metal-rich ([Fe/H]=-1.3) globular cluster, increasing the likelihood of detecting substellar companions compared to other more metal-poor globular clusters. This program will make APOGEE one of the few surveys (if not only survey) with long-term precision RV monitoring of distant globular clusters. Individually, each cluster allows a measurement of the binary fraction distribution across the cluster to compare to expectations from dynamical

evolution models. Of course, finding *substellar* companions in globular clusters would also be a unique and exciting discovery, because these represent very old and fundamentally different stellar populations from the open clusters above.

Most importantly, our expanded field lists include a selection of APOGEE-1 fields that contain young embedded clusters at a variety of ages (1 - 10 Myr). These fields are well-suited for study with APOGEE's wide-field infrared capability, and will allow us to investigate systems with companions at the critical earliest stages of evolution. The brown-dwarf eclipsing binary discovered in the Orion cluster (Stassun et al. 2006, 2007) remains the only known system of this kind in the literature and thus serves as a singular empirical benchmark for the fundamental properties of substellar objects at young ages. Finding additional brown dwarf companions in a young open cluster is the type of fundamental discovery that would be enabled by the expansion of this program. The discovery of just a few systems with brown dwarfs and hot Jupiters in this environment would allow the following questions regarding systems with substellar companions to be addressed: (1) How quickly do hot Jupiter systems form, and do they form in situ or by migration? (2) What is the occurrence and orbital distribution of close-in brown dwarfs compared to those in older systems, such as the open clusters we plan to observe, and what can that tell us about the origin and evolution of the "brown dwarf desert?" Clusters are also enticing targets for tackling during SDSS-IV because the planned robotic fiber positioner for the successor survey to SDSS-IV (see §6.3) will have a greater fiber collision radius than the plug plates currently employed, and thus targeting in these crowded fields will become even more difficult.

Finally, the Sgr dSph is a tantalizing target for "extragalactic" companion hunting due to its relative proximity and metal-rich populations, as discussed in Section 1.2.2.

Overall, the above proposed expansion will greatly enhance the impact of the current substellar companions goal science program, as well as allow us to acquire advance observations that will relieve some of the observing burden from the successor survey to SDSS-IV and fill in the temporal baseline between these fields' APOGEE-1 observations and any potential "After-SDSS-IV" observations (see §6.3).

6.3 Planning for After Sloan 4: The APOGEE Time-Domain Legacy Survey

In 2016, planning for After Sloan 4 (AS4) surveys began in earnest with a call for proposals for science programs employing the Sloan and LCO 2.5m telescopes and associated Sloan instruments starting in 2020. Though the original APOGEE observing strategy was not designed for efficient companion finding (aside from the cadence strategy to weed out the binaries with the largest RV signatures), in this dissertation we demonstrated the capacity of the system for discovering and characterizing even *substellar* companions. Thus, with better optimization directed towards this goal (see §6.3.4 below), the APOGEE spectrographs make possible the contemplation of the first Galaxy-wide survey for stellar and substellar companions, and are poised to reap a much larger scientific harvest in the study of the occurrence rate, formation, and evolution of star systems with stellar and substellar companions throughout the Galaxy with a comprehensive, stellar populations approach. It was with this motivation that we proposed the APOGEE Time-Domain Legacy Survey (ATLaS) as a flagship AS4 program. I played a major role in defining the proposed ATLaS program. In this section, we present this survey *as proposed* to the AS4 steering committee (SC). In the final subsection (§6.3.6), we discuss the SC response to our proposal and the path

Table 6.1. APOGEE-2 Substellar Companion Goal Science Fields

Field Name	APOGEE-1	APOGEE-2	Total Epochs
Approved Goal Science Fields			
120-08	3-6	22	25
150-08	3-5	22	25
180-08	3-4	21	24
COROTA2	1	24	25
N188	9	11[a]	20
Candidate Fields for Open Year 5/6 Time			
IC348	3-16	8-16[b]	19-24
N1333	3-6	18	21-24
203+04 (N2264)	3-6	18	21-24
ORIONA	3-8	16	19-24
ORIONB	1-6	18	19-24
M67	3-22	3-12[b]	15-25
M3	9-24	3-12[b]	21-27
SGR1	3-12	12	15-24
030+00	6-24	3-12[b]	18-27
060+00	6-24	3-12[b]	18-27
090+00	6-24	3-12[b]	18-27

[a]N188 will also be observed over 12 additional epochs in APOGEE-2 for calibration purposes, but not necessarily with all of the same targets.

[b]These fields would require multiple designs.

of this survey going forward.

6.3.1 Detailed Description of Proposed ATLaS Components

As proposed, ATLaS would be the first comprehensive, large-scale, time-domain stellar spectroscopic survey across many host populations, evolutionary states, and Galactic environments. This is all made possible through the continued use of the APOGEE spectrographs in both hemispheres with modest improvements (see §6.3.2) to achieve radial velocity (RV) precisions of $\sim$ 30 m s^{-1}. ATLaS will leverage the multiplexing capabilities of APOGEE to overcome some of the observational biases that have hindered efforts to uncover the role that different environmental factors play in the formation and evolution of stellar systems. For example, most companion detection techniques tend to be most sensitive to the largest companions, the brightest hosts and to either extreme of the separation distribution. At the low mass end, the excitement of pushing to find Earth-like planets combined with the expense of following up systems incentivizes the pursuit of the "most interesting" at the expense of understanding the larger context of the commonplace. In contrast, the ATLaS survey was designed to minimize such biases by observing all targets homogeneously regardless of the presence of a companion, which is something only multi-object instruments can reasonably achieve. These targets would be complemented by speckle interferometry to probe wider separation companions (P3). Finally, ATLaS aims to provide high impact spectroscopic characterization of a complementary sample of planet hosts identified by major planet hunting surveys, as well as astrometric binaries discovered by Gaia (P2). Here we give a detailed description of the goals of these three complementary observing programs that were put forward in the ATLaS proposal.

Program 1 (P1): A Long Baseline Time Domain RV Companion Search

ATLaS P1 would be the most comprehensive, farthest-probing, pan-Galactic stellar multiplicity survey for the foreseeable future sensitive to companions with short and intermediate periods, complementing the wide separations probed by the astrometric method of Gaia. ATLaS Program 1 is built on the data legacy of the APOGEE-1 and 2 surveys and aims to revisit up to 100,000 stars in ∼200 fields. By 2020, these APOGEE-1 and -2 fields will have been observed from 6 to 24 epochs, meaning as few as six additional epochs to these fields in AS4 would provide sufficient phase coverage to extend temporal baselines up to 15 years. ATLaS P1 would continue the observational strategy implemented in the APOGEE-2 substellar companion goal science program to achieve homogeneous coverage of multiple and solitary stars rather than the "target of interest" approach of most RV surveys. P1 plans to observe some of the most unique targets in regions of the Galaxy rarely explored by stellar companion surveys (see §6.3.5). Planned ATLaS P1 targets include giants, subgiants, hot dwarfs and young stellar objects (YSOs), and would also exploit previous APOGEE observations of star clusters and Galactic satellites, breaking the traditional focus on nearby, Sun-like field stars. Our sample of giant stars will include both first ascent RGB stars and core He-burning stars (which have already passed through the RGB tip phase), giving valuable insight on the survival and engulfment of planets, as discussed in Section 1.2.1.

Another primary goal of ATLaS P1 is sensitivity to brown dwarf mass companions at all periods obtainable by this survey (i.e., $P < 15$ years). Achievement of this goal would require improvement of the RV precision of 100 m s^{-1} achieved by the current APOGEE pipeline. Some recent adjustments to the RV code have brought down the RV uncertainties slightly (see §4.2), but we believe that further improvements to the

pipeline can improve the RV measurements from the legacy APOGEE-1 and 2 data to $\sim$ 50 m s^{-1} (see §6.3.3). Furthermore, implementing modest hardware (§6.3.2) improvements can improve APOGEE's RV precision to 30 m s^{-1} which would permit 3σ detection of the entire BD mass regime to $\sim$ 3 AU over the temporal baseline of ATLaS alone. Adding the temporal baseline of APOGEE-1 and improving the pipeline to achieve 50 m s^{-1} in the legacy data would enable combing to comb the extent of the BD desert to the full 13 yr baseline for all BD masses, out to beyond 5 AU (see Fig. 6.1). With these improvements, the detection of $>$ 1000 BD companions would be possible with P1. Furthermore, with its improved RV precision, ATLaS P1 would be sensitive even into the planetary-mass regime to beyond the orbit of Jupiter around solar mass stars (see Figure 6.1).

Program 2 (P2): Planet Hunter Synergy Survey

Follow-up spectroscopy is important for the comprehensive characterization of transit-detected exoplanet systems for which only the period and the ratio of the planet's and star's radii is known, and for determining statistics of exoplanet populations (e.g., by determining the false positive rates). Unfortunately, many of *Kepler*'s transit detections were associated with relatively faint stars requiring a large investment of time for spectroscopic follow-up in a very limited range of LSTs with no dedicated follow-up network. The Transiting Exoplanet Survey Satellite (TESS; Ricker et al. 2014b), launching in 2018, will be a space-based all-sky transit survey, which will target 200,000 stars pre-selected for short-cadence observations recorded every two minutes and with full-frame images (FFIs) recorded every 30 minutes. Since the short-cadence targets will be drawn from the full sky, TESS can afford to focus on stars that are on average 100 times brighter than those observed by *Kepler*. This bright sample

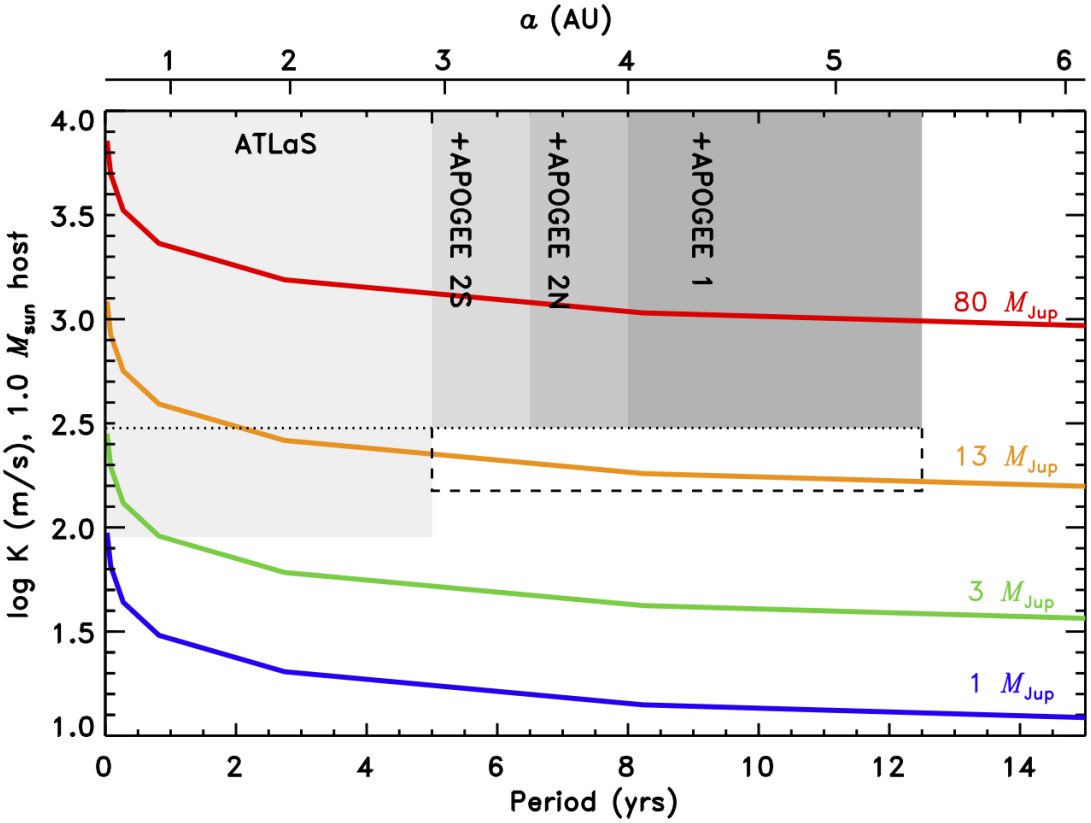

Fig. 6.1.— Colored lines represent velocity semi-amplitude (K) vs. orbital period (P) for companions of various masses. Grey regions illustrate detection sensitivity ($K > 3\sigma_{\rm RV}$) for the nominal proposal (which requires 30 m s^{-1} RV precision for ATLaS data and 100 m s^{-1} for APOGEE 1 & 2). The grey region below the dotted line is the scientific gain of improving the RV precision for ATLaS observations, which pushes our sensitivity into the planetary regime for all periods accessible by ATLaS observations alone. The dashed box shows the potential additional sensitivity to massive planets at large a if pipeline improvements can increase the APOGEE 1 & 2 RV precision as described in §6.3.3. *Figure courtesy of Joleen Carlberg.*

and selection across the full sky is intended to mitigate the spectroscopic follow-up backlog encountered with *Kepler* targets. A dedicated follow-up network is currently being built in which ATLaS **P2** can play a crucial rule.

The APOGEE spectrographs provide a timely and unique, all-sky spectroscopy resource for current (e.g., *Kepler/K2*, *Gaia*) planet (and binary)-hunting space missions, and AS4 is well-timed with the completion of TESSs primary mission in 2020.

ATLaS P2 would provide the only dual-hemisphere, spectroscopic follow-up of transit detections from the 200,000 short cadence targets as well as the additional 17,000 expected giant planet signals from the FFIs (Sullivan et al. 2015). Properties like their large FOV and obtainable magnitude limits make the APOGEE instruments well suited for this ground-based follow-up (e.g., Fleming et al. 2015). APOGEEs automated pipeline allows the efficient derivation of homogeneous stellar atmospheric parameters and detailed chemical abundances for all stellar targets, including M-dwarfs (Deshpande et al. 2013; Souto et al. 2016), making even a single AS4 visit an extremely valuable asset to stellar and exoplanet science that will complement the observations of these other major surveys. ATLaS P2 will derive stellar parameter ($T_{\rm eff}$, $\log g$, $v \sin i$), and a large set of individual elemental abundances (Fe, C, N, O, Si, Mg, etc.), *uniformly* and at high precision, not only for planet hosts but a huge control sample of TESS targets with no detected planets, a critical resource for understanding planet formation trends as a function of stellar chemistry, type, and Galactic locales spanning all environments in the Milky Way. As discussed in §1.1.2, several studies indicate that planet-hosting dwarf stars have different chemical abundance signatures compared to non-hosts, and P2 will be able to investigate these trends further using the largest sample of exoplanet host stars and non-hosts with homogeneously-derived abundances ever assembled.

In addition to exoplanet science, past partnerships between APOGEE and asteroseismologists, such as the APOGEE-Kepler Asterseicmic Science Consortium joint survey (APOKASC; Pinsonneault et al. 2014) and the COROT-APOGEE joint survey (CoRoGEE; Anders et al. 2017), demonstrate the mutual benefits of coordinating spectroscopy and asteroseismology, particularly for providing accurate *stellar ages*. ATLaS will continue to build on these foundations with K2 and TESS, which will

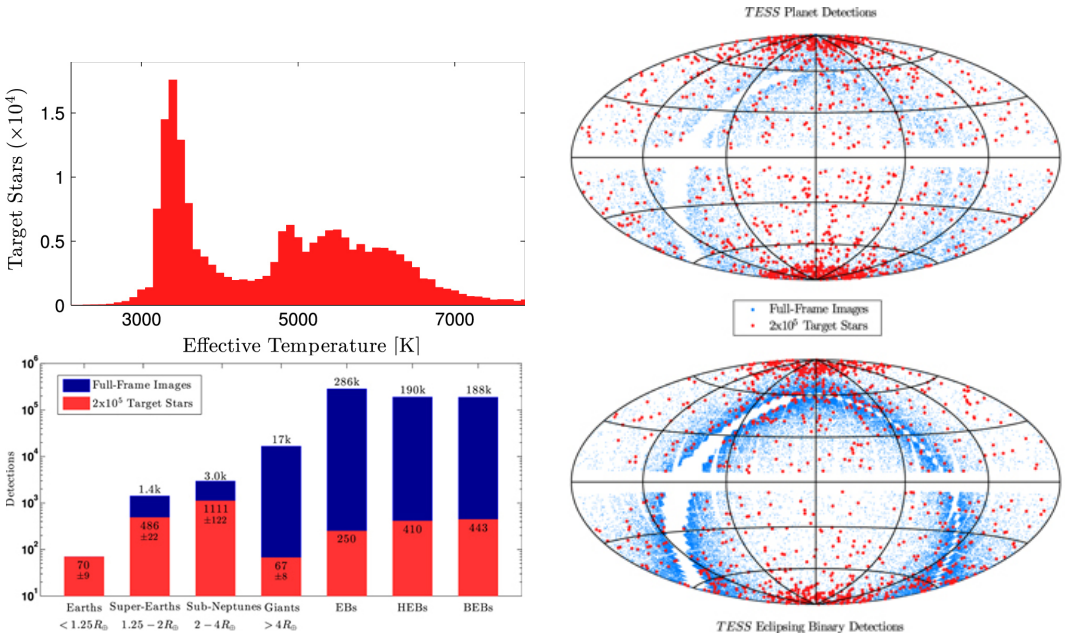

Fig. 6.2.— Figures 17, 18 and 19 from Sullivan et al. (2015) showing the Galactic and radius distribution of the expected yield of TESS, and the $T_{\rm eff}$ distribution of TESS target stars. Note the Galactic plots are in *ecliptic* coordinates, but the Galactic plane can clearly be seen as a zone of avoidance for TESS.

have a major asterosiesmology component (Campante et al. 2016).

The European Space Agency's Gaia mission will identify numerous astrometric binaries with orbital separations between, and complementary to, the unresolved ATLaS **P1** and resolved **P3** varieties, yet will not be able to break the degeneracies between primary and secondary masses without spectroscopic data that can be provided with a single ATLaS visit. An even more precise determination of the masses can be done if multi-epoch data from P1 can also be provided.

Program 3 (P3): A Near-IR Spatially Resolved Speckle Multiplicity Survey

The third component of the planned ATLaS program was to complement the P1 RV investigation of short-period multiplicity with diffraction-limited imaging, which

would allow us to investigate higher order multiplicity, as well as identify potentially confused RV signals from these perturbers. As discussed in Section 1.2.3, searching for long-period companions to stars known to have short-period companions will allow investigation of the importance of the Kozai mechanism in the formation of hot Jupiters and close binaries. In addition to the formation of hot Jupiters, the impact of giant planets undergoing Kozai-induced migration on the stability and habitability of terrestrial planets is an important consideration in the era of large-scale surveys for rocky planets (Menou & Tabachnik 2002; Kita et al. 2010). Furthermore, diffraction-limited imaging is a useful false-positive check for unresolved background sources in transit surveys. This is notoriously problematic in *Kepler* with its four arcsecond pixels, and this problem is only exasperated in *TESS* which will have pixels four times larger than *Kepler*'s.

To that end, we proposed ATLaS **P3** to be a large survey of near-IR diffraction-limited speckle imaging for bright stars to $H \sim 12$ to search for physical companions within the typical ground-based stellar light profile (down to $\sim 0.2''$) out to several arcseconds. This will produce the most extensive direct imaging study yet conducted of stellar multiplicity across the HR diagram, spanning a wide range of physical separations. Our primary mission will be to follow up many **P1** and **P2** targets, with priority to those stars having RV (i.e. **P1**) or transit/astrometric (i.e.**P2**) evidence for companions, and ease of imaging a companion (i.e. distance from the Sun and spectral type of the host star). Measuring the distribution of widely separated companions around stars known to host short-period companions (of which **P1** and **P2** will have numerous) is necessary for assessing the importance of the Kozai effect. We also anticipate many targets for **P3** independent of the other two ATLaS programs, including massive stars and massive star complexes, as well as young star forming

regions and clusters.

6.3.2 Hardware Upgrades for ATLaS

The ATLaS goals, detailed above, capitalize and expand on the dual-hemisphere, long temporal baseline, multi-epoch, high-resolution spectroscopy provided by the APOGEE instrument and the still unparalleled areal coverage provided by the Sloan and du Pont telescopes. Furthermore, the APOGEE instrument operates in the infrared (IR), which allows us to probe the dust-obscured parts of the Galaxy and achieve our goals of a *pan-Galactic* survey. With the modest modifications to the APOGEE instrument and current Sloan infrastructure outlined here, we can vastly improve the productivity, precision and yield of our survey.

Modifications to the Telescopes and Infrastructure

Robotic Fiber Positioner: The announced baseline plan for AS4 involves the building of rapidly-reconfiguring robotic fiber positioners for the SDSS and DuPont telescopes whose design will be based off of the Dark Energy Spectroscopic Instrument (DESI; Schubnell et al. 2016). Each fiber patrol area will be equipped with an interchangeable optical fiber and infrared fiber, allowing for rapid change between APOGEE and an optical spectrograph or for both to be used simultaneously. These positioners will allow for unprecedented efficiency and flexibility in Sloan observing.

However, if, like DESI, the AS4 positioners were designed with an evenly spaced grid of 300 fixed patrol areas, which would translate to 2.9 arcminutes radius per patrol area at APO, this would cause cause issues with dense fields such as clusters and the bulge which are *already* a challenge for fiber positioning on plugplates with a collision radius of a mere 70 arcsec. To mitigate this issue we requested that the robot

be engineered with maximally overlapping patrol areas, and that either the robot be placed in a removable cartridge so that the option to use traditional plugplates is still available, and/or that some period of AS4 (e.g., before robot commissioning) be allocated for plugplate observations of fields with high target densities.

Infrared-Optimized Corrector: Currently, APOGEE operates on the Sloan Telescope with the original spectroscopic corrector, which is not optimized for H-band work, and confers an overall 25% throughput loss to all APOGEE-N observations. There are several ways to redress this loss. One option is to simply build an H-band optimized spectroscopic corrector and swap correctors as needed to ensure the best throughputs for optical and APOGEE instrument passbands. However, if AS4 envisions co-observing optical and IR sources and only a single corrector can be used, we instead encouraged the replacement of the current spectroscopic corrector with one having more panchromatic transmission for both optical and IR work. Note that the common corrector also confers light losses in the H-band, with throughputs estimated at only 80-85%. However, it may be possible to recoat this optic to improve its throughput. Regardless, the expected increase in overall throughput for APOGEE instrument observations would be a windfall for ATLaS and all other IR applications by enabling either deeper magnitude limits, allowing us to extend our reach in the Galaxy, or shorter visits, allowing us to observe larger samples.

Modifications to the APOGEE Instruments

To achieve the goals of **P1**, we require improvement of the RV precision of the APOGEE instruments in any way easily achievable, with a target precision of 30 m s^{-1} (approaching the theoretical limit). Addressing the following issues would help to achieve this goal:

1. *LN2 tank "breathing" on the APOGEE-2N spectrograph:* The first APOGEE spectrograph was built with the liquid nitrogen (LN2) tank fixed to the bottom of the optical bench. Variations in the fill level of the LN2 tank impose differential flexure on the bench that has been shown to affect the RV measurements at the 10 m s^{-1} level (see Fig. 6.3). Fortunately, the APOGEE-2S instrument has been designed with this issue in mind, and the LN2 tank is decoupled from the optical bench. Unfortunately, decoupling the LN2 tank from the APOGEE-2N instrument would be a relatively expensive (>$100k) and risky proposition, so we are unlikely to pursue it.

2. *Dithering:* The blue end of the APOGEE spectral range is slightly undersampled, which is mitigated by a half-pixel spectral dither during observation. The reliability of these dithering moves is presently good to ∼1.3% of a pixel ($50-80$ m s^{-1}) RMS, but these offsets can only be estimated *ex post facto* from the data themselves. ATLaS has considered turning off the dithering mechanism as a means to stabilize the positions of the spectra on the arrays, but this will not be possible if there are other APOGEE programs, which no doubt would insist on dithering. Even our own **P2** would benefit from dithering, so we will likely not pursue this option.

3. *Environmental control:* Analysis of APOGEE-1 data shows that yearly changes in the mean atmospheric pressure in the APOGEE spectrograph lab induce perceptible effects on the temperature/pressure inside the cryostat (see Fig. 6.3), and therefore on the wavelength positioning on the arrays. To mitigate these effects, we proposed to installa back pressure regulator on the LN2 boil-off of the instrument itself to better control the internal pressure of the instrument, and to replace the clean curtain around the Northern instrument with an in-

sulated wall to control the ambient temperature surrounding the instrument to 0.5°C.

These and other systematics can be measured and calibrated out using a precision calibration source, such as an Fiber Fabry-Perot Interferometer (FFP). Tests with the Penn State Habitable Zone Planet Finder development group have demonstrated the ability of an FFP to trace internal APOGEE instrumental shifts to $\sim$ m s^{-1} levels on a single fiber exposed to calibration lamps (Fig. 1; Halverson et al. 2014). In AS4, we proposed for the installation of such devices (in both hemispheres) as a permanent fixture and an essential step in nightly operations. This could be achieved with relative ease by fiber-feeding an FFP comb at the top and bottom of the APOGEE detectors for *every* exposure, which would have the minimal impact of having one less sky and telluric fiber per pointing while gaining vastly superior calibration. Furthermore, the FFP lines can also be used as a benchmark to calibrate the use of sky and telluric lines as a stable wavelength calibrator for APOGEE-1/2 data, and to map the fiber LSFs as a function of wavelength. Moreover, additional RV precision will be achieved by scrambling fiber illumination errors through use of octagonal fibers (Halverson et al. 2015) for any new APOGEE fiber installations (e.g., in the AS4 robot positioner).

Multi-Object Speckle Instrument

To achieve our goals for **P3** we proposed to build two (one for each hemisphere) novel fiber-fed speckle interferometers, based on the design of the visible wavelength Differential Speckle Survey Instrument (DSSI, Horch et al. 2009), but capable of recording up to 300 target speckle sequences per visit by feeding the speckle images though densely-packed coherent fiber bundles. Like DSSI, the new system will collect speck-

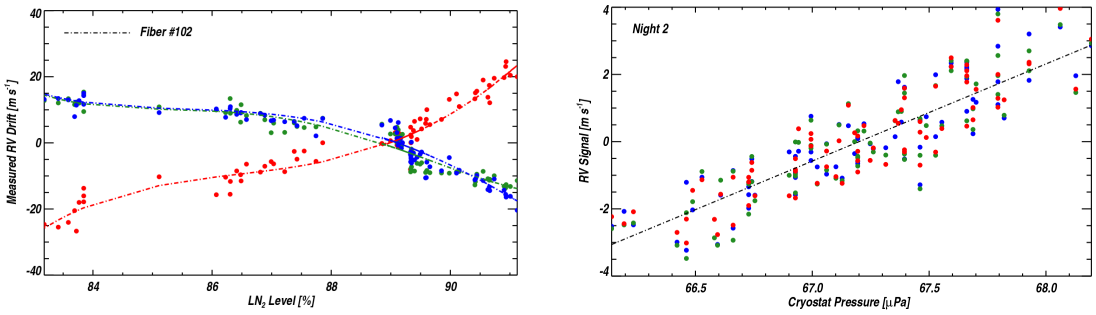

Fig. 6.3.— *Left:* Figure 11 from Halverson et al. (2014) showing the observed spectrograph drift as function of LN2 coolant level. *Right:* Figure 13 from Halverson et al. (2014) showing correlation between internal cryostat pressure and measured RV signal in FFP data during their observations for each APOGEE detector.

les in two bands simultaneously, but in our case, R and H band ($\lambda \approx 0.7$ and 1.5μm.) An H-band speckle camera realizes the advantages of (1) longer atmospheric coherence timescales, allowing longer exposure times ($4\times$ longer than V-band), and (2) more forgiving flux ratios between the typical APOGEE star (GKM spectral types) and potential companions, increasing the likelihood of detection. For example, previous results from DSSI on WIYN give a typical detection contrast of 4-5 magnitudes in a given band for a wide range of companion separations. In H band, this translates to being able to detect a companion of spectral type of M5V ($M \sim 0.2M_{\odot}$) around any main-sequence primary with spectral type later than F5V ($M < 1.4M_{\odot}$), compared to only K5V ($M < 0.85M_{\odot}$) in R band. The resolution obtained will be 0.05 and 0.11 arcseconds in the R and H bands, respectively, making the instrument sensitive to companions with projected separations as low as 50 AU at 1 kpc in the 0.7μm channel, and to potential Kozai Mechanism perturbers for much of our sample. A typical DSSI run on a WIYN-class telescope can obtain observations of several hundred targets of comparable brightness (Howell et al. 2011), thus this instrument, capable of observing several hundred targets in a single night, would be an order of

magnitude increase in efficiency.

To enable seamless operations between this instrument and the spectrographs, we proposed modifying the AS4 fiber positioner to include one coherent bundle feeding the speckle cameras along with the single optical and infrared fibers in each patrol area, making it possible to have the speckle system available at all times. This "triple instrument option" configuration would provide additional multiplexing power and efficiency to AS4, but also allow for on-the-fly "priority access" when seeing conditions become ideal for speckle observations. Furthermore, we proposed that this entire system (coherent bundles and the speckle detectors) serve double duty as the guide system for the AS4 positioner, one that is much simpler and better than a fixed guider by allowing guide stars of any desired number to be chosen anywhere in the field. In addition, guiding during APOGEE spectroscopy could be done directly at the same wavelength.

6.3.3 ATLaS Software Needs

Operations Software

Standard operations software at APO and LCO will serve most ATLaS needs, assuming that it will include standardized Sloan Telescope User Interface(STUI) control of the fiber positioner and autoscheduler-based scheduling. Software for STUI control of the speckle camera and FFP system would need to be written.

Spectroscopic Reduction and Analysis

Most of the spectroscopic reduction products already in place for APOGEE (`apogeereduce` and ASPCAP) can be used as-is for ATLaS, and we would gladly collaborate with other programs employing the APOGEE instrument in a unified reduction effort.

However, the current pipeline produces an RV precision of $\sim$100 m s^{-1}. Modifications to the wavelength calibration and RV derivation algorithms will be required to account for our proposed adjustments in observing strategies, in particular incorporating FFP exposures in our calibration routines to enable achievement of 30 m s^{-1} RV precision.

In addition, we intend to develop additional reduction algorithms for improving the RV precision of the legacy APOGEE-1&2 data by using both airglow and telluric absorption lines in the spectra as wavelength calibrators (in a less-precise and less-consistent, but similar manner, to an FFP). We expect this re-reduction of the APOGEE-1&2 data to achieve a RV precision of 50 m s^{-1} While this represents a fairly major software development effort, we will build from the efforts of Chad Bender and Cullen Blake, who has already made progress doing this with APOGEE spectra.

We will also strive to improve the RVs through better modeling of the spectrograph LSF, which is held constant in current software, but actually varies with wavelength and fiber and thus needs addressing. We expect this simple upgrade could improve APOGEE's RV precision by as much as $\sim$ 30 m s^{-1}.

Upgrades to Orbit-Fitting Pipeline

We will continue to use the `apOrbit` pipeline described in Chapter 2 with the upgrades described in Chapter 5. This would be run on all stars observed for **P1**, with further improvements to make it more robust, including better treatment of double-lined systems (SB2s) and multiple-component RV signals which constitute a significant number ($>$ 1000 in APOGEE-1 alone) of detections. Furthermore, reliable identification of SB2s before they are submitted to ASPCAP will allow us to shunt them to modified version of ASPCAP we are developing which can produce stellar

parameters for both components.

We are also actively studying ways to make automated bisector analysis presented in Section 5.1.3 convey more usable information such as the true mass of the companion and, thus, the inclination of the system. Other slated upgrades include improving stellar classification of the host (MS, SG, RG, etc.), and exploration of alternative orbit fitting codes. In particular, we will work on a multi-layered approach where we first discover orbits using a combination periodogram and reduced-χ^2 method, and then use MCMC based codes (e.g., EXOFAST; Eastman et al. 2013) to further refine the orbital elements.

Speckle Reduction and Analysis

Our plans for **P3** would require a new software pipeline for reduction and analysis of speckle data. Fortunately, Elliott Horch has a well-vetted pipeline for this from his DSSI speckle program, which, with his assistance, can easily be scaled for the proposed multi-object instrument.

6.3.4 ATLaS Survey Design

Here we describe the targeting plan and observing requirements for our programs in detail. ATLaS can achieve its goals with a modest amount of the available time at APO and LCO, leaving ample resources for other programs through shared plates and open time at a wide range of LSTs (Fig. 6.6). The low overhead advertised for the AS4 fiber positioner allows for much shorter dwell times than the standard SDSS observing mode with plugplates. Therefore, when designing this program we were instructed to assume base visit units of ten minutes, of which two minutes were designated to overhead for fiber reconfiguration and target acquisition. Our survey

will consist of three classes of observations, described below.

APOGEE Legacy Fields (P1)

We developed a preliminary list of ∼200 APOGEE legacy fields to follow up in AS4 (see Fig. 6.4) for ATLaS **P1**. These fields were selected using the following criteria on existing observations in priority order:

1. Visits in both APOGEE-1 and APOGEE-2,
2. a) 24 visits in APOGEE-2 (N or S), b) 12 visits in APOGEE-2, c) 24 visits in APOGEE-1,
3. 6-9 visits in either APOGEE-1 or APOGEE-2 *provided* the field probes a unique environment (e.g., a star cluster, bulge, Sgr dSph, MC, or YSO field).

We aim to observe 100k stars across all of these fields with 300-700 stars observed per field, depending on the density of the environment probed (e.g., halo vs. bulge).

Simulations and experience have shown that well-constrained Keplerian orbits require a minimum of 24 RV epochs per star (Kane et al. 2007a,b). Therefore, the number of visits required to a field in AS4 is given by subtracting 24 from the total previous visits to the field, but requiring a minimum of 6 AS4 visits to ensure high sensitivity to short and medium periods as well as long. These criteria yield the targeting plan shown in Figure 6.4. The individual AS4 visits should ideally satisfy the following schedule:

1. A ***Short Cadence*** with a 2-3 visits spread over a week,
2. A ***Medium Cadence*** that repeats the short cadence once per month for 2-3 months,

3. A ***Long Cadence*** which repeats the medium cadence once a year until all observations have been taken.

To achieve the longest baseline, fields which only require six visits in AS4 will use the above cadencing prescription using two rather than three (i.e. 2 visits spread over week once per month for 2 months).

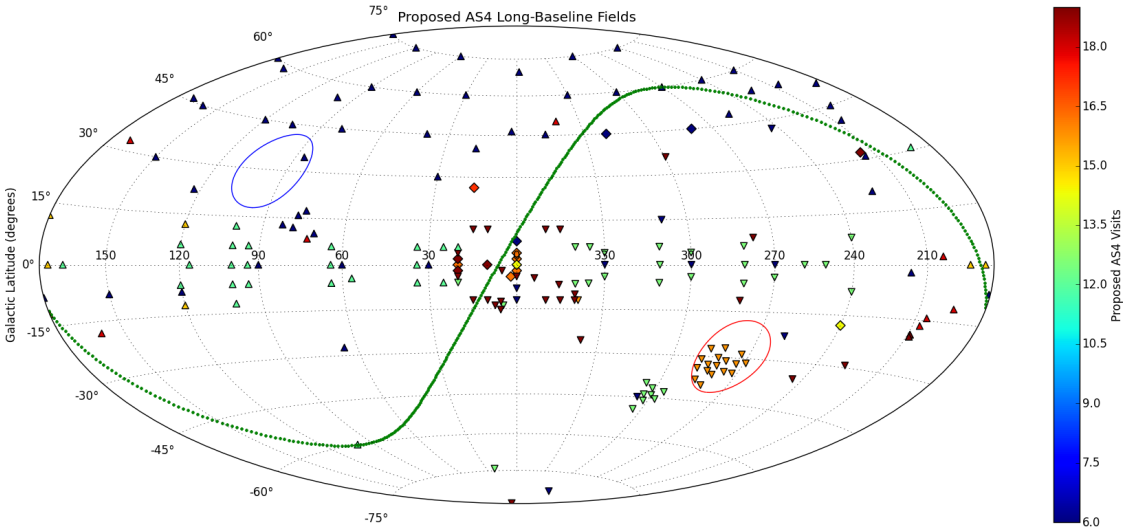

Fig. 6.4.— Proposed AS4-ATLaS long-baseline fields, with color of each point representing the number of AS4 visits. Upward pointing triangles are fields are APOGEE fields that only had visits from the North, and downward-pointing triangles are South only fields. Diamonds are APOGEE fields slated for observations in both the North and South. The North and South TESS CVZs are bordered with blue and red lines respectively, and the ecliptic plane (the path of K2's observations) is marked in green.

While APOGEE was primarily concerned with accumulated SNR for quality abundance analysis, ATLaS P1's greater focus on precision RVs shifts the paradigm to acquiring uniform SNR per visit. Unfortunately this runs counter to the AS4 plan for eight minute exposures (compared to APOGEE's 64), as many science cases driving ATLaS P1 depend on matching the legacy data collected in these fields, which include many stars too faint ($H > 11$) to accumulate sufficient signal in a single

eight minute exposure. However, the focus on SNR *per epoch* means only the faintest stars ($H > 12.8$) require a full APOGEE (64 minute) exposure. Therefore, we can employ a similar cohorting scheme where with the AS4 fiber positioner, targets in a field are sorted into cohorts by whether they require one (for $H \leq 11$ stars), two ($11 < H \leq 12.2$), four ($12.2 < H \leq 12.8$) or eight ($H > 12.8$) 8 min exposures during the visit. This particular magnitude breakdown ensures that all $H < 13.3$ stars in the field will attain $S/N \geq 30$, sufficient for the highest quality RV measurement. During an 8×10m minute visit to a field, each fiber is allowed to visit as many stars (from one faint to as many as eight bright) within its patrol area as can be accommodated with its eight total exposures. If the available targets are distributed evenly by magnitude and favorably by position on the sky up to 960 stars can be sampled in the in a single 8×10m visit to each field.

Except in the densest environments, P1 targets will likely not utilize every available fiber using this cohorting scheme. Therefore, empty fibers on a cohort will be filled with P2 and P3 targets of appropriate brightness. In particular, for the P3 speckle program, we will be reobserving a strategic subset of P1 stars that are close enough to resolve companions at $a < 1000$ AU with the goal of detecting long-period companions to objects with known short-period companions. As most of this subset will be the brighter stars in a field, and thus will be part of a shorter cohort, we can, instead of switching stars when the cohort is complete, stay on the same star and have the robot switch from an IR fiber to a coherent bundle for the next exposure. Furthermore, this cohorting scheme will allow ATLaS to seamlessly mesh its observing requirements with another AS4 bright-time program, DISCO, which requires targeting of a large number of bright stars in the Disk.

Finally, fiber-to-fiber variations in the LSF add to the RV error budget, at the

$\sim$10 m s^{-1} level. Removing such variations can be achieved by ensuring that each star is always observed through the same fiber. Such strict fiber management was implemented in the MARVELS survey, but for 1/5 the number of fibers that are used for APOGEE. While it is likely that manual plugging of SDSS plates would be challenged to deal with strict one-to-one plugging of even 300 fibers, a fiber positioner could ensure reliable, reproducible fiber assignment.

TESS CVZ Fields

TESS will observe the entire southern sky in its first year, and the north in its second. During each year, TESS will continuously observe in the 12 degrees surrounding the ecliptic poles (the "Continuous Viewing Zones (CVZs)"; shown in Fig. 6.4). Covering these regions will require 65 pointing at APO and 152 from LCO, a sizable request, but well worth it considering these regions will produce the vast majority of TESS detections (Sullivan et al. 2015). We plan to observe every TESS short cadence star as well as planet detection from the FFIs in the CVZs, for which we estimate target densities of about 10 and 1 FFI planet per square degree respectively. We will also target bright ($H < 12.2$) Gaia planet hosts and astrometric binaries in these fields (with a density of ~ 10 deg^{-2}). Therefore, in total, we proposed to observe ~ 120 and ~ 60 targets per APO and LCO pointing in the CVZs, leaving plenty of fibers open for other programs. In particular, the Southern CVZ fortuitously contains the Large Magellenic Cloud (LMC), so plates can be shared with programs to observe the LMC.

The faintest TESS short cadence stars have $H \sim 12.2$, which require 24 8-minute exposures to accumulate $S/N > 100$. Due to the range in brightness of these targets (see Figure 6.5), we wish to implement a cohorting and candencing scheme similar to

that described above for the APOGEE legacy fields to maximize the yield of each visit for both spectroscopy and speckle imaging. Therefore, we request twelve 20 minute (2×10 minute) visits for the CVZ fields with 10 & 20 min spectroscopic cohorts in each visit, with speckle observations being taken in parallel, as we discussed above in the APOGEE legacy fields.Furthermore, twelve epochs allows rudimentary Keplerian orbit fitting to these stars if RV variations are detected.

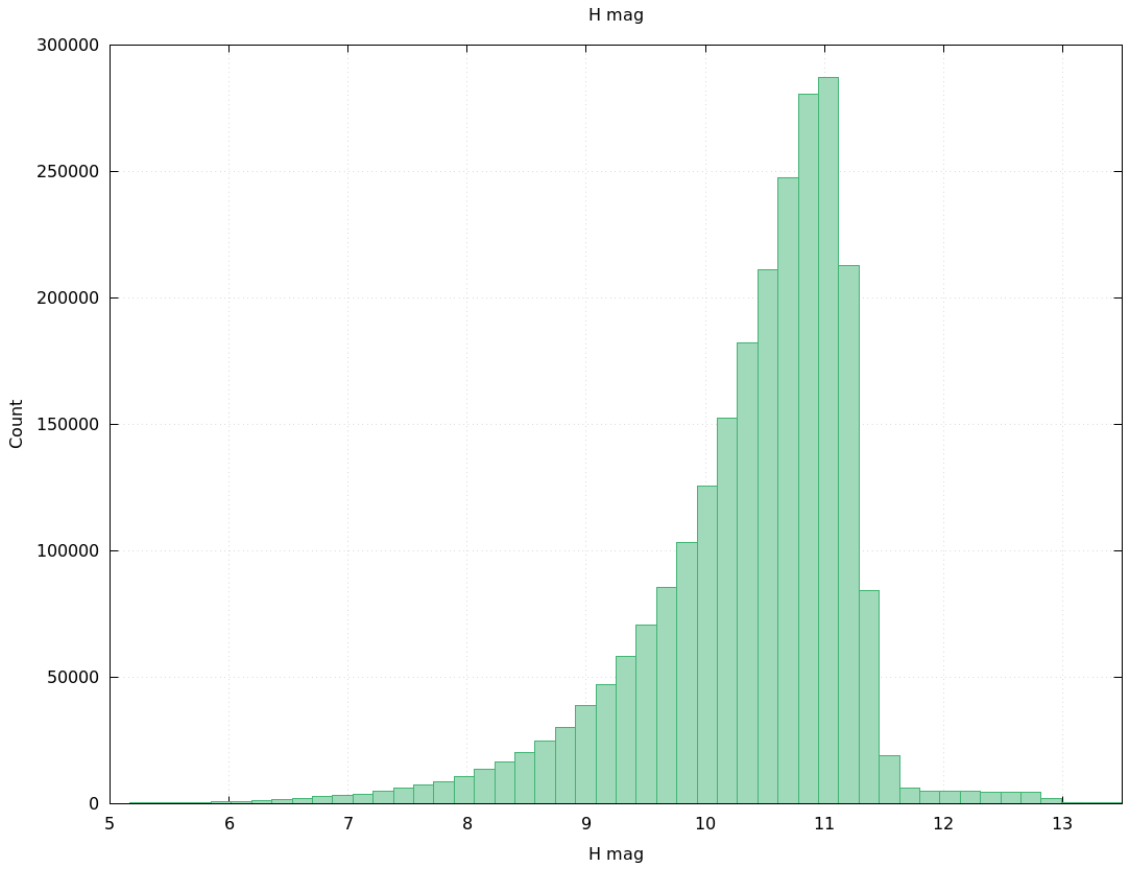

Fig. 6.5.— H magnitude distribution of the proposed TESS short cadence stars. *Image courtesy of the TESS targeting team.*

All-Sky Observations

As shown in Figure 6.6, there is time for four 8+2-minute visits across most of the sky[2], and as both TESS and Gaia are *all-sky* surveys, we wish to exploit this. For each pointing we will use three 8+2-minute visits for spectroscopic (P2) observations and one visit for speckle (P3) observations. All-sky AS4 coverage nominally creates the opportunity to observe *every* TESS target. Unfortunately, the planned 24 minutes total exposure per field limits us to $H \sim 10$ for the APOGEE minimum $S/N = 100$ for full chemical analysis. Nevertheless, for completeness, we will still observe every TESS short cadence star with the option to exchange the 8 minutes of speckle observations for a spectroscopic visit for the $H > 10$ targets. This would allow us to mitigate this issue that with 3 visits, the faintest ($H \sim 12.2$) will achieve only $S/N \sim 40$. However, the $> 80\%$ of TESS short cadence stars with $H < 11$ will achieve $S/N > 60$ in 3 visits, sufficient to derive stellar parameters and abundances for > 6 chemical elements for relatively metal rich stars (Majewski et al. 2015), which the vast majority of TESS targets will be. We will also observe TESS FFI and Gaia (transit and astrometric) detections with $H < 10$. Outside of the CVZ, we estimate ~ 5 deg^{-2} TESS short cadence stars, and ~ 10 deg^{-2} FFI, K2, and Gaia detections that meet our brightness limit. Therefore, we requested ~ 100 and ~ 50 targets per APO and LCO all-sky pointing, respectively, leaving a large number of fibers for other programs.

6.3.5 Anticipated Outcomes and Impacts of ATLaS

We anticipate that the ATLaS program laid out here will be the gold standard stellar multiplicity study for decades to come. Below we emphasize a few reasons why this will be the case:

[2]There is an oversubscription in RA range near the bulge and CVZs, but we can "drill over" to cover this range.

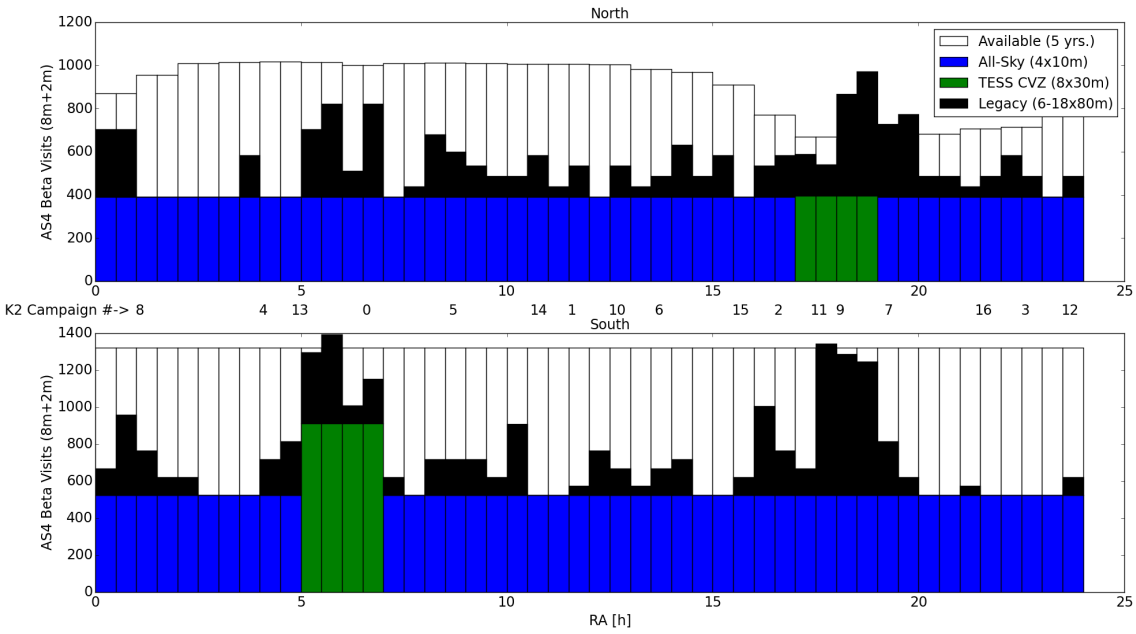

Fig. 6.6.— RA Distribution of ATLaS visits at APO (*top*) and LCO (*bottom*), color-coded by field class (see §3.3). The white histogram indicates the total amount of time avax ilable in a 5-year AS4 survey, accounting for the typical clear night fraction at each site. For reference, we have also indicated the RAs of each of the K2 campaign fields.

1. **An unmatched sample of stars with long-term RV monitoring:** By re-visiting fields with observations made in APOGEE-1 and -2, temporal baselines spanning up to 13 years will be accumulated for ∼100k stars. No other large RV survey, existing or planned (see Fig. 6.7), has sensitivity to companions with decade long periods *around such a diverse set of stellar types, drawn from such a massive parent sample*. In particular, we anticipate having detections from host stars at all stages of evolution from PMS to AGB stars.

2. **Unprecedented Reach:** The current gold standard multiplicity study (Raghavan et al. 2010) is a volume limited survey out to 25 pc, and the targets of most previous RV monitoring programs are within 1 kpc. Fig. 6.7 illustrates the anticipated Galactic reach of our **P1** targets, which does not even include our

intended exploration of companions in *other galaxies*, like the MCs and Galactic dSph satellites. Furthermore, using an IR instrument grants us access to highly dust-obscured regions of the Galaxy, such as the bulge and young clusters. Indeed, **P1** will be the first long-term RV monitoring program of the bulge.

3. **An abundance of companion host abundances:** With 1111 stars, Adibekyan et al. (2012) represents the current largest survey of planet hosts and non-hosts with multiple chemical abundances derived uniformly. In **P2**, we will uniformly acquire detailed abundances of >250k stars, including every TESS short cadence star across the sky. This represents *at least* an order of magnitude increase over any previous sample.

4. **Continued innovation of multiplexing technology: P3** will represent the first attempt to multiplex speckle observations. This will allow ATLaS to construct the largest collection of speckle observations (> 300k stars) ever assembled, and in the IR, where companion contrasts are minimized. Based on interest seen for DSSI already, this unique NIR-version could see widespread use in the community, sespecially among those studying multiplicity of late-type stars.

5. **Complete coverage of orbital phase space:** The combination of direct observations (RV and speckle) with characterization of transit, astrometric, or even microlensing companion hosts from surveys such as TESS and Gaia provides ATLaS with comprehensive coverage of companions from $a < 0.1$–1000 AU.

For the reasons stated above, ATLaS will be able to answer fundamental questions regarding the formation and evolution of stellar systems from a *stellar populations* mindset, including:

1. **The Fate of Companions:** How does the presence, nature and distribution of stellar companions vary as a function of stellar evolutionary phase (pre-main sequence, main sequence, subgiant, giant, and core He-burning stars — all stellar types already probed by the APOGEE instruments), and what is the fate of companions as their host star evolves through its evolutionary phases?

2. **The Importance of Host Star Composition:** How does the presence of companions vary as a function of the abundance of each of the chemical elements probed by APOGEE, and are there differences in these trends as a function of the abundance of, e.g., refractory versus volatile elements? Is there both an age and metallicity dependence for companion hosts?

3. **The Impact of Galactic Environment:** What is the Galactic distribution of companion hosts? How does the stellar multiplicity rate vary across the Milky Way and its satellite galaxies? How does the host environment (e.g., stellar density, radiation field, and dark matter density) affect the formation of companions? What can all of this tell us about the potential spatial distribution of life-hosting stellar systems in the Galaxy?

4. **Combing the Brown Dwarf Desert:** What do similarities and differences in the distributions of physical and orbital parameters for companions of stellar, BD and planetary mass tell us about the formation of BD companions?

5. **The Role of Higher-order Multiplicity:** What is the rate of higher-multiplicity systems as a function of stellar type, population, age, metallicity and environment? What role does the Kozai mechanism play in the formation of short-period companions?

6.3.6 ATLaS Moving Forward

The AS4 SC released their report of recommended programs in December of 2016. Unfortunately, P3 was not given much consideration due to the costs involved in building a new instrument on top of the already significant cost of building robotic fiber positioners for the duPont and Sloan 2.5m telescopes. However, many of the parts to build a prototype (single object) instrument including a suitable detector and coherent bundle fibers are currently available at UVa. Efforts are already underway, led by UVa instrument scientist J. Davidson. Furthermore, the fiber positioner will be designed so that the coherent fiber bundles required for speckle observations could be installed alongside the optical and IR fibers.

P1 and P2 of this proposal were highly regarded by the AS4 SC, and will be major bright-time programs in AS4. P2 was particularly well-matched with the SC's vision of an "All-Sky Synoptic Spectroscopic Survey," in which programs with "broad and shallow" observing plans are preferred. As TESS observations will begin in the southern hemisphere as early as late 2018, well before the start of AS4, there is a push by APOGEE partners at the Carnegie Observatories to observe the Southern CVZ using their proprietary nights with APOGEE at LCO.

P1 was slightly at odds with the "broad and shallow" strategy preferred by AS4, but we have found ways to make our program more amenable to this strategy. First of all, the planned increase of the base exposure time from eight to 15 minutes means that our maximum dwell time for a given P1 field is a maximum of four exposure units rather than eight. Furthermore, deeper analysis of our planned fields revealed that some fields do not have enough faint ($H > 12.8$) targets to justify a full 60-minute exposure. We assigned each field an exposure time based on the distribution of H magnitudes of stars in the field, with the underlying goal of achieving $S/N > 25$

per epoch. Fields with < 20 stars with $H > 12.8$ were assigned an exposure time of 30 minutes, and fields with < 20 $H > 12.2$ stars were assigned as 15 minute fields. There is a strong possibility that the fiber positioners may not ready for start of AS4, which would require the continued use of plugplates. Plugplates not conducive to switching every 15 minutes, so we would use the opportunity to observe as many of our 60-minute fields as possible. As discussed in §6.2, we also plan on using the APOGEE-2 bright time extension to relieve the stress on AS4.

Initial efforts by G. Zasowski and myself to simulate observing for a mock 5-year AS4 survey revealed that, with every approved program's fields considered separately, the survey is quite oversubscribed (by at least 2:1). Investigations of field-sharing paradigms between programs are currently underway to alleviate this problem. In addition to the above, ATLaS has made efforts towards this by agreeing to share plates with the multi-epoch QSO reverberation mapping program whose fields have target densities are low enough to enable plate sharing and require deep (60 minute) exposures per epoch. We also agreed to reduce the number of fields in regions where we requested large number of visits in a limited LST range, particularly the LMC, Orion, and the bulge, with the goal of requesting no more than 80 15-minute exposures per 3 degree bin of LST for dedicated ATLaS P1 pointings. The AS4 MW disk survey *Disco*, due to the shear density of targets in some locations, will also require multiple pointings to certain fields. We are currently exploring options to share fields by reserving a few dozen fibers in the multiple-exposure Disco fields, particularly in the oversubscribed bugle and inner disk. These initial consolidation efforts have already shown improvement, but there is still more work to be done to ensure that AS4 is a viable survey.

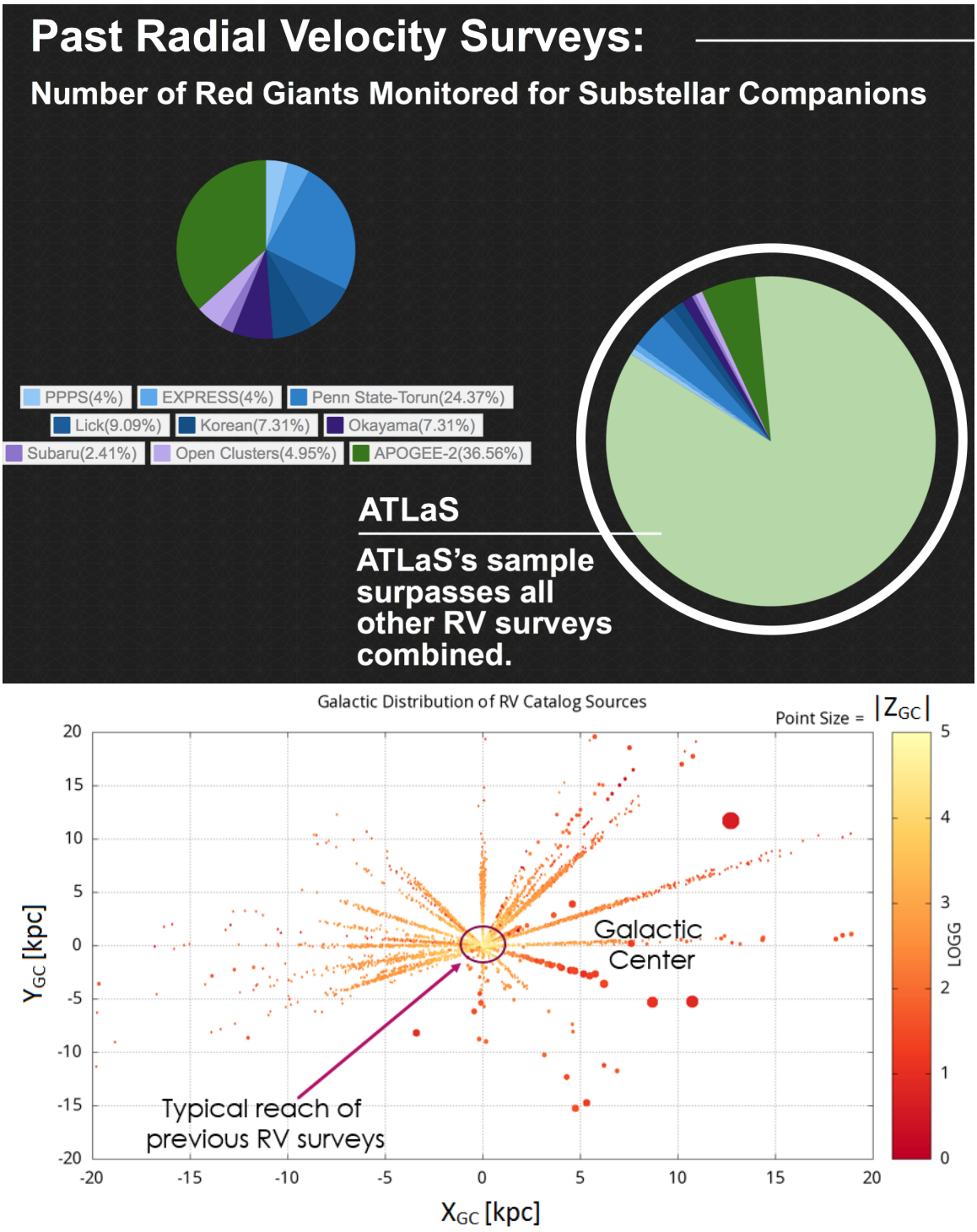

Fig. 6.7.— *Top:* Number of red giants targeted in previous long-term RV monitoring surveys compared to ATLaS **P1**.*Image courtesy of Joleen Carlberg. Bottom:* Expected Galactic distribution of ATLaS P1 targets in Galactic $X_{GC} - Y_{GC}$ coordinates with the Sun centered at $(X_{GC}, Y_{GC}) = (0, 0)$. The circle represents the typical ~ 1 kpc reach of most RV monitoring surveys.

Chapter 7

Summary and Outlook

7.1 Dissertation Summary and Takeaways

In this dissertation, I have given a glimpse of the power and challenges of considering stellar and substellar companion hosts as populations. Previous studies using such an approach led to landmark discoveries such as the Planet-Metallicity Correlation and the Brown Dwarf Desert. Upon the discovery of APOGEE's much-better-than-expected RV precision, coupled with the standard APOGEE strategy to visit stars over multiple epochs, it was realized that APOGEE was also capable of contributing to such discoveries.

To this end, we built a customized Keplerian orbit fitting pipeline to analyze APOGEE RV data, and developed criteria for selecting APOGEE "gold sample" companion candidates. Using initial tests with this pipeline, we were able to recover the orbital parameters of known exoplanets in the APOGEE database as well as identify a new false positive among the KOIs observed by APOGEE. Our first catalog derived from APOGEE DR12(Troup et al. 2016) already provided surprising results, challenging the previous-held notion of a Brown Dwarf Desert. In this catalog, at

least for larger separations ($a > 0.3$ AU), brown dwarf companions were found to be as common as stellar-mass companions. We attributed this to the diversity of stellar types encountered in our catalog compared to those used in previous work.

To further enable this work, we championed upgrades to the APOGEE pipelines that we believed would better our ability to detect companions in the APOGEE data. The first among these upgrades was the inclusion of rotational velocity information in APOGEE DR13, which allows calculation of more reliable stellar parameters for dwarfs. With this information, we also were able to check our orbital solutions for false positives due to rotational period aliasing. We also improved the APOGEE pipeline's handling of low S/N spectra, particularly in regard to RV measurement and spectral combination, enabling multiplicity studies of stars in local dSph galaxies, including orbital fitting of individual systems.

With the new data from APOGEE-2, as well as improved data from APOGEE-1 in hand, we built an updated catalog using APOGEE-2 DR14 and improved techniques for candidate selection. This new catalog largely confirmed our findings from the DR12 catalog of a lack of a prominent brown dwarf desert, and we used the new data available to us to further substantiate this finding. We found that the occurrence rate of brown dwarfs around dwarf star hosts in this catalog reached a minimum around solar mass and solar metallicity, which would explain previous studies' results of a brown dwarf desert around local solar-like stars. We also determined that the primary formation mechanism of brown dwarfs is likely shared between disk instability at lower metallicities and core accretion at higher metallicity, with disk instability overall being the more efficient way to create brown dwarf companions. Finally, we discussed our program of follow-up observations, and the continued pursuit of stellar and substellar companion science with the APOGEE spectrographs in APOGEE-2 and beyond.

7.2 Outlook

7.2.1 Upcoming Survey Missions

In the coming years, there are several space and ground-based survey missions that will be ripe for population studies of companion-hosting stars. Launching in 2018, NASA's Transiting Exoplanet Survey (TESS) is the direct successor to the *Kepler* and K2 missions, performing the first magnitude-limited *all-sky* transit survey. TESS's primary mission expects a yield of >20,000 exoplanets (Sullivan et al. 2015), and will allow for a complete accounting of occurrence rates of short-period exoplanets in the solar neighborhood. ESA's ongoing *Gaia* mission, another space-based all-sky survey, will discover an enormous number of binaries and planet candidates through precision astrometry, complementing the short period systems surveyed by TESS. The Large Synoptic Survey Telescope (LSST), because of its enormous field of view ($\sim$10 deg^2) and large (8.4 m primary) aperture, will be capable of surveying the entire southern sky every $\sim$ 3 nights, and will do so for 10 years. One of the primary design considerations of LSST is the detection of transient phenomenon, meaning that LSST will be an excellent source of microlensing detections.

7.2.2 The Latest Extreme-Precision RV Instruments

There are a number of state-of-the art single-object extreme-precision RV spectrographs coming online in the next decade built to support and enhance these survey missions, as well as make groundbreaking discoveries of their own. The Habitable-Zone Planet Finder (HPF; Mahadevan et al. 2012), slated to be installed on the HET within a year, is a near infrared (Y and J band), high-resolution ($R > 50,000$), extreme-precision RV instrument that drew heavily on the design of the APOGEE

spectrographs to achieve the exquisite stability required for ~ 3 m s^{-1} RV precision. A primary goal of HPF is to find planets in the Habitable Zone of M dwarfs.

Also in development is the "NN-explore Exoplanet Investigations with Doppler spectroscopy (NEID)" instrument to be deployed on the WIYN 3.5m telescope in the next few years. NEID builds upon the design legacy of APOGEE and HPF, and will push the limits of RV precision to < 1 m s^{-1}. This instrument, commissioned primarily for in-depth RV monitoring of well-vetted TESS objects of interest, is particularly exciting because it will be one of the first extreme-precision RV spectrographs available on a U.S. national facility, giving the full American astronomical community access to sub-m s^{-1} for the first time.

Furthermore, there are clever precision RV efforts exploiting small-aperture (< 1 m) telescopes in conjunction with affordable, reproducible, extreme-precision RV instruments. For example, the Miniature Exoplanet Radial Velocity Array (MINERVA; Swift et al. 2015) will employ an array of four commercially-available robotic 0.7 m telescopes to feed a single extreme precision RV instrument, thereby giving the effective collective area of a single 1.4 m telescope at significantly less expense.

7.2.3 The Future of Multi-Object Spectroscopy

A true successor to the work described in this dissertation would employ a massively multiplexed (> 100 fibers) extreme-precision ($\sim$ m/s) RV instrument on an 8-m class telescope with wide FOV (> 1 deg^2), such as LSST. Upon completion of its primary photometric mission in 2032, perhaps LSST will follow in the footsteps of its predecessor, SDSS, and evolve to include a spectroscopic survey. Such a facility would allow us to probe 2.5 magnitudes fainter than similar work with APOGEE. Ideally this instrument would be optimized for infrared observations to enable the

farthest Galactic reach, and to maximize the stellar types that can be surveyed.

Until such an instrument is commissioned, the APOGEE spectrographs will remain unrivaled for at least the next decade in survey efficiency and reach within the Galaxy due to their multiplexing capabilities over large FOVs, high resolution, infrared sensitivity, and unbiased targeting strategy. Moreover, the archived APOGEE databases starting from 2011 will increase in value for time series studies of RV variability. Novel and systematic large-scale probes of stars in the bulge, Galactic satellites, star clusters spanning all densities, metallicities and ages (including the most nascent and embedded), as well as field stars across all disk radii and out into the halo ensure that ATLaS, a companion search with the APOGEE instruments proposed for the "After-Sloan IV" survey, will be the most comprehensive and homogeneous, pan-Galactic exploration of binary stars, brown dwarfs, and (large) planetary mass companions for the foreseeable future. Indeed, our goal to acquire > 24 RV epochs for $\sim$100k stars will result in a sample of stars with decade-long spectroscopic monitoring that will be *at least* an order of magnitude larger than any other sample achieved by 2025. Furthermore, ATLaS, in conjunction with TESS, will also produce the largest sample of homogeneously-derived exoplanet host star abundances with comparably-sized control samples. In conclusion, the APOGEE instruments still have much to offer towards the field of companion host populations, and efforts are currently underway to make such contributions possible.

References

Abt, H. A. 2008, The Astronomical Journal, 135, 722

Adamów, M., Niedzielski, A., Villaver, E., Nowak, G., & Wolszczan, A. 2012, The Astrophysical Journal, 754, L15

Adams, F. C., Proszkow, E. M., Fatuzzo, M., & Myers, P. C. 2006, The Astrophysical Journal, 641, 504

Adibekyan, V. Z., Santos, N. C., Sousa, S. G., et al. 2012, Astronomy & Astrophysics, 543, A89

Adibekyan, V. Z., Figueira, P., Santos, N. C., et al. 2013, Astronomy & Astrophysics, 560, A51

Alam, S., Albareti, F. D., Prieto, C. A., et al. 2015, The Astrophysical Journal Supplement Series, 219, 12

Anders, F., Chiappini, C., Rodrigues, T. S., et al. 2017, Astronomy & Astrophysics, 597, A30

Armitage, P. 2000, Astronomy and Astrophysics

Barnes, S. A., Weingrill, J., Fritzewski, D., Strassmeier, K. G., & Platais, I. 2016, The Astrophysical Journal, 823, 16

Batürk, Ö., Dall, T. H., Collet, R., Lo Curto, G., & Selam, S. O. 2011, Astronomy & Astrophysics, 535, A17

Beaulieu, T., Bennett, D. P., Fouqué, P., et al. 2006, Nature, 439, 437

Becklin, E. E., & Zuckerman, B. 1988, Nature, 336, 656

Bodaghee, A., Santos, N. C., Israelian, G., & Mayor, M. 2003, Astronomy & Astrophysics, 404, 715

Bordé, P., Rouan, D., & Léger, A. 2003, Astronomy & Astrophysics, 405, 1137

Borucki, W. J., Koch, D., Basri, G., et al. 2010, Science, 327, 977

Boss, A. P. 1997, Science, 276, 1836

Bovy, J., Nidever, D. L., Rix, H.-W., et al. 2014, The Astrophysical Journal, 790, 127

Bressan, A., Marigo, P., Girardi, L., et al. 2012, Monthly Notices of the Royal Astronomical Society, 427, 127

Brucalassi, A., Pasquini, L., Saglia, R., et al. 2014, Astronomy & Astrophysics, 561, L9

—. 2016, Astronomy & Astrophysics, 592, L1

Campante, T. L., Schofield, M., Kuszlewicz, J. S., et al. 2016, The Astrophysical Journal, 830, 138

Carlberg, J. K., Cunha, K., Smith, V. V., & Majewski, S. R. 2012, The Astrophysical Journal, 757, 109

Carney, B. W., Latham, D. W., Stefanik, R. P., Laird, J. B., & Morse, J. A. 2003, The Astronomical Journal, 125, 293

Chojnowski, S., Nguyen, D., Nidever, D., et al. 2015, American Astronomical Society

Dall, T. H., Santos, N. C., Arentoft, T., Bedding, T. R., & Kjeldsen, H. 2006, Astronomy and Astrophysics, 454, 341

Damiani, C., & Díaz, R. 2016, 8

De Lee, N., Ge, J., Crepp, J. R., et al. 2013, The Astronomical Journal, 145, 155

Delgado Mena, E., Israelian, G., González Hernández, J. I., et al. 2010, The Astrophysical Journal, 725, 2349

Deshpande, R., Blake, C. H., Bender, C. F., et al. 2013, The Astronomical Journal, 146, 156

Díaz, R. F., Damiani, C., Deleuil, M., et al. 2013, Astronomy & Astrophysics, 551, L9

Dodson-Robinson, S. E., Laughlin, G., Bodenheimer, P. H., & Fischer, D. A. 2006, The Astrophysical Journal, 643, 484

Dotter, A., Chaboyer, B., Jevremovic, D., et al. 2008, \Apjs, 178, 37

Duchêne, G., & Kraus, A. 2013, Annual Review of Astronomy and Astrophysics, 51, 269

Duquennoy, A., & Mayor, M. 1991, Astronomy & Astrophysics, 248, 485

Eastman, J., Gaudi, B. S., & Agol, E. 2013, Publications of the Astronomical Society of the Pacific, 125, 83

Eggleton, P. P. 1983, The Astrophysical Journal, 268, 368

Eisenstein, D. J., Weinberg, D. H., Agol, E., et al. 2011, The Astronomical Journal, 142, 72

Fabrycky, D., & Tremaine, S. 2007, The Astrophysical Journal, 669, 1298

Fischer, D. A., & Valenti, J. 2005, The Astrophysical Journal, 622, 1102

Fleming, S. W., Ge, J., Barnes, R., et al. 2012, The Astronomical Journal, 144, 72

Fleming, S. W., Mahadevan, S., Deshpande, R., et al. 2015, The Astronomical Journal, 149, 143

Frink, S., Quirrenbach, A., Fischer, D., Röser, S., & Schilbach, E. 2001, Publications of the Astronomical Society of the Pacific, 113, 173

Gaia Collaboration, Brown, A. G. A., Vallenari, A., et al. 2016, Astronomy & Astrophysics, arXiv:1609.04172

García Pérez, A. E., Prieto, C. A., Holtzman, J. A., et al. 2015, eprint arXiv:1510.07635, arXiv:1510.07635

Ge, J., Mahadevan, S., Lee, B., et al. 2008, Extreme Solar Systems, 398

Geller, A. M., Mathieu, R. D., Harris, H. C., & McClure, R. D. 2008, The Astronomical Journal, 135, 2264

Girardi, L., Groenewegen, M. A. T., Hatziminaoglou, E., & da Costa, L. 2005, Astronomy & Astrophysics, 436, 895

Gizis, J. E., Kirkpatrick, J. D., Burgasser, A., et al. 2001, The Astrophysical Journal, 551, L163

González Hernández, J. I., & Bonifacio, P. 2009, Astronomy and Astrophysics, 497, 497

Grether, D., & Lineweaver, C. H. 2006, The Astrophysical Journal, 640, 1051

Guillot, T., Lin, D. N. C., Morel, P., Havel, M., & Parmentier, V. 2014, EAS Publications Series, 65, 327

Gunn, J. E., Siegmund, W. A., Mannery, E. J., et al. 2006, The Astronomical Journal, 131, 2332

Halverson, S., Roy, A., Mahadevan, S., et al. 2015, The Astrophysical Journal, 806, 61

Halverson, S. P., Mahadevan, S., Ramsey, L., et al. 2014, Publications of the Astronomical Society of the Pacific, 126, 445

Han, E., Wang, S. X., Wright, J. T., et al. 2014, Publications of the Astronomical Society of the Pacific, 126, 827

Hartman, J. D., Bakos, G. Á., Kovács, G., & Noyes, R. W. 2010, Monthly Notices of the Royal Astronomical Society, 408, 475

Hasegawa, Y., Pudritz, R. E., & Hirashita, H. 2014, The Astrophysical Journal, 788, 62

Hayden, M. R., Bovy, J., Holtzman, J. a., et al. 2015, The Astrophysical Journal, 808, 132

Hekker, S., Snellen, I. A. G., Aerts, C., et al. 2008a, Astronomy and Astrophysics, 480, 215

—. 2008b, Astronomy & Astrophysics, 480, 215

Hettinger, T., Badenes, C., Strader, J., Bickerton, S. J., & Beers, T. C. 2015, The Astrophysical Journal, 806, L2

Holtzman, J. A., Shetrone, M., Johnson, J. A., et al. 2015, The Astronomical Journal, 150, 148

Horch, E. P., Veillette, D. R., Baena Gallé, R., et al. 2009, The Astronomical Journal, 137, 5057

Howell, S. B., Everett, M. E., Sherry, W., Horch, E., & Ciardi, D. R. 2011, The Astronomical Journal, 142, 19

Janson, M., Jayawardhana, R., Girard, J. H., et al. 2012, The Astrophysical Journal, 758, L2

Jiang, P., Ge, J., Cargile, P., et al. 2013a, The Astronomical Journal, 146, 65

—. 2013b, The Astronomical Journal, 146, 65

Jofré, E., Petrucci, R., Saffe, C., et al. 2015, Astronomy & Astrophysics, 574, A50

Johnson, J. A., Fischer, D. A., Marcy, G. W., et al. 2007, The Astrophysical Journal, 665, 785

Johnson, J. A., Apps, K., Gazak, J. Z., et al. 2011, The Astrophysical Journal, 730, 79

Johnson, J. L., & Li, H. 2012, The Astrophysical Journal, 751, 81

Jones, M. I., Jenkins, J. S., Bluhm, P., Rojo, P., & Melo, C. H. F. 2014a, Astronomy & Astrophysics, 566, A113

Jones, M. I., Jenkins, J. S., Rojo, P., Melo, C. H. F., & Bluhm, P. 2014b, Astronomy & Astrophysics, 573, A3

Kane, S. R., Ford, E. B., & Ge, J. 2007a, Exoplanets: Detection, Formation and Dynamics, Proceedings of the International Astronomical Union, IAU Symposium, Volume 249, p. 115-118, 249, 115

Kane, S. R., Henry, G. W., Dragomir, D., et al. 2011, The Astrophysical Journal, 735, L41

Kane, S. R., Schneider, D. P., & Ge, J. 2007b, Monthly Notices of the Royal Astronomical Society, 377, 1610

Kita, R., Rasio, F. A., & Takeda, G. 2010, Astrobiology, Volume 10, Issue 7, pp. 733-741., 10, 733

Kozai, Y. 1962, The Astronomical Journal, 67, 591

Kuchner, M. J., & Seager, S. 2005, arXiv:astro-ph/0504214, arXiv:0504214

Kumar, S. S. 1962, The Astronomical Journal, 67, 579

LaCourse, D. M., Jek, K. J., Jacobs, T. L., et al. 2015, Monthly Notices of the Royal Astronomical Society, 452, 3561

Law, D. R., & Majewski, S. R. 2010, The Astrophysical Journal, 714, 229

Lee, B. L., Ge, J., Fleming, S. W., et al. 2011, The Astrophysical Journal, 728, 32

Liebert, J., Bergeron, P., & Holberg, J. B. 2005, The Astrophysical Journal Supplement Series, 156, 47

Lillo-Box, J., Barrado, D., Moya, A., et al. 2014, Astronomy & Astrophysics, 562, A109

Liu, G. Q., Deng, L., Chávez, M., et al. 2008, Monthly Notices of the Royal Astronomical Society, 390, 665

Lovis, C., & Mayor, M. 2007, Astronomy & Astrophysics, 472, 657

Lutz, T. E., & Kelker, D. H. 1973, Publications of the Astronomical Society of the Pacific, 85, 573

Mack, C. E., Ge, J., Deshpande, R., et al. 2013, The Astronomical Journal, 145, 139

Madore, B. F., & Freedman, W. L. 2005, The Astrophysical Journal, 630, 1054

Mahadevan, S., Ramsey, L., Bender, C., et al. 2012, in Ground-based and Airborne Instrumentation for Astronomy IV. Proceedings of the SPIE, Volume 8446, article id. 84461S, 14 pp. (2012)., ed. I. S. McLean, S. K. Ramsay, & H. Takami, Vol. 8446, 84461S

Majewski, S. R., Schiavon, R. P., Frinchaboy, P. M., et al. 2015, eprint arXiv:1509.05420, arXiv:1509.05420

Maldonado, J., & Villaver, E. 2017, Astronomy & Astrophysics, 602, A38

Marcy, G. W., & Butler, R. P. 2000, The Publications of the Astronomical Society of the Pacific, 112, 137

Markwardt, C. B. 2009, Astronomical Data Analysis Software and Systems XVIII ASP Conference Series, 411, 251

Massarotti, A., Latham, D. W., Stefanik, R. P., & Fogel, J. 2008, The Astronomical Journal, 135, 209

Masset, F. S., & Papaloizou, J. C. B. 2003, The Astrophysical Journal, 588, 494

Mata Sánchez, D., González Hernández, J. I., Israelian, G., et al. 2014, Astronomy & Astrophysics, 566, A83

Mathieu, R. D., Meibom, S., & Dolan, C. J. 2004, The Astrophysical Journal, 602, L121_L123

Matsuo, T., Shibai, H., Ootsubo, T., & Tamura, M. 2007, The Astrophysical Journal, 662, 1282

Mayor, M., & Queloz, D. 1995, Nature, 378, 355

Menou, K., & Tabachnik, S. 2002, The Astrophysical Journal, Volume 583, Issue 1, pp. 473-488., 583, 473

Meszaros, S., Holtzman, J., Garcia Perez, A. E., et al. 2013, The Astronomical Journal, 146, 133

Milliman, K. E., Mathieu, R. D., Geller, A. M., et al. 2014, The Astronomical Journal, 148, 38

Milone, A. P., Piotto, G., Bedin, L. R., et al. 2012, Astronomy & Astrophysics, 540, A16

Minor, Q. E. 2013, The Astrophysical Journal, 779, 116

Mordasini, C., Alibert, Y., & Benz, W. 2009, Astronomy and Astrophysics, Volume 501, Issue 3, 2009, pp.1139-1160, 501, 1139

Mullally, F., Coughlin, J. L., Thompson, S. E., et al. 2015, The Astrophysical Journal Supplement Series, 217, 31

Nakajima, T., Oppenheimer, B. R., Kulkarni, S. R., et al. 1995, Nature, 378, 463

Nelemans, G., & Tauris, T. M. 1998, Astronomy and Astrophysics

Nidever, D. L., Holtzman, J. A., Prieto, C. A., et al. 2015, The Astronomical Journal, 150, 173

Nordhaus, J., Spiegel, D. S., Ibgui, L., Goodman, J., & Burrows, A. 2010, Monthly Notices of the Royal Astronomical Society, 408, 631

Palmer, D. M. 2009, The Astrophysical Journal, 695, 496

Patel, S. G., Vogt, S. S., Marcy, G. W., et al. 2007, The Astrophysical Journal, 665, 744

Penev, K., Jackson, B., Spada, F., & Thom, N. 2012, The Astrophysical Journal, 751, 96

Pinsonneault, M. H., Elsworth, Y., Epstein, C., et al. 2014, The Astrophysical Journal Supplement Series, 215, 19

Pollack, J. B., Hubickyj, O., Bodenheimer, P., et al. 1996, Icarus, 124, 62

Privitera, G., Meynet, G., Eggenberger, P., et al. 2016, Astronomy & Astrophysics, Volume 591, id.A45, 14 pp., 591, arXiv:1604.06005

Raghavan, D., McAlister, H. A., Henry, T. J., et al. 2010, The Astrophysical Journal Supplement Series, 190, 1

Ramírez, I., Allende Prieto, C., & Prieto, C. A. 2010, The Astrophysical Journal, 743, 135

Rebolo, R., Osorio, M. R. Z., & Martín, E. L. 1995, Nature, 377, 129

Reffert, S., Quirrenbach, A., Landessternwarte, Z. A. H., et al. 2006, The Astrophysical Journal, 652, 1

Reipurth, B., Clarke, C. J., Boss, A. P., et al. 2014, Protostars and Planets VI (University of Arizona Press)

Ricker, G. R., Winn, J. N., Vanderspek, R., et al. 2014a, Journal of Astronomical Telescopes, Instruments, and Systems, 1, 014003

—. 2014b, Journal of Astronomical Telescopes, Instruments, and Systems, 1, 014003

Rodrigues, T. S., Girardi, L., Miglio, A., et al. 2014, Monthly Notices of the Royal Astronomical Society, 445, 21

Sahlmann, J., Ségransan, D., Queloz, D., et al. 2010, Astronomy & Astrophysics, 525, A95

Sahu, K. C., Casertano, S., Bond, H. E., et al. 2006, Nature, Volume 443, Issue 7111, pp. 534-540 (2006)., 443, 534

Santiago, B. X., Brauer, D. E., Anders, F., et al. 2015, eprint arXiv:1501.05500, 20

Scargle, J. D. 1982, The Astrophysical Journal, 263, 835

Schubnell, M., Ameel, J., Besuner, R. W., et al. 2016, in Proceedings of the SPIE, Volume 9908, id. 990892 6 pp. (2016)., ed. C. J. Evans, L. Simard, & H. Takami, Vol. 9908, 990892

Schultheis, M., Chen, B. Q., Jiang, B. W., et al. 2014, Astronomy & Astrophysics, 566, 120

SDSS Collaboration, Albareti, F. D., Prieto, C. A., et al. 2016, eprint arXiv:1608.02013, arXiv:1608.02013

Shetrone, M., Bizyaev, D., Lawler, J., et al. 2015, eprint arXiv:1502.04080, arXiv:1502.4080

Shvartzvald, Y., Maoz, D., Kaspi, S., et al. 2014, Monthly Notices of the Royal Astronomical Society, 439, 604

Siegel, M. H., Dotter, A., Majewski, S. R., et al. 2007, The Astrophysical Journal, 667, L57

Siegel, M. H., Majewski, S. R., Law, D. R., et al. 2011, The Astrophysical Journal, 743, 20

Silvotti, R., Charpinet, S., Green, E., et al. 2014, Astronomy & Astrophysics, 570, A130

Skemer, A. J., Hinz, P. M., Esposito, S., et al. 2012, The Astrophysical Journal, 753, 14

Skemer, A. J., Hinz, P., Esposito, S., et al. 2014, in SPIE Astronomical Telescopes + Instrumentation, ed. E. Marchetti, L. M. Close, & J.-P. Véran (International Society for Optics and Photonics), 91480L

Slawson, R. W., Prša, A., Welsh, W. F., et al. 2011, The Astronomical Journal, 142, 160

Souto, D., Cunha, K., Garca-Hernandez, A. D., et al. 2016, SDSS Paper, 87

Stassun, K. G., Mathieu, R. D., & Valenti, J. A. 2006, Nature, 440, 311

—. 2007, The Astrophysical Journal, 664, 1154

Sullivan, P. W., Winn, J. N., Berta-Thompson, Z. K., et al. 2015, The Astrophysical Journal, 809, 77

Swift, J. J., Bottom, M., Johnson, J. A., et al. 2015, Journal of Astronomical Telescopes, Instruments, and Systems, 1, 027002

Szentgyorgyi, A., Furesz, G., Cheimets, P., et al. 2011, Publications of the Astronomical Society of the Pacific, 123, 1188

Tabachnik, S., & Tremaine, S. 2002, Monthly Notices of the Royal Astronomical Society, 335, 151

Tanaka, K. E. I., & Omukai, K. 2014, Monthly Notices of the Royal Astronomical Society, 439, 1884

Torres, G., Andersen, J., & Giménez, A. 2010, The Astronomy and Astrophysics Review, 18, 67

Troup, N. W., Nidever, D. L., Lee, N. D., et al. 2016, The Astronomical Journal, 151, 85

Tsang, D., Turner, N. J., & Cumming, A. 2014, The Astrophysical Journal, 782, 113

Tsiganis, K., Gomes, R., Morbidelli, A., & Levison, H. F. 2005, Nature, 435, 459

Udalski, A. 2003, Acta Astronomica, 53, 291

Valenti, J. A., & Fischer, D. A. 2005, The Astrophysical Journal Supplement Series, 159, 141

Verbunt, F., & Phinney, E. 1995, Astronomy and Astrophysics

Villaver, E., & Livio, M. 2009, The Astrophysical Journal, 705, L81

Villaver, E., Livio, M., Mustill, A. J., & Siess, L. 2014, The Astrophysical Journal, 794, 3

Walsh, K. J., Morbidelli, A., Raymond, S. N., O'Brien, D. P., & Mandell, A. M. 2011, Nature, 475, 206

Wilson, J., Hearty, F. R., Skrutskie, M. F., Majewski, S. R., & Schiavon, R. P. 2015, in Prep.

Wilson, P. A., Hébrard, G., Santos, N. C., et al. 2016, Astronomy & Astrophysics, 588, A144

Wisniewski, J. P., Ge, J., Crepp, J. R., et al. 2012, The Astronomical Journal, 143, 107

Wittenmyer, R. A., Endl, M., Wang, L., et al. 2011, The Astrophysical Journal, 743, 184

Wolszczan, A., & Frail, D. A. 1992, Nature, 355, 145

Wright, J. T., Roy, A., Mahadevan, S., et al. 2013, The Astrophysical Journal, 770, 119

Wu, Y., & Murray, N. 2003, The Astrophysical Journal, 589, 605

Young, L. M. 2000, The Astronomical Journal, 119, 188

Zamora, O., García-Hernández, D. A., Prieto, C. A., et al. 2015, The Astronomical Journal, 149, 181

Zasowski, G., Johnson, J. A., Frinchaboy, P. M., et al. 2013, The Astronomical Journal, 146, 81

Zieliński, P., Niedzielski, A., Wolszczan, A., Adamów, M., & Nowak, G. 2012, Astronomy & Astrophysics, 547, A91